

HIGH-CONTRAST NEAR-INFRARED STUDIES OF PLANETARY SYSTEMS  
AND THEIR CIRCUMSTELLAR ENVIRONMENTS

by  
Timothy John Rodigas

---

A Dissertation Submitted to the Faculty of the  
DEPARTMENT OF ASTRONOMY  
In Partial Fulfillment of the Requirements  
For the Degree of  
DOCTOR OF PHILOSOPHY  
In the Graduate College  
THE UNIVERSITY OF ARIZONA

2013

THE UNIVERSITY OF ARIZONA  
GRADUATE COLLEGE

As members of the Dissertation Committee, we certify that we have read the dissertation prepared by Timothy John Rodigas entitled "High-Contrast Near-Infrared Studies of Planetary Systems and their Circumstellar Environments" and recommend that it be accepted as fulfilling the dissertation requirement for the Degree of Doctor of Philosophy.

\_\_\_\_\_  
Phil Hinz Date: 20 August 2013

\_\_\_\_\_  
Laird Close Date: 20 August 2013

\_\_\_\_\_  
Renu Malhotra Date: 20 August 2013

\_\_\_\_\_  
George Rieke Date: 20 August 2013

\_\_\_\_\_  
Daniel Apai Date: 20 August 2013

Final approval and acceptance of this dissertation is contingent upon the candidate's submission of the final copies of the dissertation to the Graduate College.

I hereby certify that I have read this dissertation prepared under my direction and recommend that it be accepted as fulfilling the dissertation requirement.

\_\_\_\_\_  
Dissertation Director: Phil Hinz Date: 20 August 2013

## STATEMENT BY AUTHOR

This dissertation has been submitted in partial fulfillment of requirements for an advanced degree at The University of Arizona and is deposited in the University Library to be made available to borrowers under rules of the Library.

Brief quotations from this dissertation are allowable without special permission, provided that accurate acknowledgment of source is made. Requests for permission for extended quotation from or reproduction of this manuscript in whole or in part may be granted by the head of the major department or the Dean of the Graduate College when in his or her judgment the proposed use of the material is in the interests of scholarship. In all other instances, however, permission must be obtained from the author.

SIGNED: Timothy John Rodigas

## ACKNOWLEDGMENTS

I would like to thank several people who helped me get to this point: my advisor, Phil Hinz, for guiding me through these past five years, for giving me the opportunity to use/play/break his ultra-expensive instruments/cameras/detectors, and for showing me the ropes of how to be a real astronomer; Laird Close, for always having a great attitude and giving me great career advice; and Renu Malhotra, for teaching me orbital dynamics and then helping me test that knowledge with my own ideas.

I'd also like to thank collaborators and co-authors that have helped me over the years: Jared Males, the 14 Her paper would not have been possible without your work; Andy Skemer, former officemate and fellow Knicks/Yankees fan, for many helpful discussions; and John Debes and Glenn Schneider, for countless helpful discussions about debris disks.

Finally, I'd like to thank NASA for funding my research for the past 3 years as part of the NASA Earth and Space Science Fellowship (NESSF). I was honored to be able to tell my friends that I was "working" for NASA.

## DEDICATION

This thesis is dedicated to several people: my mother, for her relentless belief that I just needed the “light bulb” to go on in my head in order to succeed in math and science (how right she was!); and for fostering my love of astronomy as a child (the books, movies, telescopes, and the trips to the planetarium in New York come to mind); my brothers and sisters, whose continuous amazement and wonder at my achievements was fuel for my academic fire; Take Kominogo, my intro to Calculus teaching assistant at UVA, whose passion and love for Math spilled over to me and helped me realize I too loved Math; John Hawley, whose cosmology class at UVA (for non-science majors) inspired me to abandon my planned major in the Classics and instead choose Astrophysics; Dave Prockop, my Astronomy teacher at Groton School, for treating me like a peer and colleague, allowing my passion to drive me to succeed; and my fiancée Colleen, who has been by my side every step of the way (even while living across the country from me for the first two years of grad school).

Finally, this thesis is dedicated to my deceased father Paul Rodigas. Dad, I’m not a heart surgeon like you were, but hopefully Astrophysicist isn’t too shabby.

## TABLE OF CONTENTS

LIST OF FIGURES . . . . .	9
LIST OF TABLES . . . . .	12
ABSTRACT . . . . .	13
1 INTRODUCTION . . . . .	15
1.1 Orbits and Masses of Planets Detected by Radial Velocity . . . . .	17
1.2 NIR Imaging of Debris Disks . . . . .	20
1.2.1 The Need for Adaptive Optics . . . . .	22
1.2.2 Results on HD 15115 and HD 32297 . . . . .	24
1.3 Dynamics of Dust Grains Shepherded by Planets . . . . .	25
2 WHICH RADIAL VELOCITY EXOPLANETS HAVE UNDETECTED OUTER COM- PANIONS? . . . . .	27
2.1 Introduction . . . . .	28
2.2 Simulation Parameters and Methodology . . . . .	31
2.3 Results and Discussion . . . . .	36
2.3.1 Control Simulations . . . . .	36
2.3.2 Matching the Observed Eccentricity Distribution . . . . .	39
2.3.3 Eccentricity as an Indicator of Multiplicity . . . . .	41
2.3.4 Why Not Observe Zero-Eccentricity RV Planets? . . . . .	44
2.3.5 The Uniqueness Problem . . . . .	44
2.4 Conclusions . . . . .	45
3 DIRECT IMAGING CONSTRAINTS ON THE PUTATIVE EXOPLANET 14 HER C . . . . .	53
3.1 Introduction . . . . .	54
3.2 Observations and Data Reduction . . . . .	57
3.3 Results and Discussion . . . . .	58
3.3.1 Phase Space Constraints . . . . .	59
3.4 Conclusions: What is 14 Her c? . . . . .	62
4 THE GRAY NEEDLE: LARGE GRAINS IN THE HD 15115 DEBRIS DISK FROM LBT/PISCES/ $K_s$ AND LBTI/LMIRCAM/ $L'$ ADAPTIVE OPTICS IMAGING . . . . .	68
4.1 Introduction . . . . .	69
4.2 Observations and Data Reduction . . . . .	72
4.2.1 LBT/PISCES $K_s$ band . . . . .	72
4.2.2 LBTI/LMIRcam $L'$ . . . . .	75
4.2.3 Ancillary Keck/NIRC2 $K_s$ band data . . . . .	78

4.3	Results . . . . .	79
4.3.1	Disk FWHM . . . . .	79
4.3.2	Disk Position Angle . . . . .	80
4.3.3	Surface Brightness Profiles . . . . .	82
4.3.4	Limits on Planets . . . . .	84
4.4	Interpretations . . . . .	85
4.4.1	Disk Structure . . . . .	85
4.4.2	Disk Color and Grain Sizes . . . . .	87
4.4.3	Does the disk have a gap? . . . . .	88
4.4.4	Limits on a planet inside the gap . . . . .	89
4.5	Summary . . . . .	90
5	LBTI/LMIRCAM HIGH-CONTRAST 3.8 $\mu\text{m}$ IMAGING OF THE HD 32297 DEBRIS DISK . . . . .	103
5.1	Introduction . . . . .	103
5.2	Observations and Data Reduction . . . . .	105
5.2.1	Observations . . . . .	105
5.2.2	Data reduction . . . . .	106
5.3	Results . . . . .	108
5.3.1	Surface Brightness Profiles . . . . .	108
5.3.2	Position Angle Measurements . . . . .	111
5.3.3	Limits on Planets . . . . .	112
5.4	Modeling the debris disk's dust . . . . .	115
5.4.1	Scattered Light Models of Optically Thin Disks . . . . .	116
5.4.2	Comparison to the D13 model . . . . .	118
5.4.3	Comparison to Water Ice, Tholins, and Silicates . . . . .	118
5.5	Summary . . . . .	120
6	EMPIRICAL CONSTRAINTS ON PLANETS SHEPHERDING DEBRIS DISKS FROM SCATTERED LIGHT OBSERVABLES . . . . .	133
6.1	Introduction . . . . .	134
6.2	Methods . . . . .	135
6.2.1	Initial conditions . . . . .	139
6.2.2	Control simulation . . . . .	144
6.3	Results . . . . .	145
6.3.1	Caveats . . . . .	146
6.4	Predictions for resolved debris rings . . . . .	148
6.4.1	Fomalhaut . . . . .	148
6.4.2	HR 4796A . . . . .	148
6.4.3	HD 207129 . . . . .	149
6.4.4	HD 202628 . . . . .	150
6.4.5	HD 181327 . . . . .	150

6.5	Parent body disk widths . . . . .	151
6.6	Summary: Observer's Procedure . . . . .	152
7	CONCLUSIONS . . . . .	159
7.1	Summary . . . . .	159
7.2	Future Work: Searching for Water Ice and Organics in Resolved Debris Disks with MagAO/Clio . . . . .	162
A	ACCOUNTING FOR DISK SELF-SUBTRACTION BY LOCI IN THE HD 15115 DATA . . . . .	167



## LIST OF FIGURES

2.1	The observed RV eccentricity distribution from <a href="http://exoplanet.eu">http://exoplanet.eu</a> as of January 2009 . . . . .	29
2.2	Typical radial velocity plot from the simulations . . . . .	35
2.3	Output semi-major axis as a function of the input semi-major axis for the control simulation (one-planet systems), and the same for mass . . . . .	37
2.4	Eccentricity distributions for the control simulation (one-planet systems) and for simulated two-planet systems . . . . .	47
2.5	Output semi-major axis as a function of the input semi-major axis in simulated systems with two planets, and the same for mass . . . .	48
2.6	Simulated eccentricity distributions and the observed single-planet eccentricity distribution from <a href="http://exoplanet.eu">http://exoplanet.eu</a> . . . . .	49
2.7	Cumulative distribution functions of the simulated eccentricity distributions . . . . .	50
2.8	Ratio of the semi-major axes of the two planets in each simulated two-planet system as a function of fitted eccentricity, and the same for mass . . . . .	51
2.9	Probability of a given single eccentric planet having a wide-separation companion . . . . .	52
3.1	RV data excluding the primary (b) component for 14 Her, from Wittenmyer et al. (2007) . . . . .	63
3.2	Final reduced image of 14 Her . . . . .	64
3.3	Mass vs. semimajor axis for 14 Her c . . . . .	65
3.4	14 Her c's mass vs. projected separation at the epoch of our imaging observations . . . . .	66
3.5	Mass vs. semimajor axis for 14 Her c, with the $42 M_J$ upper limit included . . . . .	67
4.1	Final PISCES $Ks$ band image and SNRE map of the HD 15115 debris disk . . . . .	93
4.2	Final LMIRcam $L'$ image and SNRE map of the HD 15115 debris disk . . . .	94
4.3	Disk FWHM as a function of distance from the star . . . . .	95
4.4	Disk PA as a function of distance from the star . . . . .	96
4.5	SB profiles of the disk at $Ks$ band and $L'$ . . . . .	97
4.6	Aggressive LOCI reduction of the $L'$ data, and corresponding $5\sigma$ sensitivity curve. . . . .	98
4.7	Model image and its PA as a function of distance from the star . . . .	99
4.8	Disk color as a function of distance from the star . . . . .	100

4.9	Equilibrium disk temperature vs. distance from the star, for several different silicate grain sizes . . . . .	101
4.10	Masses of a possible object orbiting inside a disk with a gap as a function of semimajor axis . . . . .	102
5.1	$L'$ final image of the HD 32297 debris disk, along with its corresponding SNRE map . . . . .	121
5.2	$L'$ image of the HD 32297 debris disk, along with three model disk inserted and recovered after running the PCA pipeline . . . . .	122
5.3	SB profiles of the HD 32297 debris disk at 1-2 $\mu\text{m}$ and 3.8 $\mu\text{m}$ . . . . .	123
5.4	PA as a function of distance from the star at 1-2 $\mu\text{m}$ and 3.8 $\mu\text{m}$ . . . . .	124
5.5	Artificial planets inserted into the HD 32297 debris disk at varying brightnesses . . . . .	125
5.6	Mass limits for planets embedded in the HD 32297 debris disk . . . . .	126
5.7	Visible spectrum of HD 32297, used for classifying its spectral type . . . . .	127
5.8	HD 32297's position on an HR diagram . . . . .	128
5.9	Comparison between the D13 model spectra and the spectrum of the HD 32297 disk . . . . .	129
5.10	PA vs. distance from the star for the real disk data and the D13 model . . . . .	130
5.11	Comparison between model spectra for 1 $\mu\text{m}$ tholins and the spectrum of the HD 32297 disk . . . . .	131
5.12	PA vs. distance from the star for the real disk data and the tholins model disk . . . . .	132
6.1	$\beta$ profiles for $\mu = 0.3\mu_J$ and initial $e_{disk,i} = 0.10$ , and $\beta$ -summed optical depth profiles for different $\mu$ values, all with $e_{disk,i} = 0.10$ . . . . .	154
6.2	Final disk eccentricity as a function of initial disk eccentricity for the various input planet masses . . . . .	155
6.3	Normalized disk FWHM as a function of final disk eccentricity for the various input planet masses . . . . .	156
6.4	Normalized disk FWHM as a function of planet mass ratio . . . . .	157
6.5	Normalized parent body disk FWHM as a function of planet mass ratio . . . . .	158
7.1	<i>Left:</i> from Honda et al. (2009), 2-4 $\mu\text{m}$ photometry of the circumstellar disk of the Herbig Ae star HD 142527. <i>Right:</i> NIR spectrum of the HR 4796A debris disk (squares, from HST), along with model spectra of various dust species (from John Debes, private communication). . . . .	165

7.2	Spectrum of Saturn's moon Phoebe from Buratti et al. (2008), with Ks and L' images of the HD 15115 debris disk on either side (Rodrigas et al., 2012). With an additional resolved image of the disk in the H <sub>2</sub> O band, we could constrain the amount of water ice/organics in the dust. This is the general idea for each target debris disk. . . .	166
A.1	Expected and observed artificial disks at <i>Ks</i> band and <i>L'</i> . . . . .	168
A.2	Expected and observed PA, FWHM, and SB as a function of distance from the star at <i>Ks</i> band and <i>L'</i> . . . . .	169

## LIST OF TABLES

2.1	Summary of simulation parameters and results . . . . .	41
2.2	RV follow-up/direct imaging observing strategy . . . . .	43
4.1	$Ks$ band SB power-law indices . . . . .	83
6.1	Numerically determined $a_p/a_{inner}$ . . . . .	141
6.2	Dynamics Simulation Parameters . . . . .	144
6.3	Dynamically Predicted Masses and Orbits for Known Debris Disks	150
7.1	Debris Disk Target List . . . . .	164

## ABSTRACT

Planets are thought to form in circumstellar disks, leaving behind planetesimals that collide to produce dusty debris disks. Characterizing the architectures of planetary systems, along with the structures and compositions of debris disks, can therefore help answer questions about how planets form. In this thesis, I present the results of five papers (three published, two in preparation) concerning the properties of extrasolar planetary systems and their circumstellar environments.

Chapters 2 and 3 are studies of radial velocity (RV) exoplanetary systems. For years astronomers have been puzzled about the large number of RV-detected planets that have eccentric orbits ( $e > 0.1$ ). In Chapter 2 I show that this problem can partially be explained by showing that two circular-orbit planets can masquerade as a single planet on an eccentric orbit. I use this finding to predict that planets with mildly eccentric orbits are the most likely to have massive companions on wide orbits, potentially detectable by future direct imaging observations. Chapter 3 presents such a direct imaging study of the 14 Her planetary system. I significantly constrain the phase space of the putative candidate 14 Her c and demonstrate the power of direct imaging/RV overlap.

Chapters 4 and 5 are high-contrast 2-4  $\mu\text{m}$  imaging studies of the edge-on debris disks around HD 15115 and HD 32297. HD 15115's color is found to be gray, implying large grains 1-10  $\mu\text{m}$  in size reside in stable orbits in the disk. HD 32297's disk color is red from 1-4  $\mu\text{m}$ . Cometary material (carbon, silicates, and porous water ice) are a good match at 1-2  $\mu\text{m}$  but not at  $L'$ . Tholins, organic material that is found in outer solar system bodies, or small silicates can explain the disk's red color but not the short wavelength data.

Chapter 6 presents a dynamical study of dust grains in the presence of massive planets. I show that the width of a debris disk increases proportionally with the mass of its shepherding planet. I then make predictions for the masses and orbits of putative planets in five well-known disks. In Chapter 7, I summarize and discuss plans for future research in the exoplanet field.

## CHAPTER 1

## INTRODUCTION

When I started graduate school at the University of Arizona in the fall of 2008, the number of confirmed exoplanets was only  $\sim 300$ . Most were detected by the radial velocity (RV) technique, with a few transit detections, a few microlensing detections, and one ambiguous direct imaging detection (Chauvin et al., 2004). Since then, the number of (candidate) exoplanets has increased tenfold, with thousands of candidates detected by Kepler, hundreds more by continued RV monitoring, dozens detected by microlensing, and a handful directly imaged. Consequently our understanding of planetary system architectures, planet formation, and planetary atmospheres and compositions has dramatically increased.

Despite these recent advances, we still have much to learn. How do planets form? What are their orbits like? How common is our solar system? Do Earth-like worlds exist, and if so, what are their atmospheres like? Answering these questions completely will require many more years of observations. The exoplanet field is a young one, and so the answers to these questions are slowly being discovered.

The atmospheres of the planets we can study so far are very alien—most are “hot Jupiters” orbiting so close to their host stars that their effective temperatures are  $\sim$  an order of magnitude higher than Jupiter’s; others, probed spectrophotometrically via direct imaging, tell us about the compositions of hot, young, very massive, long-period planets. None of these resemble an Earth-like planet in a habitable zone orbit, let alone a Jupiter on a Jupiter-like orbit. Additionally, we still have only a few direct measurements of the true masses of exoplanets. Aside from those detected simultaneously by transits and RV, and in special cir-

cumstances by transit timing variations (TTV), every mass reported to date is either a lower or upper limit or inferred from models. Without the true masses of exoplanets, planet formation models will be inaccurate, and our solar system's uniqueness (or lack thereof) will remain unknown.

Circumstellar environments—in particular, debris disks, the remnants of planet formation that are thought to resemble our Kuiper Belt—can indirectly tell us about planets that otherwise might remain undetected. Planets can create morphological signatures in the disk like warps and gaps (Kuchner & Holman, 2003), which are much easier to detect than the planets themselves. In special cases (like the  $\beta$  Pic system and possibly Fomalhaut), the detection of the disk *and* the perturbing planet can constrain planetary formation models and inform on the structures of planetary system architectures. Additionally, the composition of the dust grains can inform on whether a hidden planetary system might have the raw ingredients necessary for life. While it is now thought that at most only a small fraction of Earth's oceans was acquired via collisions with gravitationally scattered icy comets in the early solar system (Drake (2005), and references therein), finding water in extrasolar Kuiper Belt analogs would suggest that the raw materials are at least present. It has also been shown that organic materials—the building blocks of life on Earth—can form in space (e.g., in the tail of a comet (Sandford, 2009)). Therefore stars that have comet-like and/or organic material in their debris disks would point to planetary systems that might resemble our own.

In this thesis, I attempt to help answer some of the major questions in the field described above. Chapters 2 and 3 are largely concerned with characterizing the orbits (circular or eccentric) and true masses of RV-detected planets. Chapters 4-6 are largely concerned with characterizing the structure, morphology, and com-



positions of debris disks, as well as their dynamical interactions with planets. In Chapter 7, I summarize the results of my work and describe my plans for future research in the exoplanet field.

## 1.1 Orbits and Masses of Planets Detected by Radial Velocity

Aside from Mercury, the solar system planets all nearly-circular orbits, with eccentricity values  $< 0.1$ . However, the distribution of eccentricity values for planets detected by RV is skewed towards high eccentricities (<http://exoplanet.eu>). The orbital eccentricity of an RV-detected planet's is typically determined as part of a Keplerian fit to the periodic RV data. Since the RV method is inherently biased towards finding massive planets close to their host stars, planets on wider orbits are naturally difficult to detect—but they still contribute to the star's overall radial motion. Therefore these outer companions can bias the Keplerian-fitted data. Eccentricity is particularly sensitive to this bias.

Can additional undetected wide companions explain or account for the high number of eccentric RV planets? If so, what does this imply about the orbits of planets? Is our solar system then unique or ordinary? To answer these questions, in Chapter 2 I present my investigations into how eccentricity values for known RV planets are affected by as-yet undetected outer companions (Rodigas & Hinz, 2009). More specifically, I hypothesize that two planets in circular (zero eccentricity) orbits can masquerade as a single mildly-eccentric planet. While this effect alone cannot explain the complete observed RV eccentricity distribution, it does match the distribution when the effect is combined with a separate distribution of truly-eccentric single-planet systems (Jurić & Tremaine, 2008). Matching the observed distribution, I then predict what fraction of known RV systems might suffer from eccentricity bias—and therefore which systems might contain an ad-

ditional outer planet. This has important ramifications for understanding the demographics of exoplanets: while my models are not unique, they indicate that nature may consist of many more multi-planet systems with near-circular orbiting planets than previously thought, possibly implying our solar system may be more ordinary than unique. My results also highlight the importance of continued RV monitoring of known exoplanet systems, with additional direct imaging in favorable cases.

What makes a planetary system favorable for direct imaging? According to current models, wide-separation giant planets cool over time and are brighter in the near-infrared (NIR) than at other wavelengths, owing to their glowing heat leftover from formation (Burrows et al., 2003; Baraffe et al., 2003). Therefore planets are easier to directly image if they are *young*. It also helps for the system to be close to Earth, and for the planet to be far from its host star, since contrast usually decreases rapidly within  $\sim 10 \lambda/D$ , where  $\lambda$  is the wavelength of the observation and  $D$  is the telescope diameter.

Based on these requirements, nearly all of the planets directly imaged to date are young, nearby, and orbit far ( $\gtrsim 5$  astronomical units (AU)) from their host stars (e.g., Marois et al. (2010); Lagrange et al. (2010)). Only a handful of planets have been directly imaged, with most surveys yielding null results. Based on these null results, our current understanding of planetary system architectures is that planets more massive than Jupiter rarely have long-period orbits (Nielsen & Close, 2010). Most surveys conducted to date are sensitive to planets orbiting beyond  $\sim 20$  AU, and RV surveys are typically sensitive inside  $\sim 3$  AU. Microlensing studies have shown that planets can orbit well beyond the snow line (Gould et al., 2010), so many planets remain to be discovered in the  $\sim 3$ -20 AU range.

Direct imaging of RV systems is one way to study this particular orbital phase

space. Unfortunately, directly imaging RV planets is difficult. The host stars of RV planets are typically at least a few Gyr old, since the precise Doppler shifts used for detecting the planets requires the stars to be chromospherically inactive. Old planets are much dimmer, making them harder to directly detect. Additionally planets detected by RV mostly reside within  $\sim 3$  AU from their host stars; these planets, even at maximum elongation, would have a projected separation on the sky of no more than  $0''.3$  for a star at relatively nearby distance of 10 pc.

Since RV planet masses are reported as *minimum* masses ( $m \sin(i)$ ) due to the lack of information on the inclination to the system, directly imaging an RV-detected planet can remove the uncertainty and pinpoint the true mass of the object. The orbital motion of the object can also be followed over time, yielding a dynamical mass for the planet (e.g., Crepp et al. (2012a)), which can then be used to refine and constrain the atmospheric models currently used for estimating the masses of directly imaged exoplanets.

Planets on wide orbits are easier to detect than those orbiting close to their stars. This is where my work on the eccentricities of RV planets comes into play, hinting that there may be an additional population of wide-separation massive planets in current RV systems. Before a blind search or survey of systems is conducted based on this work, a more favorable case should be examined: RV systems with one or more planets and a long-term trend indicative of a massive outer companion. This was the motivation for imaging the 14 Her planetary system (Rodigas et al., 2011), which I discuss in Chapter 3. 14 Her is a nearby K star that has 1 confirmed RV planet and an outer, unconfirmed planet (14 Her c) suggested by a long-term trend in the residuals of the RV fits. I used Clio, Arizona's 1-5  $\mu\text{m}$  imager, at the MMT along with the MMT's deformable secondary mirror adaptive optics (AO) system to image the star for 2.5 hours in the  $L'$  band

( $3.8\ \mu\text{m}$ ). Planets are expected to have increasingly red  $H-L'$  colors as they age (Burrows et al., 2003). While no point sources were detected, we conservatively constrained the planet’s mass to be less than  $42\ M_J$  and its semimajor axis to be between 7 and 25 AU by combining our imaging data with the published RV data. In just a few hours of direct imaging I constrained phase space that would have required several additional years for RV follow-up, showing the power of direct imaging/RV overlap. These two complementary techniques, currently being used together to mainly detect and characterize brown dwarfs (e.g., Crepp et al. (2012b)), will surely be used together to characterize low-mass planets as high-contrast imaging technology improves.

## 1.2 NIR Imaging of Debris Disks

On Earth, life as we know it requires three key ingredients: liquid water, organic materials, and energy. In searching for planetary systems that may harbor extra-solar life, we must first identify which systems contain these ingredients. More specifically, we must determine *where* water ice is located in each system. Water ice is thought to play a crucial role in planet formation, as the cores of giant planets more easily form outside the “ice line” than inside it (Kennedy & Kenyon, 2008). Therefore detecting the locations of increased water abundance in extra-solar debris disks can tell us about where planets might have formed and where they might currently reside.

Locating extrasolar water ice reservoirs is also important for understanding how Earth acquired its vast oceans. The origin of Earth’s liquid water (and in fact, all the terrestrial planets’ water reservoirs) is not well-understood. It has been proposed that comets, scattered via gravitational interactions with the solar system’s gas giants, delivered water to Earth when they collided with Earth less

than 1 Gyr after forming (Gr  e J  rgensen et al., 2009). However, the ratio of deuterium to hydrogen in Earth’s oceans does not match ratios in current comets, implying that only a small fraction of Earth’s water could have been delivered by icy comets. Newer theories have been proposed, including Earth forming “wet” by adsorbion (Drake, 2005) onto fractal dust grains at the time of formation, but no conclusive evidence exists yet. Even if we do not currently understand *how* Earth acquired its water, comparing extrasolar systems with water to our own will help provide useful constraints and context for understanding volatile delivery to potentially habitable planets.

Water ice and organics have unique spectral features in the NIR window of the electromagnetic spectrum (1-5  $\mu\text{m}$ ). Both water ice and tholins–organic “goo” that has been identified on many comets and on Saturn’s moon Titan–have large absorption features near 3.1  $\mu\text{m}$ . Ideally we would obtain spectra of extrasolar debris disks directly, but most are too faint to achieve adequate signal-to-noise (S/N). Therefore the amount of water ice/organics must be probed using photometry of debris disks spanning the 2-4  $\mu\text{m}$  window.

Unfortunately, at these thermal wavelengths, the night sky is bright and every metal-coated surface in the optical path of the telescope glows as a greybody. These difficulties alone explain why very few resolved images of debris disks exist at these wavelengths. An adaptive optics (AO) system–in particular, one that limits the number of reflecting surfaces–can greatly improve imaging capabilities. The Large Binocular Telescope (LBT) AO system satisfies this requirement. Each primary mirror has its own adaptive deformable secondary mirror (ASM), resulting in  $\gtrsim 70\%$  Strehl-ratio images at  $\lambda > 2 \mu\text{m}$  (Esposito et al., 2010; Skemer et al., 2012; Rodigas et al., 2012). This makes detecting faint debris disks, in particular at 4  $\mu\text{m}$ , feasible. Below I describe the need for an AO system like the

LBT's for imaging faint debris disks in the NIR from the ground.

### 1.2.1 The Need for Adaptive Optics

The ability to detect faint sources like planets and disks in direct images depends on two properties: sensitivity and contrast. Both of these are significantly improved with AO systems like those employed at the LBT and Magellan. Conventional systems, like the Keck AO system, do not have ASMs, requiring multiple mirrors to correct for atmospheric turbulence. In the infrared, every metal-coated surface glows, meaning the thermal background is higher, which limits imaging sensitivity. ASMs, like those installed at the MMT, LBT, and Magellan, perform the AO correction directly, reducing the number of glowing surfaces and improving imaging sensitivity (Lloyd-Hart, 2000).

The second imaging property, contrast, is affected by the Strehl ratio of the corrected image. The Strehl ratio depends on the number of modes of wavefront error the AO system can correct for. The number of modes of correction is affected by several properties. The maximum number of modes of correction is theoretically limited by the number of actuators on the back of the thin shell ASM. At the MMT, which has an ASM with 336 actuators, the typical number of modes corrected is usually  $\sim 50$ -100. This is because correction also depends on the ASM thickness, the efficiency of the actuators, the calibration of the system, and the wavefront sensor system.

The MMT AO system employs a Shack-Hartmann (SH) wavefront sensor. SH sensors are typically located in the pupil (aperture) plane of the telescope, where lenslets reimage incoming light onto a detector. The centroids of the light on the sub-apertures are measured and compared to perfect wavefront positions. Therefore the accuracy of the correction in this set up depends on the centroid accuracy, which depends on the resolution of the incoming beams of light. Since the size

of the SH lenslets,  $d$ , is usually on the order of the size of turbulent airpockets (coherence length), which vary in size from  $\sim 10$  cm at visible wavelengths to  $\sim 50$ -100 cm at infrared wavelengths, the resolution of the light impinging on the detector is low. The AO correction in a SH sensor also typically suffers from aliasing, whereby high spatial frequency aberrations propagate into modes that are detected by the wavefront sensor (Guyon, 2005), degrading overall wavefront correction. Aliasing can be avoided by placing an aperture in the image plane that blocks out high spatial frequency light, but then the intensity of the signal decreases, meaning this should only be employed for bright guide stars.

A pyramid wavefront sensor (PWFS) avoids many of these problems by placing a prism in the image plane of the telescope (e.g., Ragazzoni (1996)). Due to the placement of the pyramid in the image plane, the size of the beams impinging on the detector is  $\sim \lambda/D$ , where  $D$  is the diameter of the telescope. This results in higher resolution, higher S/N images on the detector, allowing for more modes of AO correction. Aliasing is also less severe due to the higher resolution on the detector. A PWFS can also increase S/N on the detector with digital binning, which is much faster, easier to calibrate, and has less noise than the equivalent process of physically changing the number of sub-apertures in a SH sensor. The targets observed in this thesis are all bright ( $V < 8$ ), negating this additional advantage.

The LBT AO system (Esposito et al., 2010), along with the newly-commissioned MagAO system (Close et al., 2010), both use thin ASMs with 672 actuators and each uses a PWFS. Both systems have been extensively calibrated, improving on the results of the first ASM employed at the MMT, allowing for up to 300-400 modes of correction. This results in high Strehl ratio, high-contrast imaging capability in the NIR, which is necessary for detecting faint point and extended

sources.

### 1.2.2 Results on HD 15115 and HD 32297

In Chapter 4, I will present my first results of the debris disk imaging program, which were obtained as part of the First Light Adaptive Optics (FLAO) commissioning of the LBT AO system and published in 2012 (Rodigas et al., 2012). I obtained Ks ( $2.15\ \mu\text{m}$ ) and  $L'$  ( $3.8\ \mu\text{m}$ ) images of the edge-on debris disk around the nearby F star HD 15115. At visible wavelengths, the disk is highly-asymmetric and extends out to several hundred AU ( $\sim 12''$ , hence its former nickname, the “blue needle”; Kalas et al. (2007)). At Ks band, the disk is still asymmetric, with the eastern side of the disk clearly truncated relative to the western side. But the spatial extent of the disk is only  $\sim 100$  AU ( $2.5''$ ). At  $3.8\ \mu\text{m}$  the disk appears mostly symmetric, and the spatial extent is even more limited, falling off beyond  $\sim 60$  AU ( $1.5''$ ). Taken together, these data paint a different picture of the HD 15115 debris disk. Given the change in disk symmetry and spatial extent with wavelength, it appears that at long wavelengths, we are seeing scattered light from particles in more stable orbits, whereas at shorter wavelengths we are seeing the light from the dust particles being blown out by radiation pressure from the star. The change in symmetry fits well with a leading theory that the disk is plowing into an ISM bubble, causing the western side of the disk to appear truncated (Debes et al., 2008b). Based on the Ks- $L'$  disk colors, the best match to the data are large dust grains  $1\text{-}10\ \mu\text{m}$  in size. These large grains are responsible for the “gray” color we observe between Ks and  $L'$ , a sharp contrast from the bluer colors observed at shorter wavelengths.

Following up on this work, in Chapter 5 I will present my most recent imaging results on the bright debris disk surrounding the A star HD 32297. The disk has been imaged across several orders of magnitude in wavelength in the past,



but only recently have any attempts at modeling the dust size and composition been made (Currie et al., 2012c; Donaldson et al., 2013). Obtaining a high S/N detection of the disk at  $L'$  for the first time, I combine these new results with archival HST images of the disk at 1-2  $\mu\text{m}$ . With resolved images of the disk at 1-4  $\mu\text{m}$ , we compare the disk's spectrum and structure to various model disks of different dust grain compositions and sizes, including the cometary composition model proposed by Donaldson et al. (2013) from far-infrared spectral energy distribution analysis.

### 1.3 Dynamics of Dust Grains Shepherded by Planets

Since the first resolved images of debris disks over a decade ago, astronomers have noticed that nearly every disk is asymmetric and has a center misaligned with the star; some are very eccentric and have very sharp edges. It was proposed that such features were signs of shepherding planets. Kuchner & Holman (2003) showed how the morphology of debris disks changed depending on the mass and orbit of a single shepherding planet interior to the disk. Before the discovery of a point source in the Fomalhaut system, Quillen (2006) constrained the mass of a putative disk-shepherding planet that could produce the observed features of the disk using numerical simulations of parent bodies. Chiang et al. (2009) carried this analysis one step further by including simulations of dust in addition to parent bodies. They were able to better constrain the mass of the putative planet, discovered shortly before by Kalas et al. (2008) and later confirmed by Currie et al. (2012a); Galicher et al. (2012) (though the true nature and orbit of the object are still uncertain (Kalas et al., 2013)). Building on the work of Chiang et al. (2009), in Chapter 6 I extrapolate their models to the general case of a debris disk of a given eccentricity being sculpted by a planet of a given mass and orbit. The

goal is to provide observers with a means to estimate the mass and orbit of an as-yet undetected planet from scattered light images of the debris disk.

In Chapter 7, I summarize the main results of this thesis and present plans for future work in the field of exoplanets.

## CHAPTER 2

WHICH RADIAL VELOCITY EXOPLANETS HAVE UNDETECTED OUTER  
COMPANIONS?

The observed radial velocity (RV) eccentricity distribution for extrasolar planets in single-planet systems shows that a significant fraction of planets have eccentric orbits ( $e > 0.1$ ). However an RV planet's eccentricity, which comes from the Keplerian fitting, can be biased by low signal-to-noise and poor sampling. Here we investigate the effects on eccentricity produced by undetected outer companions. We have carried out Monte Carlo simulations of mock RV data to understand this effect and quantify its impact on the observed distribution. We first quantify the statistical bias of known RV planets' eccentricities produced by undetected zero-eccentricity wide-separation companions and show that this effect alone cannot explain the observed distribution. We then modify the simulations to consist of two populations, one of zero-eccentricity planets in double-planet systems and the other of single planets drawn from an eccentric distribution. Our simulations show that a good fit to the observed distribution is obtained with 45% zero-eccentricity double-planets and 55% single eccentric planets. Assuming our two simulated populations of planets are a good approximation for the true RV population, matching the observed distribution allows us to determine the probability that a known RV planet's orbital eccentricity has been biased by an undetected wide-separation companion. Averaged over eccentricity we calculate this probability to be  $\sim 4\%$ , suggesting that a small fraction of systems may have a yet to be discovered outer companion. Our simulations show that moderately-eccentric planets, with  $0.1 < e < 0.3$  and  $0.1 < e < 0.2$ , have a  $\sim 13\%$  and  $\sim 19\%$  probability, respectively, of having an undetected outer companion. We encourage

both high-contrast direct imaging and RV follow-up surveys of known RV planets with moderate eccentricities to test our predictions and look for previously undetected outer companions. A version of this chapter originally appeared as a published paper in the *Astrophysical Journal* (Rodigas & Hinz, 2009). All work described below was carried out by me, with helpful suggestions by Phil Hinz.

## 2.1 Introduction

Since the 1990s, over 300 extrasolar planets have been discovered (see, for example, <http://exoplanet.eu>). Exoplanets have been discovered by several different techniques, namely radial velocity (RV), transits, astrometry, microlensing, and most recently direct imaging (e.g., Kalas et al. (2008); Marois et al. (2008)). The RV method, which has discovered the majority, monitors the periodic velocity shifts (in the radial direction) of a given star. These velocity variations are caused by the star orbiting the barycenter of the combined system, which can contain additional companions (typically stars, brown dwarfs, and/or planets). The RV method allows one to extract the orbital period of the companion ( $P$ ), its semi-major axis  $a$ , the lower limit to its mass ( $m \sin i$ ), and its eccentricity ( $e$ ). Since there are  $\sim 300$  RV-discovered exoplanets, we have a large enough sample to construct distribution functions for each of these quantities.

Of these distributions, the eccentricity distribution is the most puzzling. In our own solar system, planets have very low eccentricity values (nearly circular orbits). Jupiter, the gas giant to which we compare discovered extrasolar planets, orbits with  $e = 0.05$ . While the RV extrasolar planet eccentricity distribution has a strong peak near  $e = 0$ , it also has a significant tail extending all the way out to  $e = 0.93$  (see Fig. 2.1). If our solar system and its planets are common and ordinary, then we would expect most exoplanets to have low eccentricities.

Clearly this is not the case.

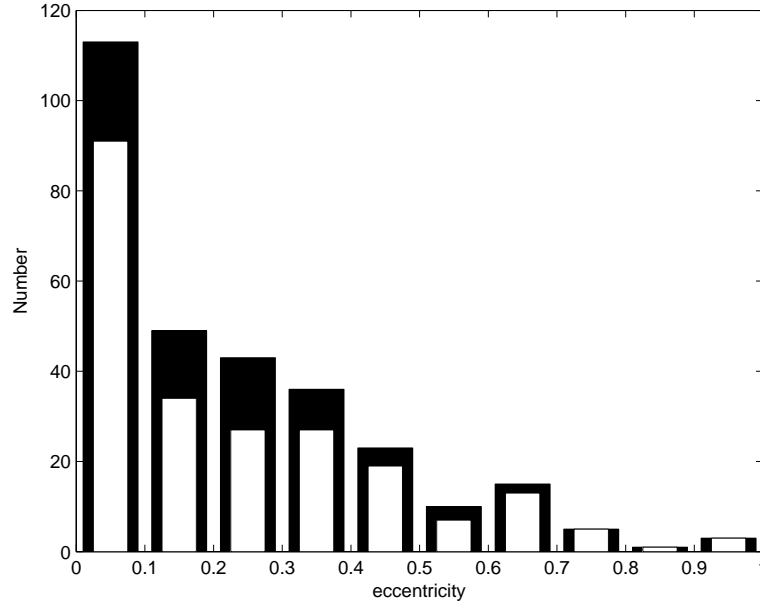


Figure 2.1 The observed RV eccentricity distribution (black bars) and the observed *single-planet* RV eccentricity distribution (white bars), both from <http://exoplanet.eu> as of January 2009. We compare our simulations only to the single-planet distribution because we hypothesize that undetected outer companions bias *one-planet* Keplerian fits. Note the large number of high eccentricity ( $e > 0.1$ ) planets.

There have been many attempts to explain the observed eccentricity distribution. Most of these focus on planet-planet interactions and scattering (e.g. Rasio & Ford (1996); Levison et al. (1998); Adams & Laughlin (2003); Jurić & Tremaine (2008)). These interactions can build up the eccentricities of two or more planets, resulting in scattering or ejection. In the process, the remaining planets settle down into stable, high-eccentricity orbits. While scattering is certainly plausible and can match the  $e \gtrsim 0.2$  observed eccentricity distribution, it is unclear whether

the majority of planetary systems go through such violent planet-planet interactions.

Other factors may be at play. Shen & Turner (2008) explored the effects of RV systematics on eccentricity. They showed that planets' eccentricities can increase with lower signal-to-noise ratios (SNR), given by  $K/\sigma$ , where  $K$  is the velocity semi-amplitude and  $\sigma$  is the experimental error (typically depending on the telescope and instrument error as well as stellar jitter). Specifically  $e$  increases for  $K/\sigma \lesssim 3$ . They also show that eccentricity increases with fewer observations in a given RV data set ( $N_{obs} \lesssim 60$ ). Here, the number of observations is the number of data points in a star's radial velocity curve. Since the SNR and  $N_{obs}$  conditions are not always met for RV data, especially for the earliest discoveries, we can expect that this bias plays a role in the observed eccentricity distribution. Shen & Turner (2008) estimated that about 10% of RV-detected exoplanets are affected by this bias.

Undetected additional planets in planetary systems can also affect RV eccentricities. When two planets orbit a star, both contribute to the star's radial velocity. Assuming the planets are not gravitationally interacting with each other, one produces the total radial velocity curve by adding the radial velocity data from each planet. One can detect the second planet by monitoring the star long enough to observe its full period. Since this time frame is usually  $\gtrsim 10$  years, only  $\sim 20$  multiple-planet systems have been discovered. If one observes a double-planet system for a duration shorter than the period of the second planet, a long-term trend can appear in the data. Fischer et al. (2001) explored the possible bias introduced by *wide-separation planets* by injecting real long-term trend data into some of their existing one-planet RV data. After fitting the new data, they found that the mass and semi-major axis of the original planet were mostly unchanged, but

that its eccentricity value increased, sometimes by as much as  $\Delta e = 0.25$ . They were able to detect the long-term trends only in cases where there was dense phase coverage (large  $N_{obs}$ ) and high SNR. These results are very important for several reasons: they confirm the effects of the systematic biases discussed by Shen & Turner (2008), and they show that *undetected* additional companions can drive up a known planet’s eccentricity value. Nonetheless, we cannot draw large-scale conclusions since the Fischer et al. (2001) results were based on a small sample of tests, and the test parameters were not significantly (randomly) varied.

To determine the full effect of undetected wide-separation planets on eccentricity, we have carried out Monte Carlo simulations of mock RV data. We first determine the statistical effect of undetected wide-separation companions on eccentricity. We then try to match the observed eccentricity distribution with a population of zero-eccentricity planets in double-planet systems. We show that this population alone cannot describe the observed eccentricity distribution, and we therefore need a second input population of high-eccentricity planets. After matching the observed distribution, we derive the probability that a known planet has a wide-separation companion, information potentially important for both RV follow-up surveys and direct imaging. In §2.2, we describe the simulations, test parameters, and methodology. In §2.3, we present the results and discuss the implications. In §2.4, we summarize and conclude.

## 2.2 Simulation Parameters and Methodology

An RV-detected planet’s orbital parameters ( $m \sin i$ ,  $a$ , and  $e$ ) are determined from the Keplerian fit to the star’s radial velocity data. The equations needed to calculate the star’s radial velocity are:

$$V_{rad} = V_0 + K [\cos(\omega + T) + e \cos(\omega)] \quad (2.1)$$

$$K = \sqrt{G/(M_* + m)} m \sin i / \sqrt{a(1 - e^2)} \quad (2.2)$$

$$T = 2 \tan^{-1}[\tan(E/2) \sqrt{(1 + e)/(1 - e)}] \quad (2.3)$$

$$E = M + e \sin E \quad (2.4)$$

$$M = (t - t_0) \frac{2\pi}{P}. \quad (2.5)$$

$P$  is the orbital period of the planet,  $t$  is the time of the observation,  $t_0$  is the time of perihelion, and  $M$  is the mean anomaly.  $E$  is the eccentric anomaly and since it is given in a transcendental equation it cannot be solved analytically. For our simulations, we solve for  $E$  using iterative loops.  $T$  is the true anomaly,  $K$  is the velocity semi-amplitude, and  $\omega$  is the argument of the perihelion. We have set  $\sin i = 1$ , assuming edge-on systems in all cases.  $V_0$  is the velocity offset which for simplicity we have set to zero.  $M_*$  and  $m$  are the mass of the star and planet, respectively. Since most RV stars are solar-type stars, we set  $M_* = M_\odot$ .

Our simulations, aside from control simulations, consist of 100 sets of  $N$  RV curves.  $N = 227$  since, as of January 2009, there are 227 single-planet RV systems (<http://exoplanet.eu>). Thus we simulate  $\sim 10^4$  total planets. We do not simulate the total number of observed RV systems because some of these ( $\sim 30$  systems) have multiple planets. Our hypothesis applies only to single-planet RV detections.

For each simulated planet, we draw  $\omega$  randomly from a uniform distribution in the range  $[0, 2\pi]$  and  $t_0$  in the range  $[0, P]$ , where  $P$  is the period of that particular planet. Each planet's semi-major axis  $a$  and mass  $m$  are drawn randomly from the most current RV distribution functions, regardless of being in a single or double-planet system. From the Butler et al. (2006) catalog of exoplanets, these are  $dN/dM \propto M^{-1.1}$  and  $dN/d \log a \propto a^{0.4}$ . In simulated systems, the first planet has  $a_{inner} \in [0.05, 3]$  AU and the second has  $a_{outer} \in [7, 15]$  AU. The first planet's



orbital range was chosen because most RV-detected planets are found within 3 AU, and the closest planets have periods on the order of a few days ( $= 0.05$  AU). We acknowledge that the Butler et al. (2006) minimum semi-major axis used to derive the distribution function was  $a \sim 0.1$ , but this difference is insignificant. It is also true that RV has found some planets beyond 3 AU, but the statistics are poor for this small sample. The second planet's orbital range was chosen for several reasons: gas giants in our solar system (Jupiter, Saturn) orbit in this range, and we wanted to avoid any resonances  $< 2:1$  that might, via secular interactions, lead to higher eccentricity values. In fact, the smallest resonance we allow is  $\sim 3.5 : 1$  (outer planet at 7 AU, inner planet at 3 AU). Our simulations are testing stable relaxed planetary systems, and the eccentricity bias we are investigating is not from planet-planet interactions but rather from the Keplerian fitting. While the solar system planets' orbits are more closely spaced than the orbits we are simulating here, we do not simulate such closely-packed systems because these systems would produce long-term trends in the RV data. The goal of this study is to determine the effect of long-period companions on *single-planet* systems, so no long-term trend can be present.

The mass range for the first planet was chosen to be  $m_{inner} \in [0.01, 25] M_J$  ( $M_J$  is the mass of Jupiter). These limits reflect the  $\sim$  minimum and maximum mass planets discovered by RV so far (<http://exoplanet.eu>). The mass range for the second planet was chosen to be  $m_{outer} \in [m_{inner}/M_J, 25] M_J$ . If a planetary system has two planets, then the outer planet is probably at least as massive as the inner. Though speculative, there is some evidence for this in Wright et al. (2009), who show that there is on average a 1-1 correspondence in mass for the RV-discovered two-planet systems. It is possible that this result is biased by the fact that more distant planets have to be more massive to be detected by the RV

method. Nonetheless most multiple-planet systems have been discovered by RV, so the sample in Wright et al. (2009) is the largest and most statistically-significant sample from which to draw conclusions.

For each simulation, we compute the star’s radial velocity  $V_{rad}$  at 32 points in time over  $2P$ . In all cases (one-planet system or two-planet system),  $P$  is the period of the inner planet. We have chosen 32 data points because this is a moderate amount of observations. We acknowledge that since  $N_{obs} = 32 < 60$ , eccentricities will be slightly biased (as described by Shen & Turner (2008)). Nonetheless,  $N_{obs} = 32$  is a reasonable assumption given the typical  $N_{obs}$  for an actual RV data set. We have chosen to simulate each system’s data for two periods because most RV data is published with at least two periods of coverage. We emphasize that the 32 data points along each RV curve are not equally spaced. This would not be realistic. Instead we have tried to mimic the “clustering” of data points seen in typical RV data (see Fig. 2.2). To accomplish this, we divide a given simulated data set into 8 zones, each containing 4 points (observations). In each zone, the first point’s location is determined randomly. The subsequent points’ locations are also determined randomly, but the inner boundary for each is the location of the previous point. This causes an apparent grouping, or clustering, of observations in each zone.

If there are two planets in a simulated system, we compute the radial velocity independently for each planet and then add them together to get the total  $V_{rad}$ . In all cases, we add Gaussian noise with  $\sigma = 5$  m/s to  $V_{rad}$ . This  $\sigma$  was chosen as a good estimate of typical RV precision. Because we enforce  $K > 3\sigma$ , changing  $\sigma$  to a higher (potentially more RV-representative) value (say, 10 m/s) would have little to no effect on our results. All simulations were carried out in Matlab. To determine the orbital parameters, we cycle through  $e$  from 0 to 0.99, hold  $e$  constant

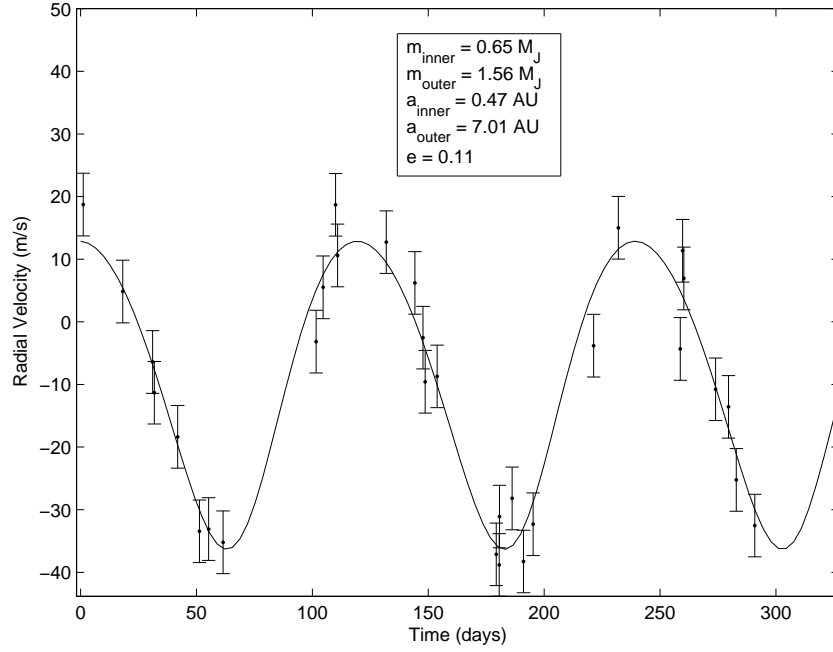


Figure 2.2 Typical radial velocity plot from the simulations. In this case there are two planets in the system, both contributing to the star’s radial velocity. There is no apparent long-term trend from the second planet evident in the data, but the fitted eccentricity has increased from  $e = 0$  to  $e = 0.11$ .

at each value, and fit for the other orbital parameters. We then take the lowest  $\chi^2$  solution, along with its corresponding  $e$ , as the final set of orbital parameters. Because we know the input parameters for each simulated system beforehand, we do not use periodograms and false-alarm probability tests in our fitting procedure. When fitting a data set, we only fit for *one* planet because we are testing the effects of *undetected* wide-separation planets on eccentricities. To ensure that the outer planets do not create long-term trends in the data, we enforce  $\chi^2_{reduced} < 3$ . This limiting value was chosen because RV data with poorly-constrained fits are rarely published; if they are, the authors typically suggest that a long-term trend

is present and attempt a two-planet Keplerian fit.

## 2.3 Results and Discussion

### 2.3.1 Control Simulations

Before running our full suite of simulations, we checked that our Keplerian fitting was working correctly. To test this, we simulated 50 sets of  $N = 227$  single-planet systems ( $\sim 10,000$  planets). Each planet’s semi-major axis and mass were drawn from the appropriate distributions. We set  $e$  to zero, which allows us to directly measure any unforeseen effects on eccentricity. If the fit is working correctly, then the output parameters for each planet should match the input parameters within experimental error.

Fig. 2.3 shows the relationships between  $a_{\text{output}}$  and  $a_{\text{input}}$ , and  $m_{\text{output}}$  and  $m_{\text{input}}$ . The tight linear relationships and slopes of unity show that our Keplerian fitting has no effect or bias on a planet’s semi-major axis or mass. Fig. 2.4 shows the average distribution of fitted eccentricity values, normalized to the first bin. Fig. 2.4 reveals that  $\sim 8\%$  of planets are eccentric ( $e > 0.1$ ). This small bias is due to the effects discussed by Shen & Turner (2008). Namely, our  $N_{\text{obs}} = 32 < 60$ , which is the suggested number of observations. Furthermore, although Shen & Turner (2008) did not explore this, we believe that the “clustering” of data points also affects a planet’s eccentricity. This is a typical feature of published RV data, so we have chosen not to ignore it.

Having confirmed the validity of our Keplerian fitting routine, the next step was to quantify the statistical effects of *undetected* wide-separation planets on one-planet fits. To this end, we simulated 100 sets of  $N \simeq 100$  two-planet systems ( $\sim 10,000$  planetary systems). Each planet’s semi-major axis and mass were drawn from the appropriate distributions, and we again fixed  $e$  at zero. Com-

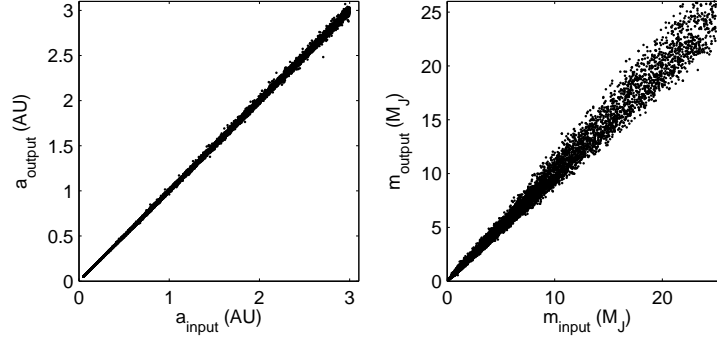


Figure 2.3 *Left*: output semi-major axis as a function of the input semi-major axis for the control simulation (one-planet systems). *Right*: the same, except showing the relationship between output and input mass. In each case, the tight linear relationships and slopes of unity verify that our simulations have no unforeseen effects on a given planet's semi-major axis or mass.

paring the results of these double-planet simulations to those of the single-planet simulations yields the second planet's effects on the first planet's parameters. Fig. 2.5 shows the relationships between  $a_{\text{output}}$  and  $a_{\text{input}}$ , and  $m_{\text{output}}$  and  $m_{\text{input}}$ . In all cases,  $a$  and  $m$  are the semi-major axis and mass of the *inner* planet. Fig. 2.5 shows tight linear relationships with slopes of unity. Evidently wide-separation planets have no effect on the inner planet's mass and semi-major axis, although there is certainly more scatter. These results agree with the previous work by Fischer et al. (2001).

Fig. 2.4 also shows the average distribution of fitted eccentricity values for

two-planet systems. The percentage of planets with  $0.1 < e < 0.2$  is  $\sim 13\%$ , and the total percentage of planets with  $e > 0.1$  is  $\sim 18\%$ . Thus the addition of the second planet can increase the eccentricity of the first planet. Knowing that the  $N_{obs} < 60$  effect accounts for  $\sim 8\%$  of the biased eccentricities, the sole effect from wide-separation planets is  $\sim 10\%$ . We note that “wide-separation” means  $7 < a_{outer}/\text{AU} < 15$ , the final range we settled on. We have also tested other semi-major axis ranges of different extents, such as  $[10,30]$  AU. In general, we saw that the larger the semi-major axis range, the lower the eccentricity bias. This makes sense given the RV equations (Eqs. 1-5); closer planets increase the velocity semi-amplitude  $K$  which in turn affects  $V_{rad}$  and the parameters of the fitted planet. In our simulations, however, bringing the second planet closer in does not necessarily induce more eccentricity bias. This is because the Keplerian fit becomes poor and the system is rejected. Therefore there is a “sweet spot” ( $\sim 7$  AU) where eccentricity is slightly biased, no long-term trend appears in the data, and the Keplerian fit converges.

The double-planet eccentricity distribution in Fig. 2.4 led us to draw two additional conclusions. First, our results agree with those of Fischer et al. (2001). The particular scatter in eccentricity values ( $e$  as high as  $\sim 0.3$ ) matches the maximum  $\Delta e$  they reported. If we relaxed our fitting constraints, then we would surely see higher eccentricity values. Therefore our agreement with the Fischer et al. (2001) result suggests that our fitting constraints (in particular  $\chi^2_{reduced} < 3$ ) are acceptable. Second, we cannot match the *observed* single-planet RV eccentricity distribution (Fig. 2.1) with *only* zero-eccentricity double-planet systems. Fig. 2.4 at best only matches the  $e < 0.2$  observed distribution shown in Fig. 2.1. Consequently we can reject the notion that the observed distribution can be explained by 100% zero-eccentricity double-planet systems. This result has

two interesting implications. It lends more support to the growing evidence that the true RV population consists of a significant fraction of high-eccentricity planets in single-planet systems; and, following from this conclusion, our solar system, as current evidence continues to show, is probably not ordinary. This is to say that the number of planets in our solar system and the low eccentricity of each is uncommon. If we had been able to match the observed eccentricity distribution with 227 zero-eccentricity double-planet systems, we could suggest that multiple-planet systems with low-eccentricity planets (like our own) may be more common than previously believed. However our simulations show that multiple-planet systems cannot be the entire story.

### 2.3.2 Matching the Observed Eccentricity Distribution

Our preliminary results show that we cannot match the observed single-planet eccentricity distribution with only zero-eccentricity double-planet systems. High-eccentricity planets in single-planet systems must constitute a significant fraction of the true RV population. Therefore, in addition to a simulated population of zero-eccentricity double-planets, we introduce a second population of single truly-eccentric planets. When simulating a truly-eccentric single planet, we draw its eccentricity value randomly from the Schwarzschild (Rayleigh) distribution for eccentricity  $e$ , given by

$$dN/de = \frac{e}{\sigma_e^2} \exp\left(\frac{-e^2}{2\sigma_e^2}\right), \quad (2.6)$$

with  $\sigma_e = 0.3$ . This is the distribution in eccentricity one would expect to see from gravitational scattering of astronomical bodies, whether they are stars or planets. Furthermore, Jurić & Tremaine (2008) used it to generate eccentricities in their simulations, and it matches the  $e \gtrsim 0.2$  observed eccentricity distribution very well.

Fig. 2.6 shows the results of our final simulations, comparing three simulated distributions to the observed single-planet eccentricity distribution from <http://exoplanet.eu>. The ratio of double-planet systems to total systems ( $\equiv R$ ) varies for each of the different simulations between 30%, 45%, and 65%. Fig. 2.6 shows that the  $R = 30\%$  case underestimates the number of low-eccentricity planets and overestimates the number of high-eccentricity planets. The  $R = 65\%$  case shows the opposite. The  $R = 45\%$  distribution is visibly the best match, with each point at or within 1 sigma of the observed distribution. This case also had the lowest  $\chi^2_{reduced}$  value ( $= 1.74$ ) compared to the other two distributions, which had  $\chi^2_{reduced} > 2$ . Fig. 2.7 shows the cumulative distribution functions of the simulated and observed distributions. Again the overall agreement is evident for the  $R = 45\%$  distribution. We also performed a two-sample K-S test for the  $R = 45\%$  case. The null hypothesis was that this simulated distribution and the observed distribution from <http://exoplanet.eu> were the same. The two-sample K-S test showed that the null hypothesis could not be rejected at the  $\alpha = 0.05$  significance level (95% confidence), supporting the notion that the  $R = 45\%$  distribution matches the observed distribution very well. These statistical results, as well as the final simulation parameters, are detailed in Table 1.

To zero in on the optimal ratio  $R$ , we carried out several simulations that varied  $R$  around 45%. Together with the  $R = 30\%$  and  $65\%$  simulated distributions, we were able to quadratically fit  $\chi^2_{reduced}$  as a function of  $R$ . This yielded a minimum  $\chi^2_{reduced}$  of 1.6, corresponding to  $R_{min} = 42^{+8.2}_{-8.7}\%$  (1-sigma limits).

In a two-planet system, what determines if the fitted planet's eccentricity is biased? We already know the effect depends on the semi-major axis and mass of the second planet from Eqs. 1-5, but which of these is the dominating factor? Fig. 2.8 shows the ratio of the semi-major axes and the ratio of the masses of the two



Table 2.1 Summary of simulation parameters and results

Number of planetary systems ( $N$ )	227
Number of simulations	100
$m_{inner}$	$[0.01, 25] M_J$
$m_{outer}$	$[m_{inner}, 25 M_J]$
$a_{inner}$	$[0.05, 3] \text{ AU}$
$a_{outer}$	$[7, 15] \text{ AU}$
$e_{single}$	$[0, 1]$
$e_{double}$	0
Ratio of double-planet systems to total systems ( $R$ )	45%
$\chi^2_{reduced}$	1.74
Interpolated $R_{min}$	$42^{+8.2}_{-8.7}\%$
Interpolated minimum $\chi^2_{reduced}$	1.6

planets in each double system as a function of fitted eccentricity. From Fig. 2.8 it is evident that a lower  $e$  means a larger separation between the two planets, and a higher  $e$  corresponds to a smaller separation. There is no apparent correlation in mass with eccentricity. This tells us that in a one-planet Keplerian fit, the fitted eccentricity value depends much more on how far away the second planet is than on how massive it is.

### 2.3.3 Eccentricity as an Indicator of Multiplicity

The ratio  $R$  tells us the fraction of simulated systems that have wide-separation companions, but we do not know which known RV systems might be affected by outer-planet bias. Because we have succeeded in matching the observed eccentricity distribution, we can use eccentricity as an indicator of exoplanet multiplicity. We stress that the discussion hereafter assumes that our two simulated input

distributions of planets are a good approximation for the true RV population. To determine what information about multiplicity a planet's eccentricity yields, we calculate the probability that an RV-detected planet's eccentricity has been biased by a wide-separation companion. Fig. 2.9 plots the ratio of the average number of double-planet systems to total systems as a function of fitted eccentricity. The first bin ( $0 < e < 0.1$ ) has a possible degeneracy in eccentricity: a planet with an eccentricity in this range either lives alone or has an extremely distant companion. In both cases, the eccentricity value is low and unbiased. We have therefore set the first bin to zero by subtracting off the control simulation bias (see Fig. 2.4). In this way any unforeseen bias introduced in our simulations would not corrupt our probabilities.

From Fig. 2.9, the probability that a given planet with any eccentricity ( $0 < e < 1$ ) has an undetected outer companion is  $\sim 4\%$ . For  $e \geq 0.1$ , any wide-separation companions have small enough orbital separations to induce effects on fitted eccentricity. For  $0.1 < e < 0.4$ , the average probability is  $\sim 10\%$ . This value increases to 13% and 19% if we consider planets with  $0.1 < e < 0.3$  and  $0.1 < e < 0.2$ , respectively.

Thus we now have a specific range in eccentricity values that can be used for observation target selection. From <http://exoplanet.eu>, there are 84 planets (in single-planet systems) with  $0.1 < e < 0.4$ , 57 planets with  $0.1 < e < 0.3$ , and 30 planets with  $0.1 < e < 0.2$ . Therefore, with the corollary stated above, we estimate that about 16 known RV planets should have wide-separation companions. We encourage high-contrast direct imaging observations of these targets to look for potential wide-separation companions. For a small target sample size, we suggest that direct imaging surveys focus on RV planets with  $0.1 < e < 0.2$  or  $0.1 < e < 0.3$  where the probabilities are highest. In this case, our simulations

Table 2.2 RV follow-up/direct imaging observing strategy

RV planet's eccentricity	Comments	RV Follow-up	Direct Imaging
$e < 0.1$	eccentricity yields no information on likelihood of outer companion	NO	?
$0.1 < e < 0.4$	$\sim 10\text{-}20\%$ chance of having an outer companion	YES	YES
$0.4 < e < 1$	extremely unlikely to have outer companion	NO	NO

predict that between 6-10 RV planets should have wide-separation companions, depending on which eccentricity range is used.

Our results are important for RV follow-up surveys as well. We again suggest looking at planets with  $0.1 < e < 0.3$ . For the zero-eccentricity planets, there is certainly the possibility that they are not part of multiple-planet systems, in which case RV follow-up would yield null-results. If these planets do have wide-separation companions, they are probably so far away that RV follow-up would require extremely long observation time frames to detect anything. However for  $e > 0.1$ , RV follow-up could reveal long-term trends and potentially extract the periods of wide-separation companions, since our simulations predict that such planets would not be too distant relative to the inner planets (see Fig. 2.8). We summarize the suggested observational strategy for RV follow-up and direct imaging in Table 2.

### 2.3.4 Why Not Observe Zero-Eccentricity RV Planets?

One might wonder why we do not advocate direct imaging of known RV planets with zero orbital eccentricity. After all, Fig. 2.8 shows that the two-planet systems with the most distant companions correspond to inner planets with nearly zero eccentricity. The more distant a planet is from its host star, the easier it is to directly image. However, because the outer planets have *no effect* on the inner planets' eccentricities, we cannot obtain any information about the systems' multiplicities; we have no way to determine if a zero-eccentricity RV planet lives alone or has a distant companion. Therefore if one had to choose between directly imaging moderately-eccentric RV planets (where we can quantify the probability that it has an outer companion) or zero-eccentricity planets, we recommend observing the moderately-eccentric planets. We cannot rule out the possibility that the RV population consists of a separate population of zero-eccentricity planets in single-planet systems. We do not entirely discourage direct imaging of zero-eccentricity planets, but the statistically favorable choice is to observe moderately-eccentric planets (see Table 2).

### 2.3.5 The Uniqueness Problem

Our simulations and results make interesting predictions, but the distributions used to fit the observed data are not unique. It is possible that other models with different parameters and assumptions could similarly reproduce the observations. Nonetheless we feel our results are important and worth further investigation because we have approached the problem from observational, theoretical, and physical standpoints. The distribution functions for semi-major axis and mass were obtained from statistical analysis of observed RV data. The orbital ranges and masses were determined from both observational data and theoretical assumptions. These were: in stable relaxed planetary systems, planets should

orbit outside 2:1 resonances; and if a planetary system has two planets, the outer should be at least as massive as the inner (Wright et al., 2009). Furthermore, with time the number of multiple-planet systems (and systems with long-term trends) discovered by RV has continued to increase, hinting that multiple-planet systems may be more common than the current statistics show. From the physical standpoint, if not all planetary systems have significant planet-planet interactions and scattering, then we might reasonably expect there to be two independent distributions of planetary systems. The planets unaffected by scattering would have  $e \sim 0$ , while the scattered population of planets would have eccentricities drawn from the Schwarzschild distribution as we have modeled. In this case our two distributions of planets provides a good description of the RV planet population. The predicted frequency of an outer companion provides the key observational test for this conclusion.

## 2.4 Conclusions

We have carried out Monte Carlo simulations of mock RV data to determine the statistical effect of undetected wide-separation companions on eccentricity. We quantify this effect and show that, for a given simulated population of planets, the number of eccentric planets increases by  $\sim 10\%$  when the outer companion is introduced. Thus undetected outer companions in RV planetary systems can have a small but important effect on the inner planet's Keplerian-fitted eccentricity. We show that the observed RV single-planet eccentricity distribution cannot be matched by 100% zero-eccentricity planets in double-planet systems, but rather an additional population of high-eccentricity planets in single-planet systems is required. This result lends support to the growing evidence that our solar system, with many low-eccentricity planets, is probably not ordinary. It also

agrees with the current RV statistics, which show that high-eccentricity planets constitute a significant portion of the RV population. This is supported by our simulations requiring low-eccentricity double-planets to constitute less than half of the total population, with the best-fitting ratio  $R = 42^{+8.2}_{-8.7}\%$ .

Assuming our two simulated populations of planets are a good approximation for the true RV population, we can make predictions about RV planet multiplicity using eccentricity. To do this we calculate the probability that a known RV planet's eccentricity has been biased by a wide-separation companion. Averaged over eccentricity this probability is  $\sim 4\%$ . For  $0.1 < e < 0.3$  and  $0.1 < e < 0.2$ , the probability is 13% and 19%, respectively. To test our predictions about the true RV population of planets, RV exoplanet multiplicity, eccentricity as an indicator of multiplicity, and to look for previously undiscovered outer companions, we encourage both high-contrast direct imaging and RV follow-up surveys of known RV single-planets with moderate eccentricities.

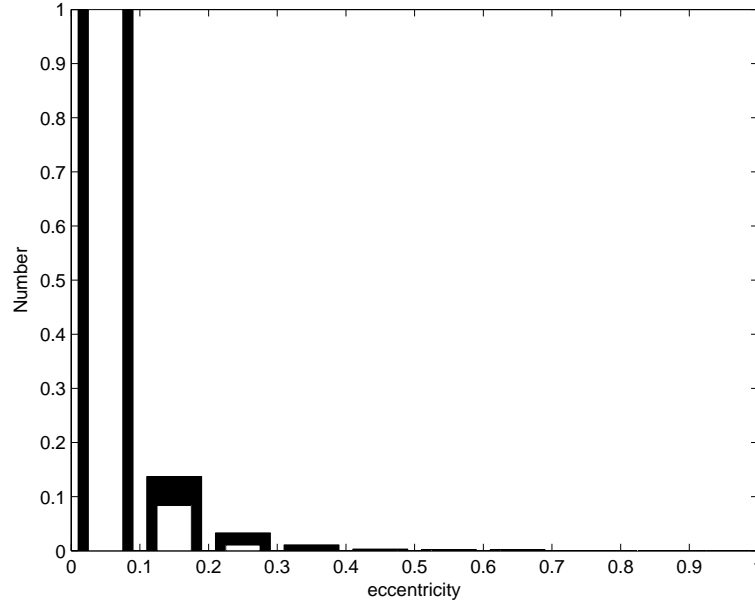


Figure 2.4 Eccentricity distribution for the control simulation (one-planet systems) (white bars), and the eccentricity distribution for simulated two-planet systems (black bars), both normalized to the respective first bin. All planets had their input eccentricities set to zero. For one-planet systems, 8% of the simulated planets' fitted eccentricities have increased, most likely due to biases coming from low SNR and poor sampling (discussed in Shen & Turner (2008)). When the wide-separation companions are introduced, the fraction of eccentric ( $e > 0.1$ ) planets increases by  $\sim 10\%$  to  $\sim 18\%$ .

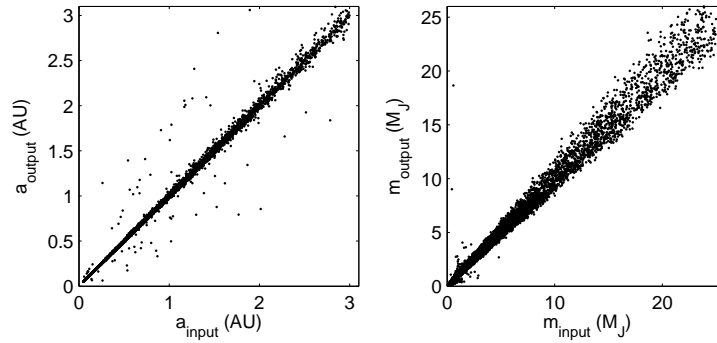


Figure 2.5 *Left*: output semi-major axis as a function of the input semi-major axis in simulated systems with two planets, both with zero eccentricity. *Right*: the same, except showing the relationship between output and input mass. In both cases, some outliers have been clipped. The tight linear relationships and slopes of unity show that wide-separation companions have a negligible effect on the fitted semi-major axis and mass, which agrees with expectations and the previous work by Fischer et al. (2001). It is worth noting, however, the increased scatter in output semi-major axis as compared to output mass. This suggests that semi-major axis is the more easily affected quantity.



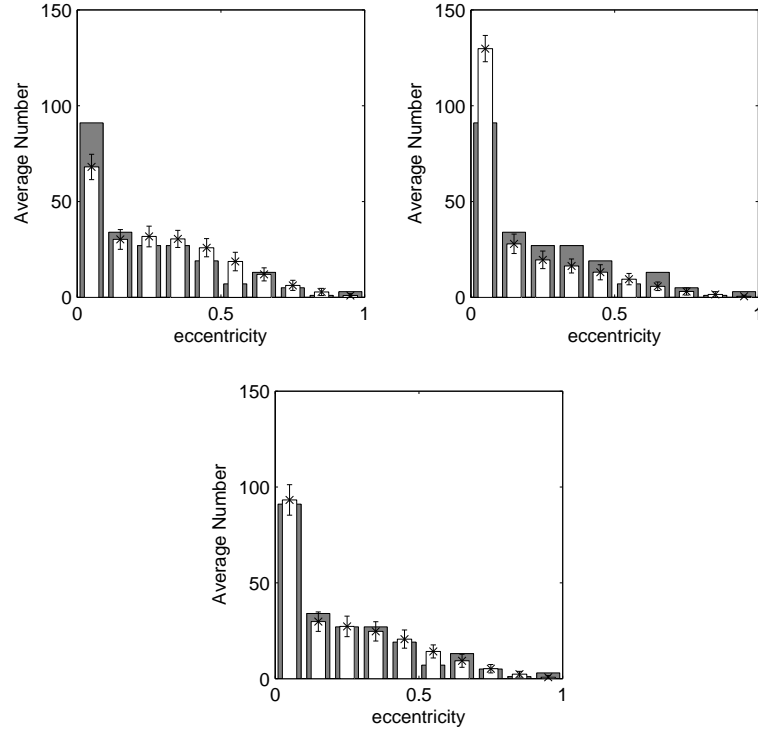


Figure 2.6 Simulated eccentricity distributions (skinny white bars with markers and error bars in all three plots) and the observed single-planet eccentricity distribution (wide grey bars in all three plots) from <http://exoplanet.eu>. *Top-left*: simulated distribution for  $R = 30\%$ . The number of low-eccentricity planets is underestimated and the number of high-eccentricity planets is overestimated. *Top-right*: simulated distribution for  $R = 65\%$ . This time the number of low-eccentricity planets is overestimated and the number of high-eccentricity planets is underestimated. *Bottom*: simulated distribution for  $R = 45\%$ . This distribution matches the observed single-planet eccentricity distribution very well ( $\chi^2_{reduced} = 1.74$ , disagreeing only around  $e \sim 0.55$  where the observed distribution dips down, most likely due to small-number statistics).

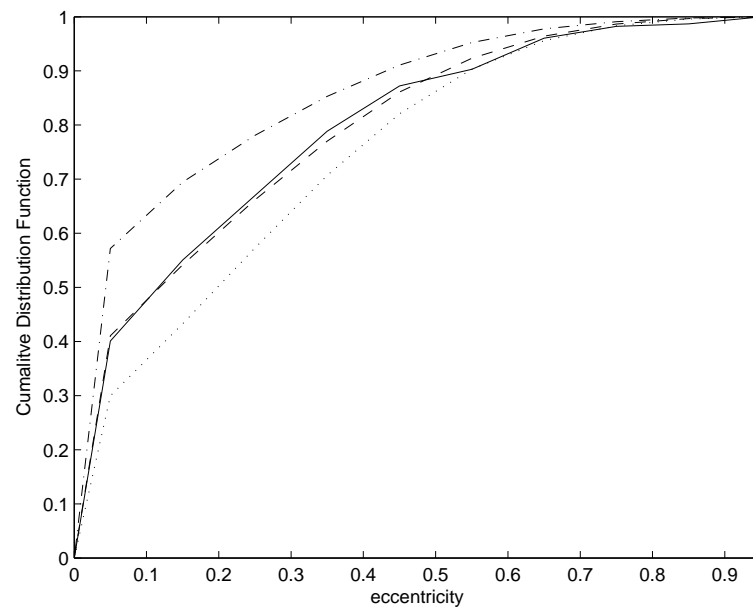


Figure 2.7 Cumulative distribution functions of the simulated eccentricity distributions for  $R = 30\%$  (dotted line),  $45\%$  (dashed line),  $65\%$  (dot-dashed line), and the observed single-planet eccentricity distribution (solid line). The  $R = 45\%$  curve matches the observed, but the  $R = 30\%$  and  $R = 65\%$  do not agree.

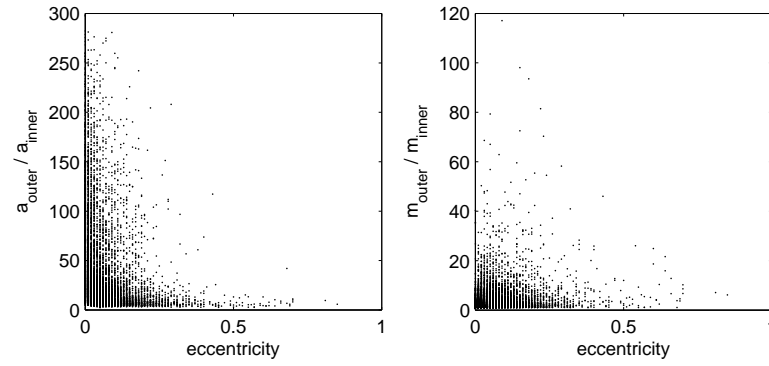


Figure 2.8 *Left*: ratio of the semi-major axes of the two planets in each simulated two-planet system as a function of fitted eccentricity. *Right*: the same, except the ratio of the masses. The semi-major axis ratio increases for low eccentricity and decreases for high eccentricity, but there is no apparent correlation between mass ratio and eccentricity. This suggests that fitted eccentricity is much more dependent on the separation between two planets than on the ratio of their masses.

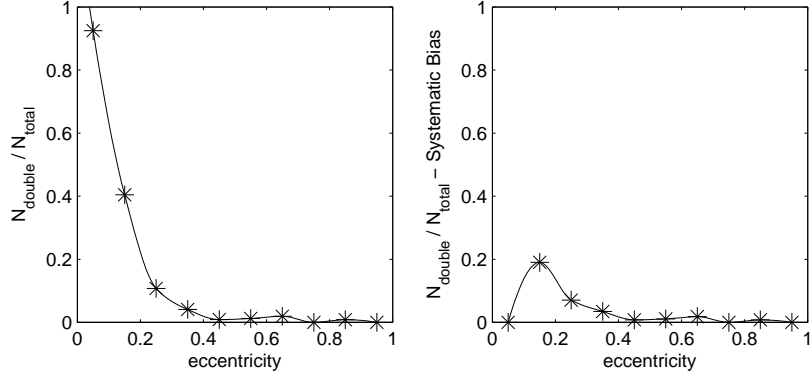


Figure 2.9 *Left*: ratio of double-planet systems to total systems as a function of fitted eccentricity. We cannot take these results at face value because the RV systematic biases (low SNR, poor sampling) have not been accounted for and subtracted off. *Right*: probability that a known RV planet’s eccentricity has been biased by an undetected wide-separation companion. To produce this plot, the control simulation bias (see Fig. 2.4) has been normalized to the first bin and subtracted off, explaining the first bin’s zero probability. In actuality planets with  $0 < e < 0.1$  have some small non-zero probability, but the degeneracy in eccentricity (single-planet system with  $e \sim 0$  or double-planet system with  $e \sim 0$  and an extremely distant companion) prevents us from drawing any conclusions about double-planet probability. For  $e > 0.1$ , there is a non-zero probability that a given RV planet has a wide-separation companion. Specifically, for  $0.1 < e < 0.4$  the average probability is  $\sim 10\%$ , for  $0.1 < e < 0.3$  the average probability is  $\sim 13\%$ , and for  $0.1 < e < 0.2$  the probability is  $\sim 19\%$ . Averaged over all eccentricities, the probability is  $\sim 4\%$ .

## CHAPTER 3

## DIRECT IMAGING CONSTRAINTS ON THE PUTATIVE EXOPLANET 14 HER C

We present results of deep direct imaging of the radial velocity (RV) planet-host star 14 Her (=GJ 614, HD 145675), obtained in the  $L'$  band with the Clio-2 camera and the MMT adaptive optics system. This star has one confirmed planet and an unconfirmed outer companion, suggested by residuals in the RV data. The orbital parameters of the unconfirmed object are not well constrained since many mass/semimajor axis configurations can fit the available data. The star has been directly imaged several times, but none of the campaigns has ruled out sub-stellar companions. With  $\sim 2.5$  hrs of integration, we rule out at  $5\sigma$  confidence  $\gtrsim 18 M_J$  companions beyond  $\sim 25$  AU, based on the Baraffe et al. (2003) COND mass-luminosity models. Combining our detection limits with fits to the RV data and analytic dynamical analysis, we constrain the orbital parameters of 14 Her c to be:  $3 \lesssim m/M_J \lesssim 42$ ,  $7 \lesssim a/\text{AU} \lesssim 25$ , and  $e \lesssim 0.5$ . A wealth of information can be obtained from RV/direct imaging overlap, especially with deep imaging as this work shows. The collaboration between RV and direct imaging will become more important in the coming years as the phase spaces probed by each technique converge. Future studies involving RV/imaging overlap should be sure to consider the effects of a potential planet's projected separation, as quoting limits assuming face-on orientation will be misleading. A version of this chapter originally appeared as a published paper in the *Astrophysical Journal* (Rodigas et al., 2011). All work described below, with the exception of the RV data-fitting performed by Jared Males, was carried out by me, with helpful suggestions by the co-authors of the published paper.

### 3.1 Introduction

In recent years, several exoplanets have been discovered by direct imaging (Marois et al., 2008; Kalas et al., 2008; Lagrange et al., 2010). While the radial velocity (RV) technique has by far discovered the most exoplanets (525 as of February 2011, <http://exoplanet.eu>), the few direct imaging discoveries have expanded our knowledge of exoplanets significantly. The directly-imaged planet orbiting Fomalhaut (Kalas et al., 2008) shows evidence for having cleared out dusty material in the star’s debris disk. The four  $\sim 10$  Jupiter-mass ( $M_J$ ) planets in the HR 8799 system (Marois et al., 2008, 2010) orbit at such a wide range of distances that they challenge all current planet formation theories. The sun-like star GJ 758 has a  $\sim 40 M_J$  companion with a  $T_{eff} < 600$  K, making it one of the coldest objects ever discovered (Thalmann et al. (2009); Currie et al. (2010)). Recently direct imaging has helped probe exoplanet atmospheres; Janson et al. (2010) characterized the atmosphere of HR 8799 c via spectra and Hinz et al. (2010) characterized the atmospheres of HR 8799 b, c, and d via photometry at 3-5  $\mu\text{m}$ . For the first time significant orbital motion has been imaged for the planet in the  $\beta$  Pic system (Lagrange et al. (2010), Lagrange et al. (2009)). This has helped constrain the planet’s orbit.

While the RV technique is mostly sensitive to planets orbiting close (semimajor axis  $a \lesssim 5$  AU) to their host stars, direct imaging probes the outer ( $a \gtrsim 5$  AU) regions. Thus direct imaging and RV complement each other. A star’s planetary system architecture can be well-characterized when it is studied by both RV and direct imaging. A planet’s true mass, semimajor axis, eccentricity, and orbital inclination can be determined when it is detected by both RV and direct imaging. Mass-luminosity models for low-mass brown dwarfs and gas-giant planets (e.g, Baraffe et al. (2003); Burrows et al. (2003)) can also be constrained and improved

in this case.

The optimal targets for direct imaging are young planets on wide orbits. Since the optimal RV targets are old, quiescent stars with close-in planets, the sample of systems that satisfy both techniques' requirements is currently very small. Even if one cannot currently image any known companions, perhaps imaging of RV stars can detect previously undiscovered companions. Rodigas & Hinz (2009) used Monte Carlo simulations of RV data to show that as many as 15% of RV systems that contain a single, moderately-eccentric planet may have an additional massive planet on a wide orbit. In this case the outer planet's RV signal is weak enough that it is not detected above the noise. A more favorable case would be if the outer planet was suggested by a long-term trend in the RV data. Then we know the companion is there, and it is just a matter of detecting it.

The star 14 Her (=GJ 614, HD 145675) is a prime target for RV/direct imaging overlap. At a distance of  $17.6 \text{ pc} \pm 0.1 \text{ pc}$  (van Leeuwen, 2007a), it is close enough that direct imaging can probe as close as  $\sim 9 \text{ AU}$  from the star. 14 Her is a multiple-body system. It has one detected planet (of minimum mass  $4.64 M_J$ , semimajor axis  $a = 2.77 \text{ AU}$  and eccentricity  $e = 0.369$ ) and a second unconfirmed companion that has been suggested by a long-term trend in the RV data (Wittenmyer et al., 2007; Goździewski et al., 2006, 2008). Two-planet Keplerian fits to the data suggest that the outer companion is  $\gtrsim 2.1 M_J$  and orbits at  $\gtrsim 7 \text{ AU}$  (Wittenmyer et al., 2007). Dynamical analysis by Goździewski et al. (2008) suggests a best-fit, minimum  $\chi^2$  mass of  $\sim 8 M_J$  and a semimajor axis of  $\sim 9 \text{ AU}$ , though there were a host of low- $\chi^2$  solutions. Fig. 3.1 shows the current RV data excluding the orbit of the primary from Wittenmyer et al. (2007). Due to the lack of data covering the orbit of the outer companion, there are many different possible mass/semimajor axis solutions.

The companion, at a minimum, orbits on a fairly wide orbit. This is beneficial for direct imaging since luminous objects on wide orbits are easier to detect via imaging than objects on small orbits. This comes from imaging typically having better contrast (and therefore sensitivity) farther from the star. Imaging, especially at the current epoch, is also favorable given that for most of the possible orbital solutions 14 Her c is likely to have a large projected separation; only for some high inclination solutions can the planet be behind or in front of the star.

Direct imaging of stars with known exoplanets has yielded strong constraints on planetary masses orbiting at large separations (e.g., Janson et al. (2009); Heinze et al. (2008); Kenworthy et al. (2009)). With regard to 14 Her, there have been several direct imaging campaigns. Two direct imaging campaigns with the Keck and Lick Observatories have already ruled out stellar-mass ( $M > 80 M_J$ ) companions beyond 9 and 12.7 AU, respectively (Luhman & Jayawardhana, 2002; Patience et al., 2002).<sup>5</sup> Carson et al. (2009) used the Palomar telescope to rule out  $\sim 70 M_J$  companions beyond  $\sim 18$  AU.<sup>5</sup> Recently Leconte et al. (2010) used the Advanced Electro-Optical System telescope to conduct an imaging survey of nearby solar-like stars, one of which was 14 Her. However with only  $\sim 20$  minutes of integration they do not report any significant detection limits for this star. Deeper imaging is required to set meaningful constraints on 14 Her c and any other potential companions.

To investigate the nature of 14 Her c and probe for additional high-mass planets and brown dwarfs, we have carried out deep direct imaging of 14 Her in the  $L'$  band with the MMT adaptive optics (AO) system. In Section 3.2 we describe the observations and data reduction. In Section 3.3 we present our constraints on 14 Her c's mass, combining analysis of the published RV data with our direct

---

<sup>5</sup>These limits assume a face-on orientation to the star, which is unlikely.



imaging results and analytic dynamical analysis. In Section 3.4 we summarize and conclude.

### 3.2 Observations and Data Reduction

Observations were carried out at the MMT on Mount Hopkins in Arizona on the night of UT 2010 May 30. We used Clio-2 (Freed et al., 2004; Sivanandam et al., 2006; Hinz et al., 2006; Currie et al., 2010), Arizona’s high-contrast near-infrared camera, and observed in the  $L'$  band. The field of view was approximately  $9''$  by  $30''$ , with a plate scale of  $29.9$  mas/pixel, determined by observations of the binary star HD 223718. We turned the instrument rotator off so that the field of view would rotate throughout the observations; this is essential for high-contrast angular differential imaging (ADI, Marois et al. (2006)). Observing conditions were optimal, with clear skies, good seeing, and the AO providing consistently good atmospheric correction. Throughout the observations, we nodded the telescope every few minutes by  $10''$  so that each image would contain the target star and sky background. We obtained 8764.7 seconds (2 hrs 26 mins) of integration on 14 Her. At  $\sim 50\%$  efficiency with Clio-2 in the  $L'$  band, this translated into  $\sim 5$  hours of wall-clock time. A small fraction of the obtained images were not used in the data reduction due to the AO being off, wind shake distorting the star, or an infrequent occurrence of losing the star on separate telescope nods. We also obtained unsaturated images of 14 Her and HD 203856 (an  $L'$  standard star from Leggett et al. (2003)) using a neutral density filter to calibrate our photometry.

Images were saved and written as stacked data cubes. All data reduction was performed with custom scripts in Matlab. We divided each image by the number of frames in each data cube and by the integration time to produce units of dn/s for each pixel. We corrected the images for bad pixels using a bad pixel mask,

and we removed detector and image artifacts as follows: since each image serves as both a target image and a background image, each image was subtracted from the opposite-nod image obtained closest in time to it, as long as that image had not already been used in the nod-subtraction process. Once an image is used to remove sky background, it is no longer available for nod-subtraction. Since we saturated the central  $0.''3$  core of the star in each image, we determined the pixel location of the star by smoothing each image with a 25 pixel ( $0.''75$ ) disk (pillbox) average, finding the maximum pixel location, then calculating the center of light at this pixel within a  $0.''75$  radius. Calculating the center of light allows for sub-pixel registration, which increases contrast. We used the center of light location to register each nod-subtracted image to a common pixel location. We then reduced the images using the LOCI algorithm (Lafrenière et al., 2007). Each image was rotated clockwise by  $2.53^\circ$  minus its parallactic angle to obtain north up and east left. The  $2.53^\circ$  rotational constant was determined by observing the binary star HD 223718. The final image was produced by median-combining the set of all the images. The change in parallactic angle between the first and last images taken during the night was  $158^\circ$ , allowing us to detect point sources all the way up to the saturated central star ( $0.''3$ ).

### 3.3 Results and Discussion

Fig. 3.2 shows our final reduced image of 14 Her. No candidate companions are identified. Some point-sources masquerade as “real,” but after dividing up the data into the first and second half of the night, all sources can be ruled out as speckles.

To determine our sensitivity level, we calculated the standard deviation per pixel in a 5 pixel ( $0.''15 = \text{FWHM}$ ) annulus centered on the star, from  $0.''3$  to  $2''$ .

We compared the total flux in a 5-pixel aperture centered on the unsaturated image of HD 203856 to the 14 Her standard deviation per pixel  $\times$  the square root of the number of pixels in the 5-pixel aperture. We used this ratio to calculate the apparent magnitude of the 14 Her background as a function of separation from the star. We used unsaturated images of 14 Her to calculate its apparent magnitude relative to the standard star HD 203856. We calculated this value to be 4.76 mag. We used this value and the 14 Her background annulus calculation to determine the contrast as a function of separation from 14 Her. Based on these calculations, we achieve excellent imaging contrast and sensitivity with our observations, reaching contrasts of  $\sim 10 \Delta$  mags at  $0.''4$  and  $\gtrsim 13 \Delta$  mags beyond  $1''$ .

### 3.3.1 Phase Space Constraints

The true mass of a directly imaged luminous object depends heavily on its age. The younger the host star, the brighter the object is expected to be. Knowing the host star's age accurately is essential for pinning down the companion mass range. Unfortunately 14 Her's age, like many stars' ages, is fairly uncertain. Kinetically the star is a metal-rich thin-disk star, suggesting an age  $< 10$  Gyr. The chromospheric activity and age-rotation-activity estimates from Mamajek & Hillenbrand (2008) estimate an age of 7.8 Gyr and  $> 8$  Gyr, respectively. Given that 14 Her is very metal rich ( $[\text{Fe}/\text{H}] \sim 0.3$ ), age-rotation-activity calibrations (as in Mamajek & Hillenbrand (2008)) could overestimate the age, since these rely on solar-metallicity calibrator stars. On the other hand, Rocha-Pinto et al. (2000) estimated an age of  $\sim 3.3$  Gyr from chromospheric activity and metallicity studies. However this value may underestimate the true age since it is based on a linear age-activity fit, which does not appear to accurately fit samples with well-determined ages (Mamajek & Hillenbrand, 2008). There are in total seven

reported age values of 14 Her. One of these is almost twice the age of the universe (Takeda et al., 2007), so we ignore this value. Because our observational result is a non-detection, we want to quote conservative upper limits to mass and should thus use a conservative age in calculations. Therefore we take the maximum of the remaining age values<sup>6</sup> and adopt this value, 8 Gyr, as the age of 14 Her. The COND age tracks do not fall on 8 Gyr, but rather between 5 and 10 Gyr. Therefore we quote  $M_J$  sensitivities interpolated between these two ages.

As a first step towards constraining 14 Her c's phase space, we fit the available RV data from Wittenmyer et al. (2007), Butler et al. (2006), and Naef et al. (2004) at fixed outer planet mass and semimajor axis, allowing all other system parameters to vary. In Fig. 3.3 we plot the  $\Delta\chi^2 = 1$  contours for inclination angles ranging from  $11^\circ$  to  $90^\circ$  (colored lines). 14 Her, like most stars with RV planets, has an unknown inclination angle. Nonetheless Han et al. (2001) found  $i > 25^\circ$  and Reffert & Quirrenbach (2011) found  $11^\circ < i < 154^\circ$ , both using Hipparcos astrometry. The latter range is equivalent to  $11^\circ < i < 90^\circ$  since we are dealing with the amplitude of  $\sin i$ . To be conservative we adopt this range of inclination angles when computing 14 Her c phase space.

A second constraint comes from analytic dynamical analysis. We used equations derived by Szebehely & McKenzie (1981) to calculate the maximum mass 14 Her c could have at a given semimajor axis such that the three-body system is stable. This is shown as the grey curve in Fig. 3.3. The equations assume that both planets have  $e = 0$  and treat 14 Her b as a massless test particle. We know that this is not true for 14 Her b; it is both fairly massive ( $> 4.64 M_J$ ) and eccentric ( $e = 0.369$ ), both of which would limit the outer planet's minimum semimajor

---

<sup>6</sup>3.33 Gyr (Rocha-Pinto et al., 2000), 5.0 Gyr (Valenti & Fischer, 2005), 5.24 Gyr (Takeda, 2007), 6.9 Gyr (Wright et al., 2004), 7.8 Gyr (Mamajek & Hillenbrand, 2008),  $> 8$  Gyr (Mamajek & Hillenbrand, 2008)

axis. This means that our results from this analysis are conservative estimates. Any phase space to the left of this dynamical curve is considered unstable.

In addition to ruling out mass and semimajor axis values, the dynamical curve also helps constrain eccentricity. We computed eccentricity contours from the RV fits, but do not plot them (for clarity). The  $e > 0.5$  solutions are ruled out since the regions of these eccentricity contours that lie within the  $\Delta\chi^2 = 1$  contours correspond to dynamically unstable massive companions. Therefore we take  $e = 0.5$  as an upper limit on 14 Her c's eccentricity.

Constraints from our direct imaging cannot simply be plotted in Fig. 3.3 because this would assume a face-on orientation. For imaging we must deal with projected separation instead of semimajor axis. Therefore the most probable orbital elements, which are within the regions to the right of the dynamical curve and within the RV contours, must be mapped into projected separation space at the epoch of the imaging observations.

In Fig. 3.4 we plot the dynamically-bound RV contours, mapped into projected separation, for  $11^\circ < i < 90^\circ$  (colored contours). At high inclinations, some orbital solutions place 14 Her c behind or in front of the star due to projection effects. The final constraint comes from our direct imaging sensitivity (solid black curve in Fig. 3.4). The planet's allowed mass and separation values must reside below the imaging curve and inside the dynamically-bound RV contours. We shade this region grey.

14 Her c then has the following constraint on mass:  $3 \lesssim m/M_J \lesssim 42$ . Using  $42 M_J$  as an upper limit on mass, we can constrain 14 Her c's semimajor axis. This is shown in Fig. 3.5, which is the same as Fig. 3.3 except that we have included this mass constraint (horizontal black line). The phase space above the horizontal line is ruled out. The allowed phase space, which is below the mass constraint line

and to the right of the dynamical curve, is shaded grey. 14 Her c’s semimajor axis is then given by  $7 \lesssim a/\text{AU} \lesssim 25$ . Our limits agree well with the dynamical results of Goździewski et al. (2008), who estimated a best-fit mass, semimajor axis, and eccentricity of  $\sim 8 M_J$ ,  $\sim 9 \text{ AU}$ , and  $\sim 0.2$ , respectively.

### 3.4 Conclusions: What is 14 Her c?

A main goal in exoplanet imaging studies is to determine how planets form. Without better constraints on mass, semimajor axis, and eccentricity we are unable to comment on whether 14 Her c formed by core accretion or disk instability. However, the close separation and low mass constraints presented here indicate the object formed out of the disk, rather than via cloud fragmentation. If 14 Her c’s semimajor axis is closer to  $\sim 7 \text{ AU}$ , its mass is likely to be small and comparable to that of 14 Her b, which would suggest formation by core accretion. It may take many more years of additional RV and imaging observations before more powerful constraints can shed light on how the two planets formed. Nonetheless this work is important for showing the potential of RV/direct imaging overlap. We have demonstrated the “proof of concept,” showing how much orbital phase space can be constrained with just a few hours of observations combined with RV data and simple dynamical analysis. We also showed the importance of considering projected separation of an RV planet when constraining phase space. Future cases of RV/imaging overlap should work in projected separation, as assuming face-on orientations can be misleading. The next generation of large ground- and space-based telescopes will be able to probe lower-mass regimes and will therefore set more powerful constraints. This deeper imaging, combined with continued RV monitoring of systems like 14 Her, will help characterize the architectures of the planetary systems beyond our own.

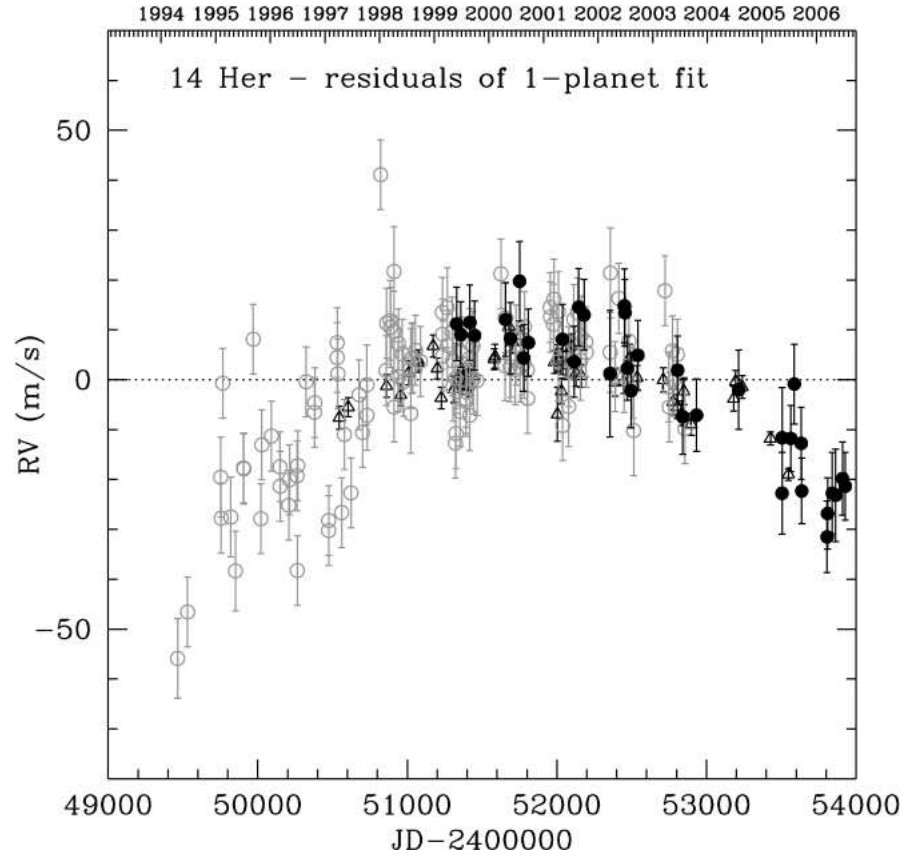


Figure 3.1 RV data excluding the primary (b) component for 14 Her, from Wittenmyer et al. (2007). Because the observation baseline is shorter than the companion's long period, there are many possible good fits to the data and therefore many possible values for 14 Her c's mass, semimajor axis, and eccentricity.

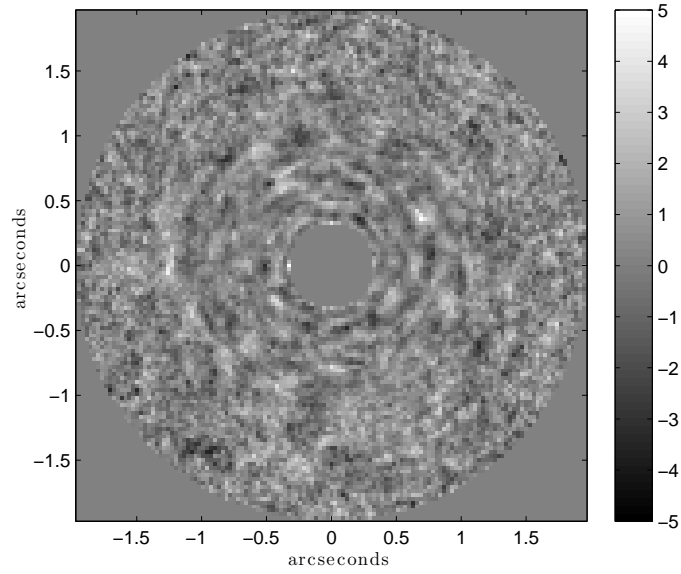


Figure 3.2 Final reduced image of 14 Her, obtained using the LOCI algorithm. North is up and east is to the left. The central  $0.''32$  has been masked out since this region is saturated. The stretch is  $-5\sigma$  to  $5\sigma$ , where  $\sigma$  was computed as the standard deviation in 5 pixel-wide ( $0.''15$ ) annuli centered on the star. No candidate companions are identified in the image.



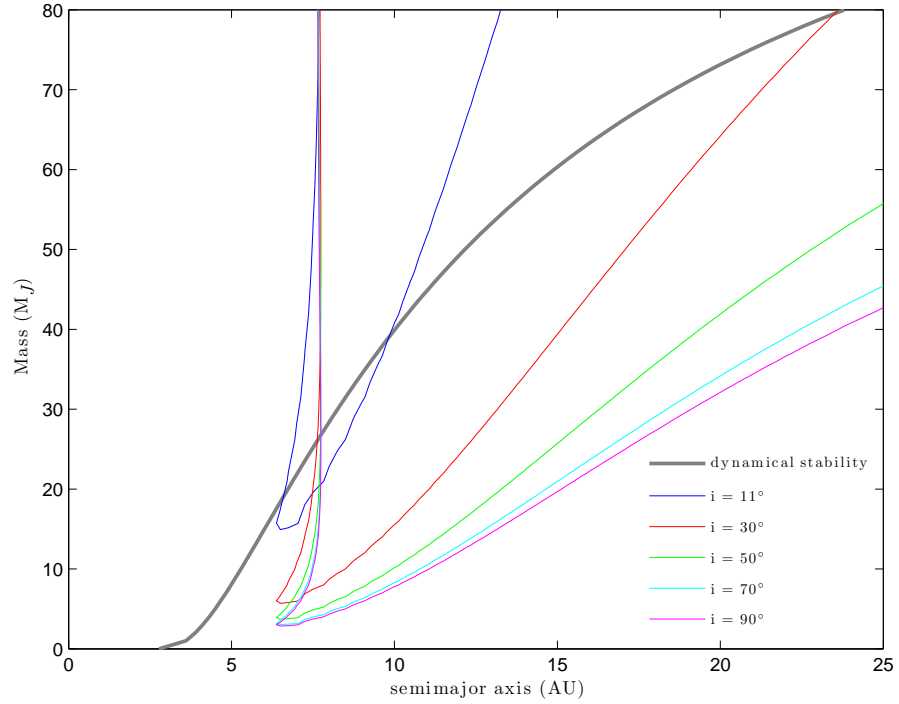


Figure 3.3 Mass vs. semimajor axis for 14 Her c, from  $\Delta\chi^2 = 1$  RV contours (colored lines,  $11^\circ < i < 90^\circ$ ) and an analytic dynamical constraint (grey line). The RV contours were computed by fitting the available RV data from Wittenmyer et al. (2007), Butler et al. (2006), and Naef et al. (2004) at fixed outer planet mass and semimajor axis, allowing all other system parameters to vary. The dynamical constraint, which comes from equations derived by Szebehely & McKenzie (1981), represents the maximum mass 14 Her c could have at a given semimajor axis such that the three-body system is stable.

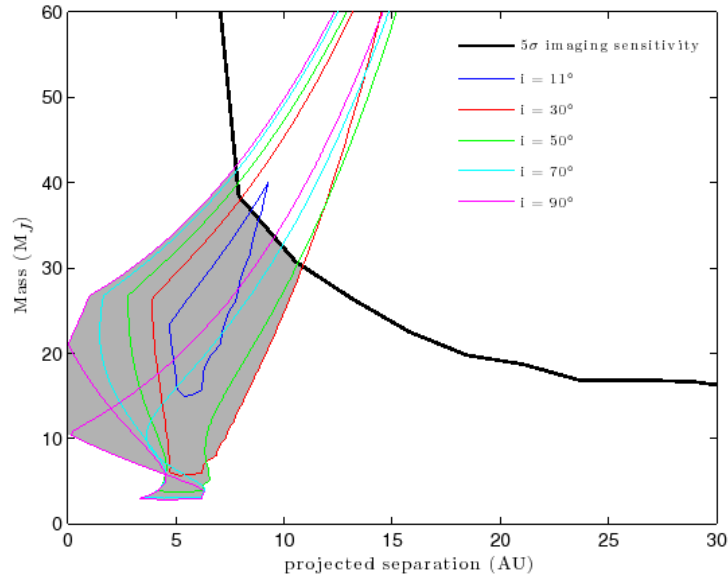


Figure 3.4 14 Her c’s mass vs. projected separation at the epoch of our imaging observations. The solid black curve is our imaging sensitivity curve. Any phase space above this line is ruled out at  $5\sigma$  confidence. The colored contours represent the projected dynamically-bound  $\Delta\chi^2 = 1$  RV contours. At high inclinations, some orbital solutions place 14 Her c behind or in front of the star due to projection effects. The region shaded grey represents the planet’s most probable mass and separation values.

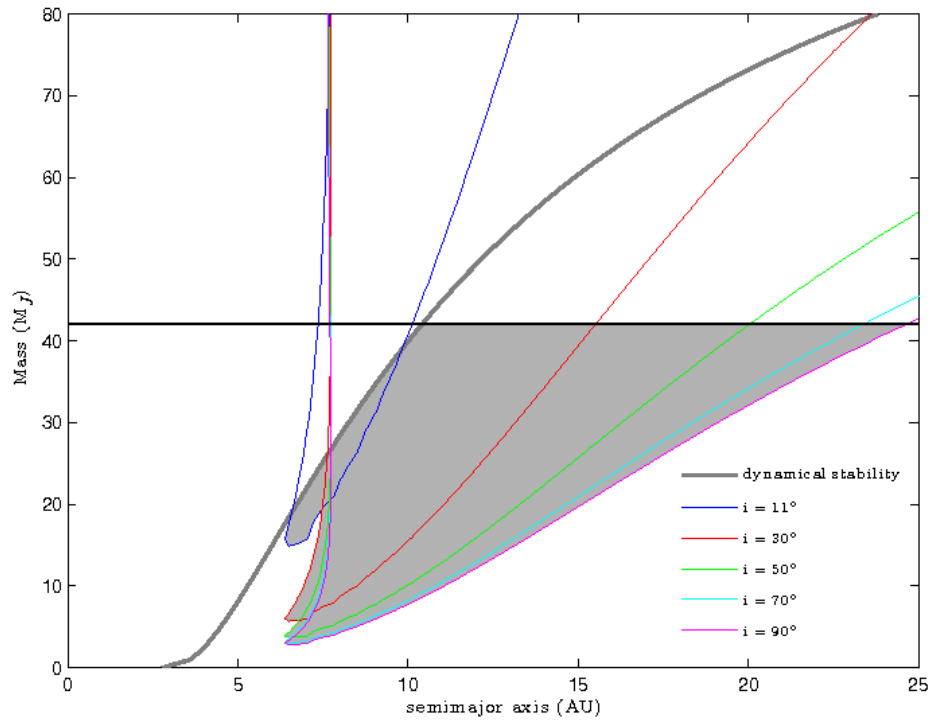


Figure 3.5 The same as Fig. 3.3, except the  $42 M_J$  upper limit on mass (horizontal black line), which was calculated from Fig. 3.4, is included. The phase space above this line is ruled out. The allowed phase space, which is below this line and to the right of the dynamical curve, is shaded grey. 14 Her c's maximum semimajor axis is then  $\sim 25$  AU.

## CHAPTER 4

THE GRAY NEEDLE: LARGE GRAINS IN THE HD 15115 DEBRIS DISK FROM  
LBT/PISCES/ $K_s$  AND LBTI/LMIRCAM/ $L'$  ADAPTIVE OPTICS IMAGING

We present diffraction-limited  $K_s$  band and  $L'$  adaptive optics images of the edge-on debris disk around the nearby F2 star HD 15115, obtained with a single 8.4 m primary mirror at the Large Binocular Telescope. At  $K_s$  band the disk is detected at signal-to-noise per resolution element (SNRE)  $\sim 3$ -8 from  $\sim 1.2''5$  (45-113 AU) on the western side, and from  $\sim 1.2''1$  (63-90 AU) on the east. At  $L'$  the disk is detected at SNRE  $\sim 2.5$  from  $\sim 1.1''45$  (45-90 AU) on both sides, implying more symmetric disk structure at  $3.8 \mu\text{m}$ . At both wavelengths the disk has a bow-like shape and is offset from the star to the north by a few AU. A surface brightness asymmetry exists between the two sides of the disk at  $K_s$  band, but not at  $L'$ . The surface brightness at  $K_s$  band declines inside  $1''$  ( $\sim 45$  AU), which may be indicative of a gap in the disk near  $1''$ . The  $K_s - L'$  disk color, after removal of the stellar color, is mostly grey for both sides of the disk. This suggests that scattered light is coming from large dust grains, with  $3$ - $10 \mu\text{m}$ -sized grains on the east side and  $1$ - $10 \mu\text{m}$  dust grains on the west. This may suggest that the west side is composed of smaller dust grains than the east side, which would support the interpretation that the disk is being dynamically affected by interactions with the local interstellar medium. A version of this chapter originally appeared as a published paper in the *Astrophysical Journal* (Rodigas et al., 2012). All work described below, with the exception of the spectral energy distribution analysis performed by Kate Su, was carried out by me, with helpful suggestions by the co-authors of the published paper.

## 4.1 Introduction

Debris disks are thought to be signposts for planet formation since their reservoirs of dust grains must be frequently replenished by collisions between larger, planetesimal-sized bodies (Wyatt, 2008). The idea of debris disks as markers for planets has been supported by the recent direct detections of wide-orbiting, massive exoplanets in systems that also harbor luminous debris disks (e.g., Marois et al. (2010); Kalas et al. (2008); Lagrange et al. (2010)). In systems with spatially resolved disks where no planets are detected, knowledge of dust grain sizes, compositions, density distributions, and disk morphologies can help us infer where any unseen planets might reside (Moro-Martín & Malhotra, 2005; Quillen, 2006).

To date the highest resolution images of debris disk scattered light have been obtained in the visible to near-infrared (NIR) with the Hubble Space Telescope (HST) and from the ground with adaptive optics (AO). Unfortunately, due to thermal emission from the Earth's atmosphere, obtaining ground-based detections of scattered light from extended debris disks at wavelengths longward of  $2\ \mu\text{m}$  is difficult. But the  $2\text{--}5\ \mu\text{m}$  wavelength region is a window into important debris disk properties. Scattered light at these wavelengths is sensitive to larger grains ( $\gtrsim$  a few  $\mu\text{m}$ ) than can be probed by visible to NIR scattered light. Imaging at these wavelengths can also constrain dust grain compositions, in particular the fraction of water ice on the surface of dust grains (Inoue et al., 2008). The  $3\text{--}4\ \mu\text{m}$  wavelength region is also particularly sensitive to the thermal radiation of massive exoplanets (e.g., Burrows et al. (2003); Hinz et al. (2010); Marois et al. (2010); Lagrange et al. (2010)). Therefore imaging at these wavelengths simultaneously probes disk scattered light from large grains and thermal radiation from exoplanets.

Because debris disks are optically thin, edge-on disks have a larger optical

depth along the line of sight than face-on disks. Therefore, in the favorable case of an edge-on inclination, disk flux densities (assuming isotropic scattering) are maximized, facilitating their detection above the high sky background. In addition, when creating a reference point spread function (PSF) from the intrinsic rotation of the sky relative to the telescope using the science target (as in Liu (2004) and Fitzgerald et al. (2007), for example), edge-on disks are more resistant to disk self-subtraction when differencing the reference PSF from the observed target. However being edge-on and bright does not guarantee detections longward of  $2\ \mu\text{m}$ , as Fitzgerald et al. (2007) obtained confident detections of the AU Mic debris disk in the  $J$ ,  $H$ , and  $K_s$  bands, but reached only a  $3\sigma$  upper limit of  $\sim 12.6\ \text{mags/arcsecond}^2$  at  $L'$  (in 12 minutes of integration). To confidently detect scattered light at  $3.8\ \mu\text{m}$  from the ground, longer integrations (relative to integrations at shorter wavelengths) are required to mitigate the higher sky background. Additionally, detections are facilitated if the disk consists of large, grey-scattering grains as opposed to small, blue-scattering grains.

HD 15115 is a nearby ( $d = 45.2 \pm 1.3\ \text{pc}$  (van Leeuwen, 2007b)) F2 star with an edge-on asymmetric debris disk previously spatially resolved in the visible and NIR (Kalas et al., 2007; Debes et al., 2008b). The star is believed to be young for several reasons: it has shared kinematics with the 12 Myr old  $\beta$  Pic moving group (Moór et al., 2006), it is believed to be on the zero-age main sequence (Eric Mamajek, private communication), and it has a high fractional luminosity circumstellar disk ( $f_d = 4.9 \times 10^{-4}$ ), which is more commonly seen for younger stars (Moór et al., 2006). However other indicators, such as Ca II H and K lines and X-ray emission, may point to a much older age, perhaps 100-500 Myr (Silverstone, 2000; Rhee et al., 2007). Furthermore Debes et al. (2008b) refuted the evidence for the star being a  $\beta$  Pic group member, based on backtracking the star's proper

motion and radial velocity. Given the large uncertainty in this star's age, for the purposes of this paper we take the star's age to be conservatively between 10 Myr and 1 Gyr.

HD 15115's circumstellar disk is believed to be gas-poor, with  $< 0.28 \times 10^{-4} M_{\oplus}$  in CO gas (Moór et al., 2011a), and has  $0.047 M_{\oplus}$  in dust mass (Zuckerman & Song, 2004; Williams & Andrews, 2006). Therefore the disk is considered to be predominantly "debris." At visible wavelengths, the disk is highly asymmetric, with the western lobe extending out to a stellocentric radius of  $\sim 12''$  in a "needle"-like feature (Kalas et al., 2007). Kalas et al. (2007) reported blue F606W -  $H$  colors, especially at large separations (hence the "blue needle"). Debes et al. (2008b) also saw blue scattering beyond  $2''$ , but reported red F110W -  $H$  colors at  $1''$ . The red color of the disk close to the star makes HD 15115 an attractive target for 2-4  $\mu\text{m}$  imaging.

Resolving the disk longward of 2  $\mu\text{m}$  would allow us to constrain the population of large grains in the disk, especially closer to the star. This requires high-Strehl ratio, low thermal background observations. From the ground, we need a precise adaptive optics (AO) system and a minimal number of warm surfaces in the optical path.

The Large Binocular Telescope (LBT) satisfies these requirements. Currently it has a single adaptive secondary mirror with 675 actuators, capable of operating with up to 500 modes of correction on one of the two 8.4 m primary mirrors. This allows for high-Strehl ratio (up to 70-80% at  $H$  band and up to 95% at  $Ks$  band), low thermal background observations (see Esposito et al. (2011) and references therein for a review of the LBT AO system).

We observed HD 15115 at  $Ks$  band and at  $L'$  with the DX (right) primary mirror and its adaptive secondary mirror at the LBT. In Section 2 we describe the ob-

servations we carried out at  $Ks$  band with PISCES (McCarthy et al., 2001) and at  $L'$  with LMIRcam (Skrutskie et al., 2010) combined with the non-interferometric mode of the Large Binocular Telescope Interferometer (LBTI, Hinz et al. (2008)), as well as our data reduction methods. In Section 4.3 we present our results on the disk structure and surface brightness (SB) profiles, and limits on planets in the system. In Section 4.4 we discuss the implications of our results, including the disk color and grain sizes. In Section 4.5 we summarize the main results.

## 4.2 Observations and Data Reduction

### 4.2.1 LBT/PISCES $Ks$ band

We carried out our  $Ks$  band observations of HD 15115 on UT November 9 2011 with the PISCES camera, a high-contrast 1-2.5  $\mu\text{m}$  imager modified for use at the LBT. PISCES has a field of view (FOV) of  $\sim 19''$  on a side and a plate scale of 19.4 mas/pixel. PISCES, which uses a pyramid wavefront sensor with natural starlight, was mounted at the right front bent Gregorian focus behind the First Light Adaptive Optics (FLAO) system (Esposito et al., 2010). Skies were clear and the seeing was good (0.5-1'') for most of the duration of the observations. We used the single 8.4 m DX (right) mirror combined with its adaptive secondary mirror. The camera rotator was fixed at a fiducial position to allow for angular differential imaging (ADI; Marois et al. (2006)), and no coronagraphs were used. We obtained 603 images with 4 s integration per image, resulting in a total integration of 40.2 minutes and  $\sim 40^\circ$  of parallactic angle rotation. For approximately the first half of the integration, the star remained stationary on the detector and was not noddled or dithered. For the second half of the data, the star was moved to the opposite side of the detector, after approximately half an hour of down time during which the AO was not functioning. We also obtained several 0.8 s unsaturated images



of HBC 388 in the narrowband BrG ( $\lambda_0 = 2.169 \mu\text{m}$ ) filter, a few hours after HD 15115, as a photometric reference.

The raw images were corrected for cross-talk and geometrical distortion<sup>1</sup>. After these steps, all data reduction was performed with custom Matlab scripts. Each half of the data was used to subtract the sky and detector artifacts from the opposite half, and flat-field corrections were applied from sky images obtained earlier in the night. Each image was divided by its exposure time to obtain units of counts/s. All images were saturated at the cores (inside  $\lambda/D$ ) of the PSF, so the star positions were determined by calculating the center of light using an annulus from just outside the saturated region to  $2''$ . We performed similar center of light calculations on the unsaturated images of HBC 388 and found the difference between the true centroid and the calculated centroid to be  $\sim 1$  pixel ( $0''.194$ ). The images were then registered to a fiducial position. For each image, we calculated the azimuthal median radial profile after masking out the spider arms and other detector artifacts, constructed an image built from the radial profile, and subtracted that from the original image.

After median-combining the first half of the images, the second half of the images, and all images together, we determined that the second half of the data was of much poorer quality than the first half, perhaps due to the worse seeing during this part of the night. Consequently we only used the first half of the data in our final data reduction and analysis. We constructed the master PSF reference by median-combining the first 284 images, and scaling and subtracting this reference image from each of the first 284 images. The scale factor was determined by minimizing the flux after subtraction inside a  $0.15\text{--}1''$  annulus (outside the saturated region). Each image was then flipped about the vertical axis (due to a

---

<sup>1</sup>see <http://aries.as.arizona.edu/> and links therein

mirror flip inside PISCES) and rotated by its parallactic angle plus an additional rotational offset to obtain North-up, East-left. The offset was determined to be  $80.88^\circ$  (the position angle of the detector) plus  $3.9^\circ$  (see Section 3.2 for a discussion of how the  $3.9^\circ$  offset was determined). The total parallactic angle rotation for this set of images was approximately  $20^\circ$ .

We median-combined the PSF-subtracted, rotated images, masking out the residual streaks left by the spider arms and other detector artifacts. The final image revealed HD 15115's edge-on asymmetric disk structure at the expected position angle (PA) of  $\sim 279^\circ$  (Kalas et al., 2007; Debes et al., 2008b)). To obtain the highest SNR image, we reduced the first 284 (better quality) images using a conservative LOCI (Lafrenière et al., 2007) algorithm, as in Buenzli et al. (2010) and Thalmann et al. (2011). Specifically, to preserve disk flux we required a field rotation of at least 3 times the full-width half-max (FWHM) at  $Ks$  band ( $= 3 \times 0''.0525$ ) between images. We also set the optimization section ( $N_A$ ) to 2000 to ensure less self-subtraction. Fig. 4.1a shows our final PISCES/ $Ks$  band image in  $\text{mJy/arcsecond}^2$ .

Because we could not obtain any unsaturated images of HD 15115 (the shortest integration time possible with PISCES is 0.8 s, which saturates the star), the flux calibration for obtaining units of  $\text{mJy/arcsecond}^2$  was calculated as follows: we scaled the ratio of the PSF halo of HBC 388 to its total flux and compared that to the halo of the median-combined PSF reference image of HD 15115 (so that the disk flux contribution was washed out). The ratio was determined for different halo sizes, ranging from  $0''.3$  to  $1''$ ,  $1''.25$ , and  $1''.5$ —all yielding the same ratio to within less than 1%. We adopted this method, as opposed to scaling by the relative bandwidths in the  $Ks$  and BrG filters, because the latter method may be less accurate due to changing photometric conditions.

Fig. 4.1b shows the map of the signal-to-noise per resolution element (SNRE) of the final  $Ks$  band image. The SNRE was determined by masking out the disk in the final image, smoothing the image by a Gaussian kernel with FWHM =  $0''.0525$  ( $= \lambda/D$ ), calculating the standard deviation of the smoothed image in concentric annuli around the star, then dividing this noise image into the final smoothed  $Ks$  band image. From the SNRE map, the disk is detected on the eastern side at SNRE  $\sim 3$  between  $1.2\text{--}2''.1$ ; and on the western side the disk is detected at SNRE  $\sim 3\text{--}8$  between  $1\text{--}2''.5$ .

We refer the reader to the Appendix, wherein we describe how we inserted an artificial model disk into the raw data and re-reduced the data using the LOCI algorithm, to understand LOCI's effects on disk position angle, FWHM, and surface brightness as a function of distance from the star. The algorithm's effects on these values were measured and accounted for in the disk analysis found later in this paper.

#### 4.2.2 LBTI/LMIRcam $L'$

We carried out our  $L'$  observations of HD 15115 on UT November 16 2011 with LMIRcam (Skrutskie et al., 2010), a high-contrast  $3\text{--}5\ \mu\text{m}$  imager designed for use with LBTI (Hinz et al., 2008). These observations were made in direct imaging mode, without any interferometric combination. Like the FLAO system, LBTI also uses a pyramid wavefront sensor with natural starlight for the adaptive reference source. We used the 8.4 m DX mirror combined with its adaptive secondary. LMIRcam has a FOV of  $\sim 11''$  on a side and a plate scale of  $10.7\ \text{mas/pixel}$ , determined from observations of the binary star HD 37013 the previous night. LBTI is fixed to the telescope and thus cannot rotate, facilitating the use of ADI throughout the observations. We obtained 2319 images, the first 5 with integrations of  $\sim 10$  seconds, and the remainder with integrations of  $\sim 2.5$  seconds. The total

integration obtained on the source was therefore  $\sim 97$  minutes. Observing conditions were good, with clear skies and  $\sim 1''$  seeing. For much of the second half of the integration, the wind picked up and caused some vibration-induced blurring of the saved images. At the end of the acquisition, we obtained several short-exposure, unsaturated images of HD 15115 and HD 40335, an  $L'$  standard star (Leggett et al., 2003), for photometric references. Throughout the long exposure images, each image was saturated inside  $\lambda/D$ . Due to a poorly-mounted dichroic, astigmatism in the PSF was visible inside the central  $\sim 0''.2$  of each image, creating a “cross” pattern on the PSF. This did not ultimately have any measurable effect on the quality of the data taken, and the instrumental astigmatism was corrected after the observing run. Throughout all observations, we nodded the star diagonally by several arcseconds, and dithered the star by  $0''.25$  in a box around the center of each nod position.

All data reduction was performed in custom Matlab scripts. Images were divided by their individual integration times to obtain units of counts/s, nod-subtracted, and corrected for bad pixels. Due to the large quantity of data, images were averaged in sets of 4. We registered the images to a fiducial pixel by calculating the center of light around the star, excluding the saturated pixels within  $\sim \lambda/D$ , in the same manner as for the  $Ks$  band images. We performed similar center of light calculations on the unsaturated images of HD 15115 and found the difference between the measured and true centroid to be  $\sim 0.2$  pixels (2 mas). We then calculated the radial profile of each image and subtracted it, also in the same manner as for the  $Ks$  band images. To test the quality of the data, we median-combined the first half of the data, the second half, and the entire set. We saw that though the quality of the PSFs was good, the second half of the data suffered from bright extended streaks appearing in the raw data, out to several arcsec-

onds. These streaks were not caused by the spider arms, and were not symmetric, so they could not be easily masked out and would overwhelm the brightness of any disk structure seen in the final image. Therefore we used only the first half of the data ( $\sim 40$  minutes of integration, with  $\sim 50^\circ$  of parallactic angle rotation).

After scaling and subtracting (in the same manner as for the  $Ks$  band images) the master PSF from each image in the first half of the data (240 averaged images; 960 total), we rotated each image by its parallactic angle plus an offset to obtain North-up, East-left. The offset was determined to be  $1.81^\circ \pm 0.0685^\circ$  by calculating the PA of the binary HD 37013, which was observed with LMIRcam the night before. The error was determined by independently calculating the offset with two different software routines and measuring the difference. The PSF-subtracted images were then median-combined. The final image, after smoothing by a Gaussian kernel with  $\text{FWHM} = \lambda/D$  and binning by a factor of 4, revealed edge-on disk structure at a similar PA to the disk in the PISCES  $Ks$  band image.

To obtain the highest-SNR image, we reduced the data using a conservative LOCI algorithm. Here we required 3 FWHMs ( $= 3 \times 0''.1$ ) of rotation between images, and the optimization section  $N_A$  was 300 ( $\sim 1''.5$ ). Fig. 4.2a shows this final image in  $\text{mJy}/\text{arcsecond}^2$ , where the conversion to  $\text{mJy}/\text{arcsecond}^2$  was determined using the unsaturated images of HD 15115. Fig. 4.2b shows the SNRE map of the final  $L'$  image, where the SNRE map was calculated in the same manner as for the  $Ks$  band image. The disk at  $L'$  is detected at  $\text{SNRE} \sim 2.5$  from  $1-1''.5$  on both sides of the disk.

We refer the reader to the Appendix, wherein we describe how we inserted an artificial model disk into the raw data and re-reduced the data using the LOCI algorithm, to understand LOCI's effects on disk position angle, FWHM, and surface brightness as a function of distance from the star. The algorithm's effects on

these values were measured and accounted for in the disk analysis found later in this paper.

#### 4.2.3 Ancillary Keck/NIRC2 $Ks$ band data

During the LBT observations, the PISCES camera lacked an accurate astrometric solution to determine the PA of true North on the detector. This is largely due to faulty fits header reporting of the detector PA, as well as the lack of observations of a standard binary for astrometric calibration. Therefore we compared our PISCES final image to  $Ks$  band data of HD 15115 obtained on the night of UT August 12 2011 with Keck/NIRC2, which has a very precise astrometric calibration and distortion solution determined from repeated observations of the galactic center (Yelda et al., 2010).

Briefly, the data were taken with the narrow camera with the  $0''.6$  diameter coronagraphic mask and consisted of coadded 10 s exposures, with a cumulative integration time of  $\sim 1280$  seconds and total field rotation of  $\sim 39^\circ$ . The data were processed using a conservative LOCI algorithm. To provide a detection of the HD 15115 disk minimally-biased by LOCI processing, we adopted relaxed LOCI parameters comparable to those used in Thalmann et al. (2011). Specifically, we set the LOCI parameter for the required rotation gap,  $\delta$ , to be 3 times the FWHM ( $3 \times 0''.052$ ) and set the optimization area,  $N_A$ , to be 3000 (see Currie et al. (2011) for additional details on the algorithm used). The disk was detected between  $\sim 1\text{--}2''$  at SNRE  $\sim 3\text{--}5$ . The final image was rotated clockwise by an additional  $0.252^\circ$  to obtain North-up, East-left. We show only the PISCES  $Ks$  band image in this paper because the disk in the PISCES image was detected at higher SNRE. The Keck/NIRC2 data will be discussed and analyzed in Currie et al. (2012, in prep.).

### 4.3 Results

#### 4.3.1 Disk FWHM

To better define the  $Ks$  band morphology of the disk, we measured the disk FWHM perpendicular to the major axis of the disk as a function of stellocentric distance. We did this as follows: first we rotated the final image by  $7^\circ$  so that the disk midplane was horizontal; next at each discrete horizontal (pixel) distance from the star we located the brightest pixel in the column of pixels perpendicular to the disk; we then placed a 7 pixel by 25 pixel ( $0''.13$  by  $0''.48$ ) box centered on the brightest pixel, and summed up the counts/pixel along each row of the box, producing a 1D array of 25 values. Next we fit a Gaussian to this array. The Gaussian fit gives the disk midplane pixel location along with the FWHM at that location. We also measured the disk FWHM as the number of pixels along each row with  $\text{SNRE} > 3$ . We took the final disk FWHM value as the average of the Gaussian-fitted value and the SNRE-width value, with the error being half the difference between the two. We also added in the constant FWHM offset ( $\sim 0''.03$ ) determined from insertion and recovery of an artificial disk in the raw data (see Appendix for details).

Fig. 4.3a and Fig. 4.3b show the east and west FWHM of the disk as a function of distance from the star, respectively. The western disk FWHM increases gradually with increasing distance from the star, though this may be an effect from the LOCI reduction (see Appendix), while no strong correlation is evident for the eastern FWHM. The median FWHM across the entire disk was found to be  $0''.21 \pm 0''.03$ . The intrinsic FWHM of the disk is computed by subtracting off in quadrature the PSF broadening at  $Ks$  band ( $= 0''.0525$ ), but this has a negligible effect on the disk FWHM, yielding the same value. Within the uncertainty, this value is consistent with both the intrinsic disk FWHM at  $1.1 \mu\text{m}$ ,  $0''.26 \pm 0''.07$ ,

where we computed this value by averaging the reported intrinsic disk FWHM of each side of the disk (Debes et al., 2008b), as well as the FWHM of the disk at  $0.6 \mu\text{m}$ , reported by Kalas et al. (2007) as  $0''.19 \pm 0''.1$ . The measured disk FWHM at  $Ks$  band being  $> 3$  times the size of the PSF FWHM ( $0''.0525$ ) suggests that we have spatially resolved the disk.

We also measured the FWHM of the disk at  $L'$ . We did this in the same manner as for the  $Ks$  band image, except the  $L'$  image was binned by a factor of 4 to increase the disk SNR per pixel, and we used 3 pixel by 11 pixel ( $\sim 0''.13$  by  $0''.47$ ) boxes. We also added in the constant FWHM offset ( $\sim 0''.11$ ) determined from insertion and recovery of an artificial disk in the raw data (see Appendix for details). Given the low SNRE ( $\sim 2$ -3) of the  $L'$  disk and the lack of spatial coverage (detected between only  $1$ - $1''.5$ ), we do not plot the FWHM as a function of distance from the star. Instead we computed the global FWHM value as the median of the measured FWHM disk values, which was found to be  $0''.26 \pm 0''.03$ . The intrinsic disk FWHM, calculated by subtracting off in quadrature the PSF broadening at  $L'$  ( $= 0''.0940$ ), is  $0''.24 \pm 0''.03$ . Within the uncertainty this value is consistent with the both the intrinsic disk FWHM at  $Ks$  band, as well as the disk FWHM at  $1.1 \mu\text{m}$  (Debes et al., 2008b) and at  $0.6 \mu\text{m}$  (Kalas et al., 2007). Given that the measured FWHM is  $\sim 2$  times the size of the PSF FWHM at  $L'$ , the disk is marginally spatially resolved.

#### 4.3.2 Disk Position Angle

To determine the rotational offset needed to obtain North-up, East-left in our final PISCES  $Ks$  band image, we compared our  $Ks$  band disk image to the Keck/NIRC2  $Ks$  band image, since the rotational offset has been well-calibrated for Keck/NIRC2. We do not compare our PISCES image to published HST images to avoid any potential wavelength-dependent changes in PA. Comparing our final PISCES



$Ks$  band image with the Keck image between 1-2'' revealed a difference in overall PA of  $3.9^\circ$ , so we rotated our PISCES image by an additional  $3.9^\circ$  clockwise. Fig. 4.1a shows this correctly-rotated image.

To test for any warps in the disk, we calculated the PA of the disk at  $Ks$  band on both sides of the disk as a function of distance from the star, using the disk midplane pixel locations from the Gaussian fits. The errors were measured as the difference between these values and the center of light along each 1D row at each discrete pixel distance from the star. The errors also included the 1 pixel =  $0''.194$  astrometric centroiding uncertainty. Fig. 4.4a and Fig. 4.4b show the  $Ks$  band PA of the eastern and western sides of the disk as a function of distance from the star, respectively. The eastern PA increases with increasing distance from the star, similar to what is seen over the same spatial locations at  $1.1\ \mu\text{m}$  (Debes et al., 2008b). The western PA increases closer to the star. This also agrees with the western PA vs. stellocentric distance seen at  $1.1\ \mu\text{m}$  (Debes et al., 2008b) and with the overall PA ( $278.5^\circ$ ) measured for the western side of the disk at  $0.6\ \mu\text{m}$  between 1.5-12'' (Kalas et al., 2007).

We calculated the PA of the disk at  $L'$  in the same manner as for the  $Ks$  band image, except we used 3 pixel by 11 pixel ( $\sim 0''.13$  by  $0''.47$ ) boxes. The  $L'$  image was again binned by a factor of 4. We do not plot PA vs. distance from the star due to the poor spatial coverage of the disk and, even after binning, the low SNRE ( $\sim 2$ -3); however the measured values for both sides of the disk were globally consistent with the values measured at  $Ks$  band (this is also evident by examination of the  $Ks$  band and  $L'$  disk images in Fig. 4.1a and Fig. 4.2a, respectively).

### 4.3.3 Surface Brightness Profiles

For both the  $Ks$  band and the  $L'$  disk images, we obtained the SB profiles by calculating the median disk flux in circular apertures with a radius of  $0''.15$  centered on the Gaussian-fitted disk midplane location at each discrete pixel distance from the star. We chose this aperture size because it maximized the SNR of the disk flux at  $L'$ . This was necessary because the  $L'$  disk is detected at low SNRE ( $\sim 2.5$ ), so using larger apertures incorporated more background noise. We measured the errors as the standard deviation of the median SB values in the same apertures placed in a circular annulus at each pixel distance from the star. We computed the aperture correction at  $Ks$  band to be 0.64 by convolving the image of the photometric reference HBC 388 with a bar of unity counts/pixel and  $\sim$  equal width to the observed disk at  $Ks$  band. The SB as a function of distance from the star is shown in Fig. 4.5a. “Magnitudes” in this paper refers to Vega magnitudes.

Between  $\sim 1.2$ – $2''.1$  (where both sides of the disk are detected), the typical western disk SB is  $\sim$  a magnitude/arcsecond<sup>2</sup> brighter than the eastern side. A similar brightness asymmetry was seen at  $1.1 \mu\text{m}$  (Debes et al., 2008b). It is also interesting that the western SB appears to drop off near  $1''$ , by  $\sim$  half a magnitude/arcsecond<sup>2</sup> (although the noise is high interior to this distance). We saw this SB reduction in our final ADI image as well as in our final LOCI image (Fig. 4.1a), even after correction with insertion and recovery of an artificial disk. The drop in SB near  $1''$  was not seen at shorter wavelengths (Kalas et al., 2007; Debes et al., 2008b), which raises suspicion that the feature may not be real. However the shorter wavelength results appear to be limited by PSF residuals interior to  $1''$ , so it may not be appropriate to compare to these data.

Table 4.1 shows the power-law indices measured for the eastern and western sides of the disk at  $Ks$  band. The power-law indices do not agree very well with

Table 4.1 *Ks* band SB power-law indices

Side	index
West ( $1-1''.2$ )	$3.48 \pm 0.5$
West ( $1''.2 < r < 1''.8$ )	$-1.75 \pm 0.05$
West ( $r > 1''.8$ )	$-4.40 \pm 0.24$
East ( $1''.2 < r < 1''.4$ )	$-5.27 \pm 0.41$
East ( $r > 1''.4$ )	$-1.1 \pm 0.07$

the indices at  $1.1 \mu\text{m}$  reported by Debes et al. (2008b). The discrepancies could be explained by the differing spatial coverage of the disk at the two wavelengths. On the other hand, it is also possible that the disk SB falls differently at *Ks* band than at  $1.1 \mu\text{m}$ . Additional high-contrast imaging data at these wavelengths would help clarify this matter. We do not calculate the power-law indices at  $L'$  due to the lower SNRE and poor spatial coverage of the disk.

Using the *Ks* band power-laws, we can quantify the significance of the SB reduction interior to  $1''.1$ . From the power-law index for  $1''.2 < r < 1''.8$ , the expected disk SB should be  $13.48 \text{ mags/arcsecond}^2$  at  $\sim 1''$ . The actual value is  $\sim 13.82$ , with a  $1\sigma$  upper limit of  $13.64$ . This suggests that we are seeing a  $\sim 2\sigma$  reduction in SB interior to  $1''.1$ .

We calculated the SB vs. distance from the star for the  $L'$  image in the same manner as for the *Ks* band image, using the same size aperture as we did for the *Ks* band image. Additionally the image was binned by a factor 4 to increase the signal-to-noise per pixel. We computed the aperture correction at  $L'$  to be  $0.63$  by convolving the photometric image of HD 15115 with a bar of unity counts/pixel and  $\sim$  equal width to the measured disk at  $L'$ . We computed the errors in the same manner as for the *Ks* band SB profile. Fig. 4.5b shows the SB profile of the

disk at  $L'$ . Both sides of the disk are  $\sim$  equal in SB beyond  $1''.2$ , which is not seen at  $Ks$  band. Interestingly, within the uncertainties the data are consistent with a flattening in SB interior to  $\sim 1''.1$ , similar to the SB drop off interior to  $1''.1$  seen in the  $Ks$  band image.

#### 4.3.4 Limits on Planets

We do not detect any high SNR point-sources in any of our data reductions that would point to a possible planet. To set firm constraints on what we could have detected, we reduced the same data that was used to detect the disk at  $L'$  with an aggressive LOCI algorithm. We examined only the  $L'$  data, as opposed to including the  $Ks$  band data as well, because we had nearly double the integration time at  $L'$  ( $\sim 40$  minutes vs. 20 minutes at  $Ks$  band) and double the parallactic angle rotation ( $\sim 40^\circ$  vs.  $\sim 20^\circ$  at  $Ks$  band). For the aggressive LOCI reduction we required only 0.75 FWHM of parallactic angle rotation between images, and our optimization section size ( $N_A$ ) was 100. Our final image (in units of  $\sigma$ , where  $\sigma$  was calculated in concentric annuli the size of the PSF FWHM ( $\sim 0''.1$ )), shown in Fig. 4.6a, reveals no  $5\sigma$  point-source detections.

To ascertain the minimum flux density point-source object we could have detected, we inserted artificial planets into the raw data and re-ran our aggressive LOCI reduction. The artificial planets were bright PSFs obtained from the unsaturated images of HD 15115. We did not scale down the PSFs in brightness. Instead we simply calculated the SNR for each artificial planet's location (inside a radius = FWHM aperture) and determined the flux that would have resulted in a  $5\sigma$  detection. These are plotted in Fig. 4.6b. We reach a  $5\sigma$  background limit of  $\sim 17.8$  mags (in 40 mins of integration). At  $0''.6$ , the contrast (computed by subtracting the star's  $L'$  magnitude of 5.763) is  $\sim 9.5$  mags. These sensitivity and contrast limits show the incredible potential of direct imaging with LBTI/LMIRcam. For

comparison, with Clio-2 at the 6.5 m MMT, a  $5\sigma$  background limit of 17.8 mags at  $L'$  was achieved in 2.5 hours of integration (Rodigas et al., 2011).

We also overplot the magnitudes of 1-3  $M_J$  planets (10 Myr old) and, conservatively, the magnitude of a 30  $M_J$  brown dwarf (1 Gyr old) from the Baraffe et al. (2003) COND mass-luminosity models (horizontal dashed lines). Assuming a young stellar age, at  $5\sigma$  confidence we rule out planets more massive than  $\sim 1$ -2  $M_J$  outside of  $1''$ , and outside of  $0''.6$  we can rule out planets more massive than  $\sim 3 M_J$ . If HD 15115's age is much older, then we can only rule out brown dwarfs more massive than  $\sim 30 M_J$  beyond  $0''.7$ .

## 4.4 Interpretations

### 4.4.1 Disk Structure

It has been suggested that HD 15115 is interacting with the local interstellar medium (ISM), given its space motion to the south-east nearly parallel with its disk major axis PA (Debes et al., 2009) and the disk asymmetries seen at shorter wavelengths (Kalas et al., 2007; Debes et al., 2008b). The  $\sim 1$  magnitude/asec<sup>2</sup> brightness asymmetry (between 1.2-2''.1) and the east-west morphological asymmetry seen in our  $Ks$  band data both support this proposition. These effects could be caused by the eastern side of the disk plowing head-first into the ISM. In this case the eastern side would be much more affected than the western side, and small grains could be blown out to the west. This could cause the eastern side to be more truncated and fainter relative to the western side, both of which we observe. Any large ( $>$  a few  $\mu\text{m}$ ) grains in bound orbits should remain mostly unaffected. Since the disk is symmetric at  $L'$ , which is sensitive to large, grey-scattering grains, our data support the ISM-interaction interpretation.

It is also certainly possible that other dynamical effects (e.g., planets or a close

passage of a nearby star as suggested by Kalas et al. (2007)) are responsible for the observed morphological and SB asymmetries. However there is currently no supporting evidence for a stellar flyby (Kalas et al., 2007; Debes et al., 2008b, 2009). Dynamical modeling of the disk with embedded planets is beyond the scope of this paper, but such modeling would help clarify what exactly is causing the observed asymmetries in the disk.

Inspection of our  $Ks$  band and  $L'$  disk images (Fig. 4.1a and 4.2a), as well as the PA vs. stellocentric distance plots for both sides of the disk (Fig. 4.4a and 4.4b) suggests that the debris disk has a bow-like shape and is offset by a few AU to the north from the star. Specifically the offsets are  $\sim 0''.012$  (0.5 AU) and  $0''.04$  (2 AU) at  $L'$ , for the eastern and western sides, respectively; and  $\sim 0''.11$  (5 AU) and  $0''.17$  (8 AU) at  $Ks$  band for the eastern and western sides, respectively. Since the astrometric uncertainty in centroiding is  $\sim 0''.002$  and  $0''.0194$  at  $L'$  and  $Ks$  band, respectively, it is unlikely that the northern offsets could be due to centroid error. Bow-like disk morphologies have been seen in systems moving in near-perpendicular directions to their disk major axis positions (e.g., HD 61005 (Hines et al., 2007) and HD 32297 (Debes et al., 2009)). Because HD 15115 is moving to the south-east, nearly parallel with its disk major axis, one would not expect the disk to have a bow-shape, especially with an offset from the star to the north. However, in the HD 61005 debris disk system, Maness et al. (2009) showed that dust grain interactions with the ISM in directions along the disk midplane could actually create bow-shapes perpendicular to the disk major axis, roughly reproducing that disk's observed morphology. Similar dynamical interactions in the HD 15115 system could be creating the observed bow-shape, though no explicit model has tested this hypothesis for this system.

Another perhaps simpler explanation for the bow-shape and the apparent off-

set is that these are caused by geometrical effects. We can reproduce the observed bow-shape and vertical offset with a simple inclined, ringed disk model. We used the radiative transfer equations describing the intensity of light scattering off dust particles and made three assumptions about the disk: it is not exactly edge-on, but rather inclined to  $87^\circ$ ; it has a gap from  $0.1''$  (see Section 4.3 for additional discussion of the possible disk gap); and we set the Henyey-Greenstein scattering parameter  $g = 0.5$  for predominantly forward-scattering grains. This is a reasonable assumption for large ( $\gtrsim 1 \mu\text{m}$ ) grains scattering NIR light (Duchêne et al., 2004). We set the dust grain size uniformly to  $3 \mu\text{m}$  and set the disk SB power-law index to  $-3/2$ . Fig. 4.7a shows the rotated model image, along with the rotated final  $Ks$  band image. Dashed lines have been inserted to guide the eye to the apparent bow-shape and northern offset from the star. Fig. 4.7b shows the PA vs. stellocentric distance for the western side of the disk in the model image, computed in the same manner as for the real data. The PA increases closer to the star, as is observed in the real data (Fig. 4.4b).

While the parameters used in our model are not a unique explanation for the observed features of the disk, the proposition that the effects can be explained by the disk’s geometric orientation in space is attractive because it explains the observations without contradicting the evidence supporting the ISM interaction interpretation (Debes et al., 2009).

#### 4.4.2 Disk Color and Grain Sizes

To determine the disk color as a function of distance from the star, we calculated  $\Delta(Ks - L') = (Ks - L')_{Disk} - (Ks - L')_{Star}$  in the regions of spatial overlap between the  $Ks$  band and  $L'$  images ( $1.1\text{--}1''45$ ). The errors were calculated by summing the individual  $Ks$  and  $L'$  errors in quadrature. The data suggest that the eastern side of the disk becomes redder than the western side with increasing distance from

the star. Interior to  $1''3$  both sides of the disk are grey.

To constrain the characteristic dust grain sizes, we compared our  $\Delta(Ks - L')$  disk colors to the models of Inoue et al. (2008). These models calculate disk colors in the NIR and assume silicate dust grain composition. The modeled grain sizes range from  $0.1 \mu\text{m}$  to  $10 \mu\text{m}$  and assume a single grain size for the dust population. We plot the model disk colors for 1, 3, and  $10 \mu\text{m}$  grains. These are shown as the colored lines in Fig. 4.8. We also modeled  $0.1 \mu\text{m}$  and  $0.3 \mu\text{m}$  grains, but their colors were too blue to be supported by the data.

From Fig. 4.8, we see that  $1\text{-}10 \mu\text{m}$ -sized grains are the best match to the western side of the disk, while  $3\text{-}10 \mu\text{m}$  are the best match to the eastern side. This suggests that the observed scattered light from the disk is tracing the large parent body dust grains in the disk. The data also may suggest that the west side of the disk is composed of smaller grains than the east side. The blowout grain size for this system is expected to be  $\sim 1\text{-}3 \mu\text{m}$  (Hahn, 2010), assuming a stellar mass of  $1.3 M_{\odot}$ , a luminosity of  $3.3 L_{\odot}$ , and a grain density in the range  $1\text{-}2.5 \text{ g/cm}^3$ . Grains smaller than the blowout size would be blown out radially; on the eastern side, these grains would hit the ISM and be blown back to the west, resulting in the western side being dominated by smaller blue-scattering grains. Our observational constraints on the dust grain sizes offer some support for these predictions.

#### 4.4.3 Does the disk have a gap?

The SB profiles at  $Ks$  band and at  $L'$  drop off or flatten out (at low SNR) near  $1''$ . For an edge-on disk with no gap, the SB should continue to increase closer to the star. Because we do not see this in our data, this may be an indication that the disk has a gap interior to  $\sim 1''1$ . This is consistent with prediction of a gap near  $1''$  by Moór et al. (2011b), using spectral energy distribution (SED) analysis of the



system. Though degenerate with temperature and dust grain size, their best-fit model of HD 15115's infrared SED yields a two-component disk, with the inner at 4 AU and the outer at 42 AU (both  $\pm 2$  AU). Given a distance to the star of 45.2 pc, the outer edge of the gap would be at  $0''.93 \pm 0''.04$ . This agrees well with the observed drop offs in SB near  $1''$ .

We can independently constrain the parent body dust grain size using estimates of the disk's equilibrium temperature as a function of distance from the star, for different grain sizes (Fig. 4.9). The equilibrium dust temperature was computed by balancing the absorption and the emission energy of a particle with adopted dust properties for astronomical silicates (Laor & Draine, 1993). Under an optically thin condition, the heating is solely from the central star, representative as the best-fit Kurucz model with a stellar temperature of 7000 K and a stellar luminosity of  $3.3 L_{\odot}$ .

The horizontal dashed lines represent the predicted disk temperatures of 179 K and 57 K from Moór et al. (2011b). Assuming we have observationally detected the inner edge of the outer disk component (and hence the gap) at  $\sim 1''.1$ , the parent body dust grain sizes are constrained to be  $\sim 3 \mu\text{m}$ . This is consistent with our dust grain size estimates from the disk colors.

#### 4.4.4 Limits on a planet inside the gap

We can also calculate an independent estimate of the mass of a planet creating the gap in the disk using the equation describing the relationship between the width of the chaotic zone around an assumed coplanar, low-eccentricity planet and its mass and semimajor axis (Malhotra, 1998):

$$\Delta a \approx 1.4 a_p (M_p/M_*)^{2/7}, \quad (4.1)$$

where  $\Delta a$  is the width of the chaotic zone,  $a_p$  and  $M_p$  are the semimajor axis and mass of the planet, respectively, and  $M_*$  is the mass of the star. We make the assumption that, from our SB profiles, the outer edge of the gap,  $r_{gap}$ , is at  $1''.1$  (50 AU). Since  $\Delta a = r_{gap} - a_p$ , we can substitute this into Eq. 4.1 and solve for the planet mass as a function of semimajor axis (Fig. 4.10).

The planet's mass approaches zero the closer it orbits to the disk edge and approaches the brown dwarf mass regime closer to the star. Assuming the gap was created by an object whose semimajor axis = its projected separation at the epoch of our observations and that the system is young, we can say that the object must be  $\lesssim$  a few  $M_J$  because we could have detected  $\gtrsim 3 M_J$  planets (dashed line in Fig. 4.10). The planet's semimajor axis would then be constrained to be between  $0.87\text{-}1''$  (40-45 AU). If the system is old, the object must be less than  $\sim 30 M_J$  and its semimajor axis would be constrained to  $0.75\text{-}1''$  (34-45 AU).

It is certainly possible that we did not detect the putative planet because it is currently in front of or behind the star. It is also possible that the gap has not been created by a planet, but instead arises from other dynamical interactions. Additional high-contrast, high angular resolution imaging of the debris disk would help constrain the existence of both the gap and any possible planets.

## 4.5 Summary

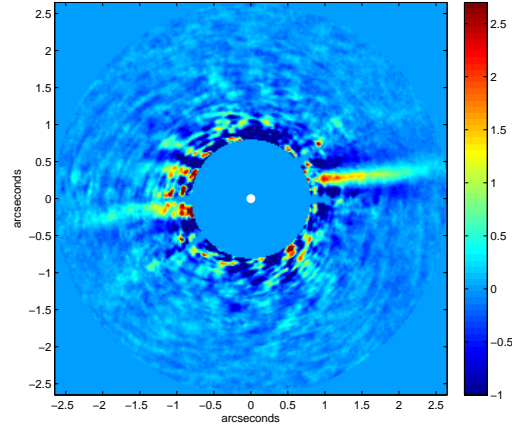
We have presented several intriguing results on the debris disk surrounding HD 15115. These results are:

1. We detect east-west asymmetry in the disk morphology at  $Ks$  band, with the western side of the disk being a  $\sim$  magnitude/arcsecond<sup>2</sup> brighter than the eastern side at the same stellocentric distances. The asymmetry and brightness differences are consistent with results at shorter wavelengths

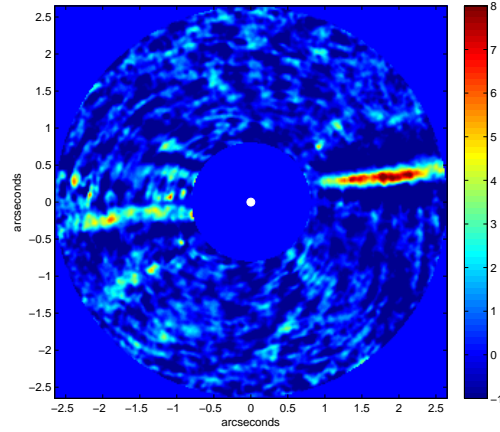
and lend additional evidence to the interpretation that ISM interactions are affecting the disk structure (Debes et al., 2009).

2. At  $L'$ , we detect symmetric and  $\sim$  equally bright disk structure.
3. We detect an overall bow-like shape to the disk at both  $Ks$  band and  $L'$ , and the disk appears offset from the star to the north by a few AU. We are able to explain these observed effects using a model disk with a near edge-on inclination, a gap between  $0.1''$ , large ( $3 \mu\text{m}$ ) grains, and mostly forward-scattering grains ( $g = 0.5$ ).
4. The FWHM of the disk at  $Ks$  band and at  $L'$  is consistent with the disk FWHM at  $1.1 \mu\text{m}$  (Debes et al., 2008b) and at  $0.6 \mu\text{m}$  (Kalas et al., 2007).
5. The disk SB profile at  $Ks$  band shows evidence for a  $2\sigma$  reduction interior to  $1''$  (50 AU). Combined with SED analysis, this may be a sign that the disk has a gap interior to  $1''$  (45 AU). Additional high-contrast observations at NIR wavelengths with better inner working angles would help confirm or disprove the proposition that the disk has a gap.
6. The  $Ks - L'$  disk color is mostly grey for both sides of the disk between  $1.1 - 1''45$  (50-66 AU).  $1-10 \mu\text{m}$  grain sizes are the best match to the western disk color.  $3-10 \mu\text{m}$  grain sizes are the best match for the eastern side. Given the system's expected grain blowout size of  $1-3 \mu\text{m}$ , our dust grain size constraints may support the ISM interaction interpretation (Debes et al., 2009), which predicts that small grains would be blown to the western side of the disk, leaving large, unaffected grains on the eastern side. SED analysis, combined with our observational evidence for a gap near  $1''$  (45 AU), also predicts a dust grain size of  $\sim 3 \mu\text{m}$ .

7. We do not detect any  $\gtrsim 5\sigma$  point-sources at  $L'$  indicative of planets. We rule out companions more massive than  $\sim 3 M_J$  beyond  $0''.6$  if the star is young and more massive than  $30 M_J$  beyond  $0''.7$  if the star is old. Independently we constrain the mass of a single, coplanar, low-eccentricity planet creating the gap in the disk to be  $\sim$  a few  $M_J$  if it is close to the disk edge, and to be in the brown dwarf regime if its orbit is closer to the star. Assuming the object's semimajor axis = its projected separation at the epoch of our observations, the planet would be  $\lesssim 3 M_J$  and orbit between  $0.87\text{--}1''$  (40–45 AU) if the star is young; if the system is old, the object would be less massive than  $\sim 30 M_J$  and orbit between  $0.75\text{--}1''$  (34–45 AU).

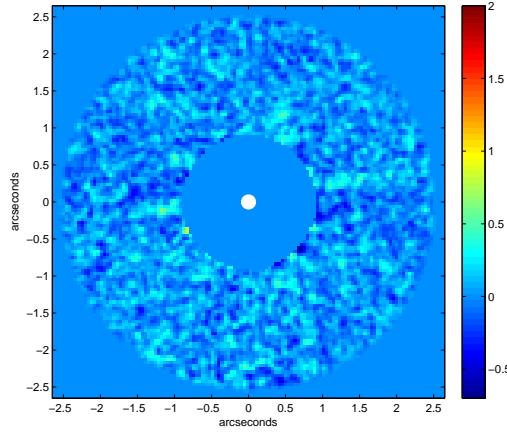


(a)

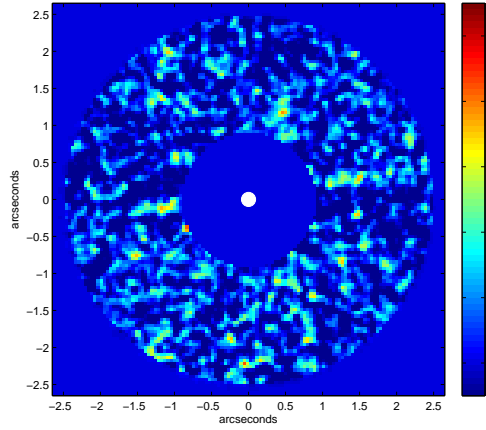


(b)

Figure 4.1 *Top*: Final PISCES  $Ks$  band image of the HD 15115 debris disk, in units of  $\text{mJy}/\text{arcsecond}^2$ , with North-up, East-left. The white dot marks the location of the star, and represents the size of a resolution element at  $Ks$  band. For display purposes a  $0''.8$  radius mask has been added in post-processing. The western side SB is  $\sim$  a magnitude/ $\text{arcsecond}^2$  brighter than the eastern side SB, as is seen at shorter wavelengths (Kalas et al., 2007; Debes et al., 2008b). *Bottom*: SNRE map of the image. The eastern side is detected at SNRE  $\sim 3$  out to  $\sim 2''.1$ . The western side of the disk is detected at SNRE  $\sim 3-8$  from  $\sim 1-2''.5$ .

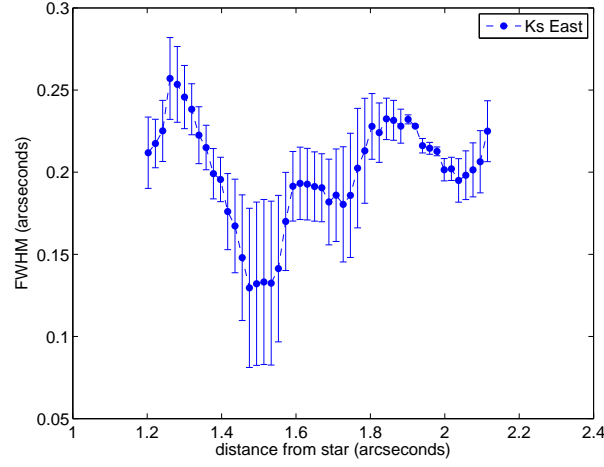


(a)

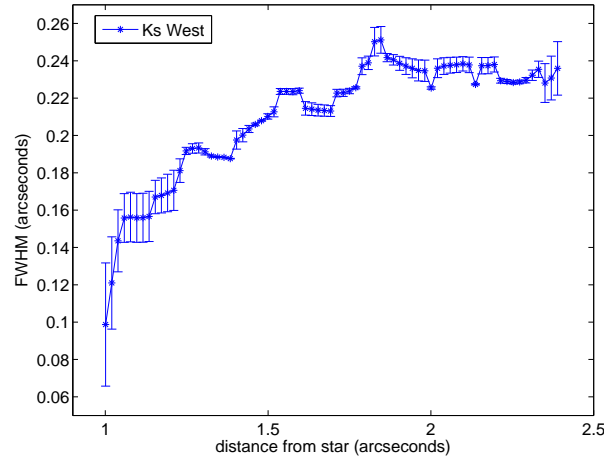


(b)

Figure 4.2 *Top*: Final  $L'$  image of the disk obtained with LMIRcam, in units of  $\text{mJy}/\text{arcsecond}^2$ , with North-up, East-left. The white dot marks the location of the star, and represents the size of a resolution element at  $L'$ . For display purposes a  $0''.9$  radius mask has been added in post-processing. The image has been smoothed by a Gaussian kernel with  $\text{FWHM} = \lambda/D$  and binned by a factor of 4 to bring out the disk. At  $L'$  the disk is mostly symmetric and is equally bright on both sides. These features are nearly opposite to what is seen at  $Ks$  band and at shorter wavelengths. *Bottom*: SNRE map of the final  $L'$  image shown above. The disk is detected at  $\text{SNRE} \sim 2.5$  between  $\sim 1-1''.5$  on both sides.

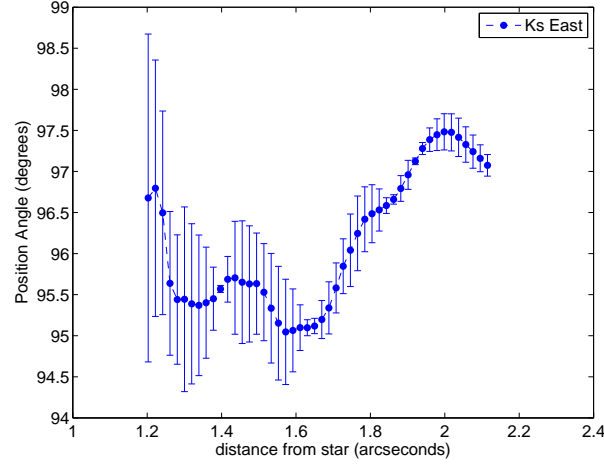


(a)

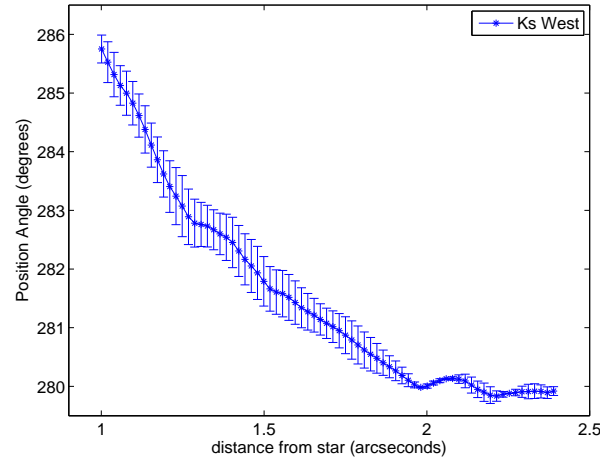


(b)

Figure 4.3 *Top*:  $Ks$  band eastern disk FWHM as a function of distance from the star. See text for methodology. There is no obvious trend in FWHM vs. stellocentric distance. *Bottom*: Same as above, except for the western side of the disk. The FWHM increases with increasing distance from the star, though this may be an effect from the data reduction (see Appendix).



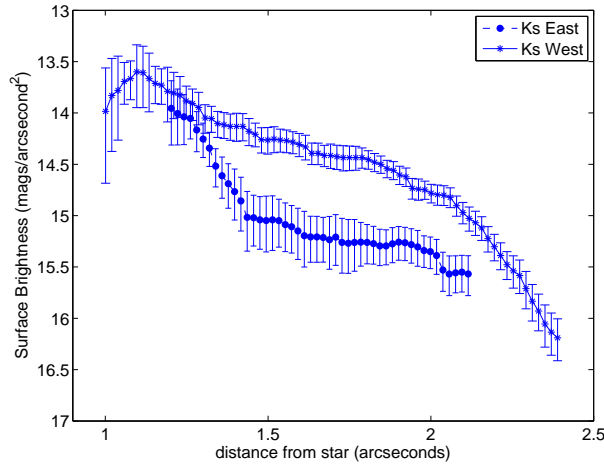
(a)



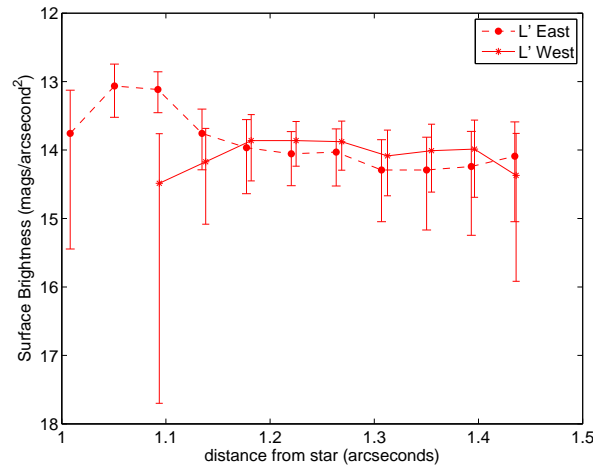
(b)

Figure 4.4 *Top*: PA of the eastern side of the disk at  $Ks$  band as a function of distance from the star. See text for methodology. The PA increases with increasing distance from the star; over the same stellocentric distances a similar trend was observed at  $1.1\ \mu\text{m}$  (Debes et al., 2008b). *Bottom*: Same as above, except for the western side. The PA increases closer to the star, as is seen in the Debes et al. (2008b)  $1.1\ \mu\text{m}$  band data.





(a)



(b)

Figure 4.5 *Top*: SB profile of the disk at  $Ks$  band. The western side of the disk is  $\sim$  a magnitude/arcsecond<sup>2</sup> brighter than the eastern side at  $Ks$  band over the same stellocentric distances. The western SB profile shows a  $\sim 2\sigma$  drop off in SB near  $1.1''$ . This cannot simply be explained by flux loss due to disk self-subtraction, since this has been corrected for. *Bottom*: SB profile of the disk at  $L'$ . Both sides of the disk are  $\sim$  equally bright beyond  $1''$ , and just as in the  $Ks$  band image there is low SNR evidence for a decrease/flattening in SB near  $1.1''$ .

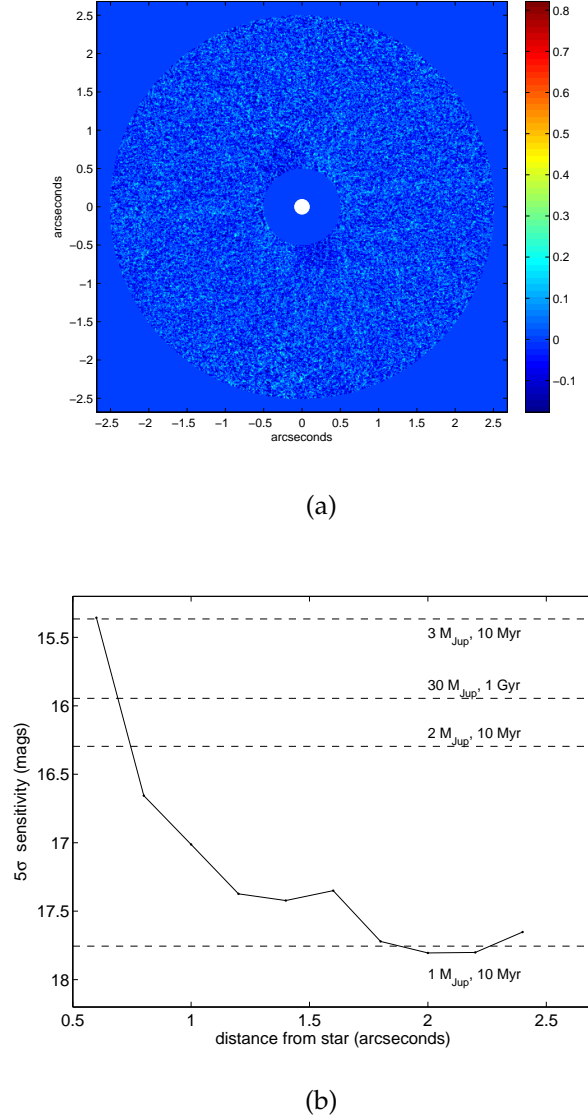
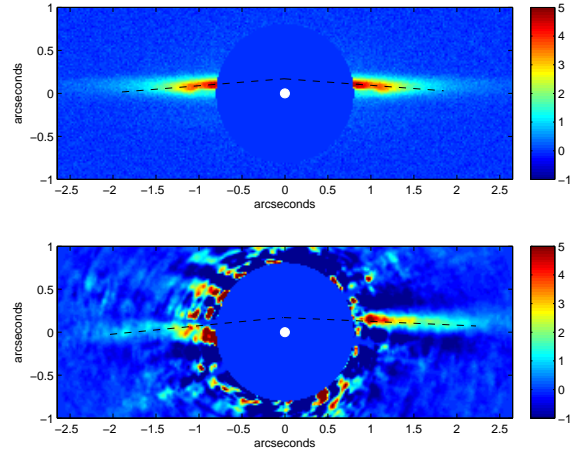
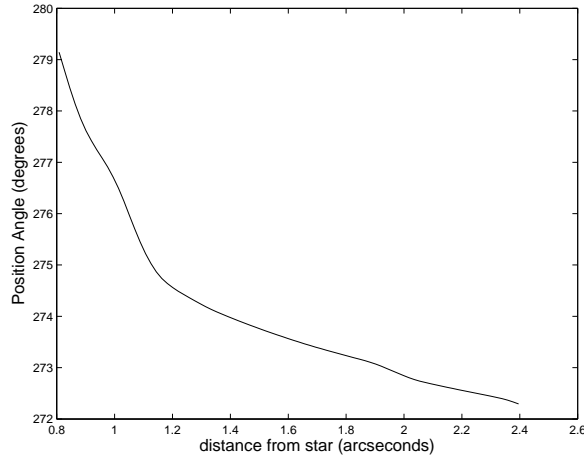


Figure 4.6 *Top*: Final image at  $L'$ , in units of  $\sigma$ , computed with an aggressive LOCI reduction. See text for methodology. The white dot marks the location of the star and the size of a resolution element at  $L'$ . No high SNR point-sources are detected. *Bottom*:  $5\sigma$  sensitivity curve for our  $L'$  data, computed by inserting artificial planets into the raw data and running our aggressive LOCI reduction. We reach a background limit of  $\sim 17.8$  mags, and a contrast of  $\sim 9.5$  mags at  $\sim 0''.6$ . The horizontal dashed lines represent the magnitudes of 10 Myr old and 10 Gyr old planets, from the Baraffe et al. (2003) COND mass-luminosity models. We rule out planets more massive than  $\sim 3 M_J$  if the star is young and  $30 M_J$  if the star is old.



(a)



(b)

Figure 4.7 *Top*: Rotated model and real  $Ks$  band disk images. The model image has an inclination of  $87^\circ$ , scattering parameter  $g = 0.5$ ,  $3 \mu\text{m}$  grains, a SB power-law index of  $-3/2$ , and a gap from  $0-1''.1$ . The model image has been convolved with the PSF from the photometric image of HBC 388, and Gaussian noise has been added. Units are in  $\text{mJy}/\text{arcsecond}^2$  for both images. The white dot marks the location of the star in both images. The dashed lines are meant to guide the eye to the apparent northern offset of the disk relative to the star. *Bottom*: PA vs. stellocentric distance for the western side of the disk in the model image. The PA increases closer to the star due to the apparent bow-shape, similar to what is seen for the real data shown in Fig. 4.4b.

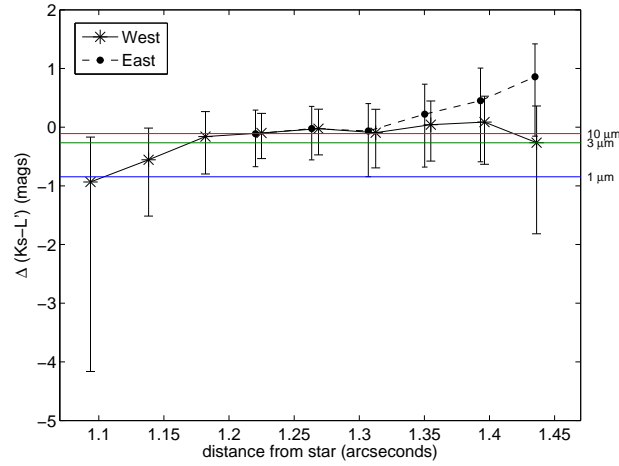


Figure 4.8 Disk color vs. distance from the star, expressed as  $\Delta(K_s - L') = (K_s - L')_{Disk} - (K_s - L')_{Star}$ . This is calculated only where the disk is detected at both  $K_s$  band and at  $L'$ . To constrain dust grain size, we also plot model colors from Inoue et al. (2008) (colored horizontal lines). The data suggest that the eastern side of the disk becomes redder than the western side with increasing distance from the star. 1-10  $\mu\text{m}$  grains are the best fit to the western side, while 3-10  $\mu\text{m}$  grains are the best match to eastern side. This may suggest that the west side of the disk is composed of smaller grains than the east side.

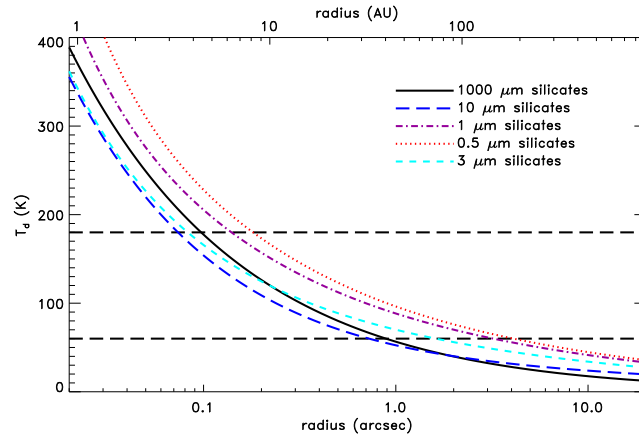


Figure 4.9 Equilibrium disk temperature vs. distance from the star, for several different silicate grain sizes. See text for methodology. The horizontal dashed lines represent temperature constraints of 179 K and 57 K from Moór et al. (2011b). Given that we have observational evidence for the predicted gap at  $\sim 1''$ , we can independently constrain the dust grain sizes to be  $\sim 3 \mu\text{m}$  for astronomical silicates.

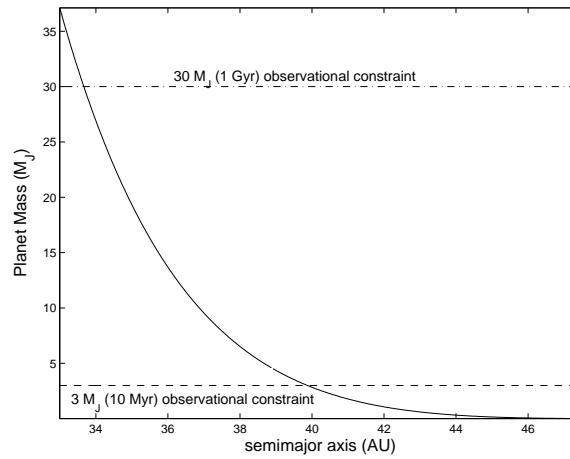


Figure 4.10 Masses of a possible object orbiting inside a disk gap with its outer edge at  $1''.1$  (50 AU), as a function of semimajor axis, computed using Eq. 4.1 (solid line). The dashed line represents our  $3 M_J$  (10 Myr old age) observational constraint and assumes that the planet's semimajor axis = its projected separation at the epoch of our observations. The dash-dot line is the same, except showing our  $30 M_J$  (1 Gyr old age) observational constraint. If HD 15115 is old, then the object creating the gap must reside between  $\sim 34$ -45 AU. If the system is young, the allowed semimajor axis range shrinks to 40-45 AU.

## CHAPTER 5

LBTI/LMIRCAM HIGH-CONTRAST  $3.8\ \mu\text{m}$  IMAGING OF THE HD 32297

## DEBRIS DISK

We present a new imaging detection of the HD 32297 debris disk at  $L'$ . The disk is detected at high S/N from  $\sim 0''.3$ – $1''$ . We do not detect any point sources that could be planets or high-mass companions but find that we could have detected planets more massive than  $\sim 8\ M_J$  beyond  $0''.5$ . The disk at  $L'$  is bowed, as is seen at shorter wavelengths, but not to the same extent. Compared to images at  $1$ – $2\ \mu\text{m}$  from HST/NICMOS, the disk is  $\sim 0.5$ – $1$  magnitude/arcsecond<sup>2</sup> brighter at  $L'$ . This red color is not easily explained, and the cometary material model suggested by D13 does not reproduce the spectrum of the disk. Small grains composed of tholins and silicates better reproduce the red color of the disk but fail to adequately match the disk's spectrum at  $1$ – $2\ \mu\text{m}$ . None of the models reproduce the observed bowing of the disk, implying the scattering asymmetry parameter is still not well-constrained. Additional modeling and narrowband data between  $3$ – $4\ \mu\text{m}$  is necessary to constrain the composition of the dust in the disk. All work described below, with the exception of the dust grain modeling performed by John Debes and the age determination of the star by Eric Mamajek, was carried out by me, with helpful suggestions from Phil Hinz and other collaborators.

## 5.1 Introduction

Debris disks, which are thought to be continually replenished by collisions between large planetesimals (Wyatt, 2008), can point to interesting planets in several ways: with high signal-to-noise (S/N) evidence of warps and/or gaps (Lagrange et al., 2010), sharp edges (Schneider et al., 2009; Chiang et al., 2009), and

with their specific dust grain compositions. Since many outer solar system bodies contain copious amounts of water ice and organic materials, finding other debris disk systems that contain water ice and/or organic materials (Debes et al., 2008a) would point to planetary systems that might contain the ingredients necessary for Earth-like life. Therefore constraining the dust grain compositions in debris disks is crucial.

Recently far-infrared Herschel observations have been used to constrain the composition of dust in two debris disks (Lebreton et al., 2012; Donaldson et al., 2013). Narrowband scattered light imaging is a particularly powerful for constraining composition because it can substitute for spectra that would otherwise be too difficult to obtain. The wavelength range between 1-5  $\mu\text{m}$ , in particular, contains strong absorption features for water ice and organics like tholins (both near 3.1  $\mu\text{m}$ ; Inoue et al. (2008); Buratti et al. (2008)).

Obtaining high S/N detections of faint debris disks at these wavelengths from the ground is challenging due to the bright thermal background of Earth's atmosphere as well as the warm, glowing surfaces in the optical path of the telescope. Adaptive optics (AO)—in particular, a system that suppresses unwanted thermal noise—is necessary to overcome these obstacles. The Large Binocular Telescope (LBT), combined with the Large Binocular Telescope Interferometer (LBTI, Hinz et al. (2008)), is one such system. The LBT AO system (LBTAO, Esposito et al. (2011)) consists of two secondary mirrors (one for each primary) that can each operate with up to 400 modes of correction, resulting in very high Strehl ratios ( $\sim 70\text{-}80\%$  at  $H$  band,  $\sim 90\%$  at  $Ks$  band, and  $> 90\%$  at longer wavelengths). This results in very high-contrast, high-sensitivity imaging capabilities, allowing detections of planets and debris disks that were previously out of reach.

Recently we used LBTI and LMIRcam (Skrutskie et al., 2010), the 1-5  $\mu\text{m}$  high-



contrast camera for LBTI, to obtain 2.15 and 3.8  $\mu\text{m}$  images of the faint debris disk around the nearby F star HD 15115 (Rodigas et al., 2012). The Ks- $L'$  colors allowed us to infer that the disk consists of a population of large stable dust grains 1-10  $\mu\text{m}$  in size. Building on this work, we have now obtained high-contrast images of the bright debris disk around the young A star HD 32297 at 3.8  $\mu\text{m}$ . Using these new images, along with archival HST/NICMOS images of the disk at 1-2  $\mu\text{m}$  from Debes et al. (2009), we attempt to constrain the typical grain size and fractional composition (silicates, water ice, tholins, and other cometary material) of dust grains in the disk.

In Section 5.2 we describe the observations and data reduction. In Section 5.3 we present our results on the disk's surface brightness at  $L'$  and our detection limits on planets in the system. In Section 5.4 we constrain the debris disk dust composition using disk models of varying dust compositions. In Section 5.5 we summarize and conclude.

## 5.2 Observations and Data Reduction

### 5.2.1 Observations

We observed HD 32297 on the night of UT November 4 2012 at the LBT on Mt. Graham in Arizona. We used LBTI/LMIRcam and observed at  $L'$  (3.8  $\mu\text{m}$ ). LMIRcam has a field of view (FOV) of  $\sim 11''$  on a side and a plate scale of 10.7 mas/pixel. Skies were clear during the observations, and the seeing was  $\sim 1''3$  throughout. The camera rotator was fixed at its nominal position (it cannot rotate) to allow for angular differential imaging (ADI; Marois et al. (2006)), and no coronagraphs were used. We used the single SX (left) primary mirror with its deformable mirror operating at 400 modes for the AO correction. To increase nodding efficiency, we chopped an internal mirror (rather than nodding

the entire telescope) by several arcseconds every few minutes to obtain images of the sky background. While this method did dramatically increase efficiency (to  $\sim 85\%$ ), neglecting to move the telescope resulted in a “patchy” background that remained even after sky subtraction. Ultimately we removed this background noise by unsharp-masking all images, which results in self-subtraction of the debris disk; this is not a problem because we accounted for this effect with the insertion of artificial disks, which we discuss in Section 5.3.1.

We obtained 759 images of HD 32297 in CDS mode, so that each image cube consisted of 15 coadded minimum exposure (0.029 s) images containing the unsaturated star (for photometric comparison), and 15 coadded 0.99 s science exposure images with the core of the star saturated out to  $0''.2$ . After filtering out images taken while the AO loop was open, the final dataset consisted of 726 images, resulting in 2.99 hours of continuous integration (not including the minimum exposure photometric images). Throughout the observations, which began just after the star’s transit, the FOV rotated by  $50.84^\circ$ , enabling the star itself to act as the PSF reference for subtraction during data reduction.

### 5.2.2 Data reduction

All data reduction discussed below was performed with custom Matlab scripts. We first divided each science exposure image by the number of coadds (15) and integration time (0.99 s) to obtain units of counts/s for each pixel. Next we subtracted opposite chop beam images of the star to remove detector artifacts and the sky background, resulting in flat images with  $\sim 0$  background counts/s, except for the “patchy” regions of higher sky noise. We determined the sub-pixel location of the star in each sky-subtracted image by calculating the center of light inside a  $0''.5$  aperture centered on the approximate location of the star. We then registered each image so that the star’s location was at the exact center of each

image. We binned each image by a factor of 2 to ease the computational load required in processing 726 images. To remove the patchy sky background regions, for each image we subtracted a 15 pixel ( $0''.32$ ) by 15 pixel box median-smoothed image from itself. The unsaturated minimum exposure images were reduced as detailed above, except for this last step of unsharp masking, since the majority of the star's flux does not overlap with the background patches.

During the observing run, the LMIRcam detector suffered from “S-shaped” non-linearity (which has since been corrected). This had the effect of artificially inflating raw counts per pixel at long exposures relative to short exposures, complicating photometric comparisons. Using a linearity curve constructed from images taken throughout the observing run, we multiplied each reduced image's pixels by the corresponding linearity correction factors. We verified the effectiveness of the linearity correction by comparing the total flux within an annulus centered on the star between  $0''.1$ - $0''.2$  for the unsaturated (linear) final image and the final (linearity-corrected) long exposure image; the median counts/s for the two images agreed to within  $\sim 4\%$ .

As a first check on the efficacy of the steps described above, we performed simple PSF subtraction by constructing a master PSF image from a median combination of all the images, subtracting this PSF from each image, and then rotating the images by the parallactic angle at the time of the exposure. The resulting image revealed edge-on disk structure at the expected position angle (PA) of  $\sim 47^\circ$  (Debes et al., 2009; Mawet et al., 2009).

To obtain the highest possible S/N detection of HD 32297's debris disk, we reduced the images using principal component analysis (PCA, Soummer et al. (2012)). PCA has recently been shown to produce equal-to or higher S/N detections of planets and disks (Thalmann et al., 2013; Bonnefoy et al., 2013; Boccaletti

et al., 2013; Soummer et al., 2012) than LOCI (Lafrenière et al., 2007), though this may be a result of LOCI’s tunable parameters not being optimized correctly (C. Marois, private communication). We did also reduce the data using conventional LOCI algorithms (Rodigas et al., 2012; Currie et al., 2012c; Thalmann et al., 2011) but found that the gain in computational speed for PCA with no loss in S/N warranted the ultimate preference of PCA over LOCI for this dataset.

We followed the prescription outlined in Soummer et al. (2012), with the main tunable parameter being  $K$ , the number of modes to use for a given reduction. Increasing  $K$  reduces the noise in the final image but also suppresses the flux from the disk; therefore this parameter must be optimized. After examining the average S/N per resolution element (SNRE) over the disk’s spatial extent for varying values of  $K$ , we determined the optimal number of modes to be  $K = 5$ . We then fed all the images through our PCA pipeline, rotated the images by their corresponding PAs clockwise to obtain North-up East-left, and median-combined the set of all images. Fig. 5.1a shows this final image, and Fig. 5.1b shows the corresponding SNRE map. We detect the disk from  $\sim 0''.2$ - $1''$  at SNRE  $\sim 3$ -9. The detection of the disk at high S/N allows us to more precisely measure its surface brightness, which in turn results in better constraints on the composition and size of the dust grains producing the observed scattered light.

### 5.3 Results

#### 5.3.1 Surface Brightness Profiles

Measuring the surface brightness (SB) of the disk as a function of wavelength requires several steps to ensure the same quantities are being compared. For the  $L'$  data, we first needed to account for the self-subtraction and other biases induced by the PCA algorithm. Therefore, as in Rodigas et al. (2012) and Currie

et al. (2012c), we measured these biases by inserting artificial disks into the raw data, re-reducing the data, and computing the correction factors based on how the SB of the artificial disks changed. We inserted three artificial disks (the best-matching model from Currie et al. (2012c)) of varying brightness and PA into the raw images. Specifically, the first disk was slightly brighter than the real disk and located  $\sim 90^\circ$  away; the second was 10% fainter than the first and located  $\sim 45^\circ$  away; and the third was 25% fainter than the first and located  $\sim 135^\circ$  away. We chose to insert disks of varying SB and PA to better account for the biases inherent in the PCA reduction.

To compute the SB of the real disk, we rotated the final image so that the disk's axis was horizontal, calculated the median counts/s in a 5 pixel (106 mas) by 5 pixel box centered on the brightest pixel at each horizontal distance from  $0''.45$ - $1''.1$  from the star, and divided this number by the plate scale of LMIRcam squared. We converted these values to mJy by measuring the total flux in the unsaturated photometric image of HD 32297.

After recovering both the real and artificial disks, we measured the PCA correction factors for the real disk's surface brightness as a function of separation from the star as follows: we calculated the median counts/s in the same 5 pixel (106 mas) by 5 pixel boxes at the same locations used for measuring the SB of the real disk, except now on the rotated, horizontal, PCA-processed artificial disks, and compared these values to the equivalent measurements on the pure, unaltered, noiseless model disk images. We recorded the ratio of these two numbers as a function of distance from the star and PA, then we averaged all the values together at each separation. The correction factors typically ranged from  $\sim 2$ -4 and were correspondingly multiplied into the SB of the real disk.

The final correction necessary for the  $L'$  SB was an aperture correction at each

distance from the star. These corrections were computed as follows: we produced model images (again with parameters determined from Currie et al. (2012c)) of the unconvolved and convolved disk at each wavelength. We measured the SB in all the HST/NICMOS images using 3 pixel ( $0''.0754$ ) by 3 pixel boxes. For the F110W ( $1.1 \mu\text{m}$ ) images, these boxes were centered on the brightest pixel at each specific pixel distance from the star ( $0''.45$ - $1''.1$ ). For the F160W ( $1.6 \mu\text{m}$ ) and the F205W ( $2.05 \mu\text{m}$ ) images, the boxes were centered on the same pixel locations as were used in the F110 image. We computed the SB in each box for the unconvolved images, first verifying that these values were constant across wavelength. Next we computed the SB values in the convolved images and determined the appropriate aperture correction factor needed to obtain the same SB in the unconvolved and convolved images. For the HST/NICMOS images, these values varied with distance from the star but generally ranged from 1-1.5.

The aperture correction for the  $L'$  data was computed in a similar manner, except that 5 pixel ( $106 \text{ mas}$ ) by 5 pixel boxes were used. We used a smaller aperture for the  $L'$  data than for the HST/NICMOS data due to the disk being thinner ( $\text{FWHM} \sim 0''.1 \approx \lambda/D$ ) at  $L'$ . To account for the different aperture sizes used for the HST/NICMOS and  $L'$  data, we included an additional aperture correction for the  $L'$  data.

For the HST/NICMOS data, which was obtained using “classical” (non-ADI) PSF subtraction, errors and uncertainties were calculated by measuring the equivalent SB values perpendicular to the disk. With this conservative estimate of errors, large error bars are associated with poor PSF subtraction, while small error bars are associated with a low level of residual flux away from the disk. For the  $L'$  data, PCA/ADI introduce residuals that typically increase closer to the star and are more azimuthally symmetric. Therefore we calculated the errors by tak-

ing the standard deviation of the equivalent SB measurements all around the star (excluding the disk itself).

Fig. 5.3 shows the SB of the 1-2  $\mu\text{m}$  HST/NICMOS data as well as the 3.8  $\mu\text{m}$  LBT data. For both the northeast and southwest sides, the disk is brighter at  $L'$  than at shorter wavelengths by  $\sim$  a magnitude/arcsecond<sup>2</sup>. The disk SB at  $L'$  falls with increasing distance from the star comparably to shorter wavelengths. Interestingly, a SB peak is seen at  $\sim 0''.9$  on the northeast side of the disk at  $L'$ . While such a feature could be a PSF subtraction residual lying on top of the signal from the disk, the feature is  $\sim$  half a magnitude/arcsecond<sup>2</sup> brighter than the disk and is detected at  $\sim 3\sigma$  confidence. If the feature corresponds to a planet embedded in the disk, the planet's mass would be  $\sim 1 M_J$ , assuming the star is 100 Myr old and using the atmospheric models of Baraffe et al. (2003). Whether this feature is a real astronomical source or not requires additional data.

### 5.3.2 Position Angle Measurements

Currie et al. (2012c) measured the PA of the HD 32297 debris disk as a function of separation from the star at  $Ks$  band and found that the disk was bowed close to the star. This was also seen at  $Ks$  band for the HD 15115 debris disk (Rodigas et al., 2012), and both effects can be explained by highly forward-scattering grains and a nearly edge-on viewing geometry. To test whether the bow shape is seen at other wavelengths, we measured the PA as a function of distance from the star at  $L'$ , and we recalculated these quantities for the 1-2  $\mu\text{m}$  HST/NICMOS data. All PAs were measured in manners analogous to those described in Rodigas et al. (2012) and Currie et al. (2012c).

Fig. 5.4 shows the PA plots for the northeast and southwest sides of the disk at 1-2  $\mu\text{m}$  and at  $L'$ . The bow shape is generally evident at each of these wavelengths and on both sides of the disk, although the change in PA is less dramatic

at  $L'$  compared to the shorter wavelengths. Additionally the PA generally decreases as a function of increasing wavelength. This may be an indication that the scattering properties of the dust change with wavelength. The forward scattering asymmetry parameter,  $g$ , may change with wavelength, which has been seen in other disks (e.g., Duchêne et al. (2004)) and may account for the change in the disk's apparent bow-shape with wavelength. See 5.4 for further discussion.

### 5.3.3 Limits on Planets

In addition to being sensitive to scattered light from debris disks at  $L'$ , imaging at this wavelength is also particularly sensitive to luminous planets, which are expected to become redder (from 1-5  $\mu\text{m}$ ) as they age and cool (Burrows et al., 2003; Baraffe et al., 2003). This is crucial for constraining planetary system architectures and consequently planet formation. Currently there are two theories that describe how planets form: core accretion (Ida & Lin, 2004; Helled & Schubert, 2008) and gravitational instability (Boss, 1997). In the former case, giant planets form by collisions of rocky planetesimals, which can then accrete gas once the core attains a mass of  $\sim 10 M_{\oplus}$  (Earth-masses). Because circumstellar gas dissipates within the first  $\sim 10$  Myr, these cores must form quickly and therefore must reside within  $\sim 30$  AU of the star. Gravitational instability circumvents this problem with planets forming out of local overdensities in the primordial circumstellar disk, and likewise predicts that planets can form and orbit much farther from their host stars.

Marley et al. (2007) modeled the evolution of the luminosities of core accretion planets (“cold-start”) and found that they are significantly dimmer at young ages ( $\lesssim 100 \text{ Myr}$ ) than planets that formed by gravitational instability (“hot-start”; e.g., Burrows et al. (2003); Baraffe et al. (2003)). An intermediate “warm-start” case has also recently been proposed (Spiegel & Burrows, 2012). Since the luminosi-



ties of planets from these models vary so much at young ages, directly imaging young planets can help determine which model—and consequently, which formation scenario—best fits the data.

The luminosities of the planets directly imaged so far seem to agree better with the “hot-start” evolutionary models (e.g., Bonnefoy et al. (2013)). This indicates that either these planets are forming differently than planets found closer to their host stars, or that the evolutionary models for “cold-start” planets need to be revised. The matter of “hot-start” vs. “cold-start” is nowhere near resolved, nor are architectures of planetary systems fully characterized. This warrants searching for luminous planets in debris disk systems like HD 32297 to help constrain planet formation and atmospheric evolution models.

By inspection of the SNRE map in Fig. 5.1b, only one source stands at  $5\sigma$  above the noise (the typical minimum threshold for detecting imaged exoplanets). However this feature, located  $\sim 1''$  away from the star at a position angle of  $\sim 80^\circ$ , is not point-like, is not very symmetrical, and is surrounded by additional residuals. Therefore we do not treat this as a real astronomical source. Other than this feature, there are no high S/N point-source features in the final  $L'$  image.

To ascertain what planets we could have detected, we assume that any planets in the HD 32297 system must currently reside within the debris disk itself and therefore insert artificial planets into the midplane of the disk. The insertion of sources into the disk is valid because the disk is likely to be optically thin, so the signals from any real embedded planets should travel to Earth relatively unimpeded. We vary the brightnesses of the artificial planets and re-reduce the data until each is recovered at  $\geq 5\sigma$  confidence. Artificial planets are made by extracting the central  $0''.094$  (=FWHM at  $L'$ ) of the unsaturated photometric image of HD 32297. The reduction pipeline for the planets uses the same parameters as were

used to detect the disk at high S/N; we investigated using more modes for PCA but found little advantage over  $K = 5$ , which was optimal for the disk.

When calculating the S/Ns of the recovered planets, we have to be careful about how we interpret the numbers since signals from the planets lie *on top* of the signal from the disk. Therefore any measurement of a recovered planet's S/N must first subtract out the S/N of the recovered disk.

After doing this, only planets at  $\geq 1''.25$  were detected at  $5\sigma$  confidence at a contrast level of  $2.5 \times 10^{-5}$  (11.5 mags). At  $5 \times 10^{-5}$ , all planets with separations  $\geq 0''.75$  were successfully detected, and at  $5.9 \times 10^{-5}$  all planets at  $\geq 0''.5$  were detected. Within  $0''.5$ , only planets 100 times fainter than the star could be detected at  $> 5\sigma$  confidence, and even these become highly elongated due to the increased self-subtraction so close to the star. This self-subtraction could in principle be removed by reducing the data more carefully (e.g., including a minimum azimuthal field rotation before subtracting a PSF image), but such an exhaustive optimization of PCA is unnecessary since it would probably not increase contrast levels here by more than a factor of 10. While the disk SB itself is very bright close to the star (especially on the northeast side), it is difficult to ascertain whether this increase in brightness is due to a planet or the disk. If the source is a planet, the brightness close to the star will change in the coming years as the planet moves in front of or behind the star, motivating additional high-contrast observations. Fig. 5.5 shows three example images, along with their S/N maps, of artificial planets inserted into the disk. Fig. 5.6 summarizes all the planet detection results.

Estimating the masses of exoplanets detected via direct imaging requires atmospheric models, which depend heavily on the age of the planet and therefore on the host star. The age of HD 32297, like many stars, is poorly constrained. The star's spectral type, which can be used to constrain its age, has ranged from

A0 (Torres et al., 2006) to A5 (Heckmann, 1975). Based on an archival optical spectrum of the star taken 2 February 2006 with the 300 line grating of the FAST spectrograph on the Tillinghast telescope (see FAST archive: <http://tdc-www.harvard.edu/cgi-bin/arc/fsearch>), and comparison of the spectrum to a dense grid of MK standard stars using the python tool “sptool”<sup>1</sup>, we estimate that the star’s spectral type is approximately A6 V (see Fig. 5.7). This leads to an effective temperature of  $T_{eff} \sim 8000$  K. Plotting the star’s updated position on an HR diagram (Fig. 5.8), along with isochrones from the evolutionary tracks of Bressan et al. (2012), we estimate that HD 32297 is most likely older than  $\sim 15$  Myr and younger than  $\sim 0.5$  Gyr. Because the star’s kinematics and the debris disk’s high fractional luminosity both point to a young age for the star ( $\sim 10$ -20 Myr), we conservatively adopt an age of 100 Myr for the star.

From Fig. 5.8, we estimate the star’s maximum age to be  $\sim$  a few hundred Myr. This justifies plotting the brightnesses of 100 Myr old planets from the atmospheric models of Baraffe et al. (2003). Comparing our limits to these planets, we rule out planets more massive than  $8 M_J$  at projected separations  $\geq 0''.5$  (56 AU), and planets more massive than  $\sim 6 M_J$  beyond  $1''.25$  (140 AU).

#### 5.4 Modeling the debris disk’s dust

The high S/N images of HD 32297 debris disk at multiple wavelengths provide a unique window into the dust grain properties within the disk. Under the assumption that a single population of grains can explain all the observations, we set out to test the recent models of the HD 32297 disk from Donaldson et al. (2013) (hereafter D13), which are constrained by observations of the disk at  $Ks$  band (Boccaletti et al., 2012) along with detailed SED modeling. The primary struc-

---

<sup>1</sup><http://rumtph.org/pecaut/sptool/>

ture of the debris disk is that of at least one component with a sharp edge at 110 AU and a drop-off in surface density with increasing radius. Additional interior, warmer dust rings are preferred to fit an additional hot component of dust (D13, Currie et al. (2012c)), but are unobservable at the current inner working angles. Any model must simultaneously reproduce the SB distributions (Fig. 5.3 and increases in PA of the disk at close separations as a function of wavelength (Fig. 5.4).

#### 5.4.1 Scattered Light Models of Optically Thin Disks

We construct a model of the disk in a similar fashion to Currie et al. (2012c) (and references therein). An analytical density distribution of dust is generated in a 3 dimensional array and sampled in a Monte Carlo fashion with 2 million particles representing a model dust population. Scattering angles are calculated for the density distribution with a given PA and inclination. Inputs to the model include a cross-sectional averaged asymmetry parameter  $\langle g \rangle$ , which can be used to model the forward scattering nature of a grain model in a self-consistent fashion assuming a specific grain size distribution (Augereau & Beust, 2006; Wolf & Voshchinnikov, 2004):

$$\langle g \rangle = \frac{\int_{a_{\min}}^{a_{\max}} n(a) C_{\text{sca}}(a) g(a) da}{\int_{a_{\min}}^{a_{\max}} n(a) C_{\text{sca}}(a) da}, \quad (5.1)$$

where  $n$  is the density of the dust in the disk and  $C_{\text{sca}}$  is the scattering cross-section. The variable  $\langle g \rangle$  can create an approximate phase function as a function of scattering angle  $\Phi(\theta)$  for the dust under the assumption of a Henyey-Greenstein functional form:

$$\Phi(\theta) = \frac{1}{4\pi} \frac{(1 - \langle g \rangle^2)}{(1 + g^2 - 2 \cos \theta)^{1.5}}. \quad (5.2)$$

The code can include linear combinations of  $\langle g \rangle$  parameters, which might be appropriate for debris disks and can reproduce the phase function that has been found for the zodiacal dust in the solar system (Currie et al., 2012c; Hong, 1985). To convert an observed disk SB into a mass, one must solve for the combination of both the phase function of the dust and the size-averaged cross section of the dust  $\langle C_{\text{sca}} \rangle$ :

$$\langle C_{\text{sca}} \rangle = \int_{a_{\text{min}}}^{a_{\text{max}}} n(a) C_{\text{sca}}(a) da. \quad (5.3)$$

We calculated scattering cross-sections  $\langle C_{\text{sca}} \rangle$  and  $\langle g \rangle$  using the real and imaginary parts of the complex indices of refraction for the best-fitting grain model (provided kindly by J. Donaldson, private communication) from the code *mies*, which has been designed specifically for fast modeling of debris disks with a size distribution of dust (Wolf & Voshchinnikov, 2004; Ertel et al., 2011). The grain model used here (and by D13) is a highly porous mixture of carbon, ice, and silicates which may also be appropriate for other debris disks (e.g., Lebreton et al. (2012)). Models were generated for each image (wavelength) with the appropriate pixel scale and sampled in a similar fashion to our SB profiles. A scaling factor for each lobe of the disk was calculated by ratioing the models with the observed disk SB profiles as a function of wavelength. The results of the models were compared with the measured SB profiles and PA vs. distance curves. For a density distribution, we used the best-fitting distribution in Boccaletti et al. (2012):

$$n(r) = n_o \sqrt{2} \left( \left( \frac{r}{110 \text{AU}} \right)^{10} + \left( \frac{r}{110 \text{AU}} \right)^{-4} \right)^{-1/2}. \quad (5.4)$$

We also kept their assumption of  $\langle g \rangle = 0.5$ , which is somewhat degenerate with the choice of an interior steep power law drop-off in density interior to 110

AU. It is also not consistent with Mie calculations of the expected  $\langle g \rangle$ , which is closer to 0.99.

#### 5.4.2 Comparison to the D13 model

Figures 5.9 to 5.10 show a comparison between the D13 model and the observations for the F110W, F160W, F205W HST/NICMOS data and our new  $L'$  data. The inferred mass from the scattered light data, assuming a minimum grain size of  $1 \mu\text{m}$  and a maximum grain size of  $1 \text{ mm}$  with a size distribution power law of  $-3.33$ , is consistent with that derived from D13.

The model fits the HST/NICMOS data well but does not reproduce the color of the disk at  $L'$ . Furthermore, this model does not reproduce the behavior of the disk midplane PA as a function of distance from the star at any of the imaged wavelengths. The lower forward asymmetry parameter assumed by Boccaletti et al. (2012) implies very little interior warping due to the diminution of the back side of the inner dust ring's SB—the front and back portions of the disk emission keep the midplane at the nominal position angle of the disk on the sky. Highly forward scattering grains, on the other hand, present only the part of the disk closest to the observer, creating an apparent inner warp due to geometrical projection of an inclined ring (Rodigas et al., 2012).

#### 5.4.3 Comparison to Water Ice, Tholins, and Silicates

An apparent problem in modeling the HD 32297 disk is balancing the apparent forward scattering nature of the grains at small scattering angles with the lack of significant brightening in the surface brightness profile due to this forward scattering at small inner working angles (Currie et al., 2012c). This is demonstrated by comparing the observations to other types of grains. We tested three additional grain compositions—pure water ice grains, pure tholin grains (Khare et al.,

1984; Debes et al., 2008a), and pure astronomical silicates. Each of these compositions has blow out sizes of  $\approx 2 \mu\text{m}$ , similar to the minimum grain size inferred by SED modeling (Donaldson et al., 2013). For these models we use Mie formalism to infer the scattering cross-sections and  $\langle g \rangle$  parameters for a Dohany size distribution of dust with varying minimum grain sizes from 1-9  $\mu\text{m}$  and a maximum grain size of 1 cm. These models are not intended to directly fit the full set of observations of the HD 32297 disk, but rather to demonstrate possible alternatives to the D13 model.

None of the models of pure water ice were able to match the spectral character of the dust, while small grain sizes of both pure tholins and pure silicates are better fits to the red color of the dust at  $L'$ . Fig. 5.11 and Fig. 5.12 show the model spectra and PA vs. distance from the star for the pure tholins model. For this model, a small grain size is also preferred (1  $\mu\text{m}$ ), but a self-consistent calculation of  $\langle g \rangle$  fails to reproduce the proper SB profiles, implying a differing density distribution than assumed above.

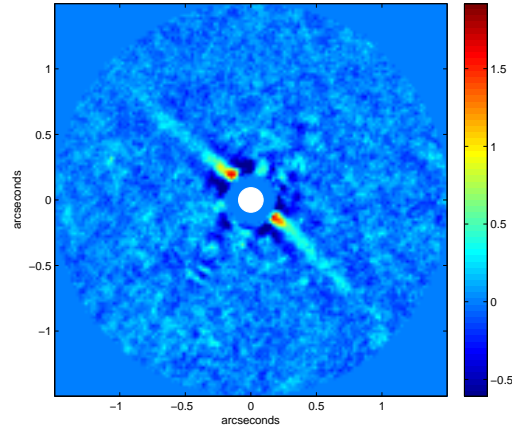
Pure self-consistent Mie calculations of grain properties fail to reproduce the observed SB distribution of the disk as a function of wavelength, nor do ad hoc models of porous grains with arbitrary values for  $\langle g \rangle$ . This results primarily from failing to simultaneously explain the interior morphology of the disk, the scattering cross-sections, and the SB profiles as a function of wavelength. Future work is required to empirically disentangle the magnitude of  $\langle C_{\text{sca}} \rangle$  and the proper phase function. This will be crucial for self-consistently modeling debris disks and comparing them to realistic grain models over a broader range of parameters.

## 5.5 Summary

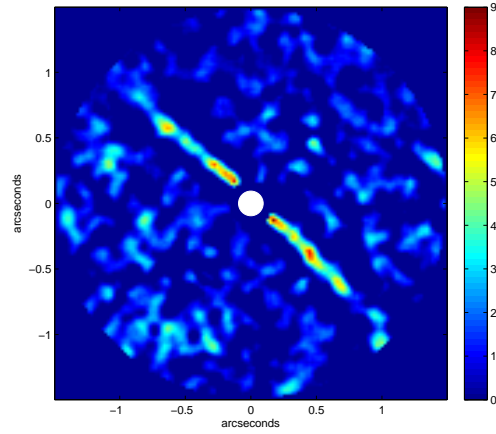
We have presented a new imaging detection of the HD 32297 debris disk at  $L'$ . The disk is detected at high S/N from  $\sim 0''.3$ - $1''$ . We do not detect any point sources that could be planets or high-mass companions. We inject artificial planets into the disk itself and find that we could have detected planets more massive than  $\sim 8 M_J$  beyond  $0''.5$ .

The disk at  $L'$  is bowed, as is seen at shorter wavelengths, but not to the same extent. Compared to images at  $1\text{-}2\ \mu\text{m}$  from HST/NICMOS, the disk is  $\sim 0.5$ - $1$  magnitude/arcsecond<sup>2</sup> brighter at  $L'$ . The disk's red color is not easily explained, and the cometary material model suggested by D13 does not reproduce the spectrum of the disk. Small grains composed of tholins and silicates better reproduce the red color of the disk but fail to match the disk's spectrum at  $1\text{-}2\ \mu\text{m}$ . None of the models reproduce the PA vs. separation of the real disk at any of the wavelengths, suggesting that the asymmetry parameter  $g$  needs to be additionally constrained.





(a)



(b)

Figure 5.1 *Top*: Final reduced  $L'$  image of the HD 32297 debris disk, in units of detector counts/s, with North-up, East-left. The white dot marks the location of the star and represents the size of a resolution element at  $L'$ . A  $0''.2$  radius mask has been added in post-processing to cover the saturated portion of the star. The SW side of the disk is brighter than the NW side, as is seen at other wavelengths. However there is no brightness asymmetry at the location of the mm peak first identified by Maness et al. (2008) and later seen at  $K_s$  band by Currie et al. (2012c). *Bottom*: SNRE map of the final image. Both sides of the disk are detected from  $\sim 0''.2$ - $1''$  at SNRE  $\sim 3$ -9.

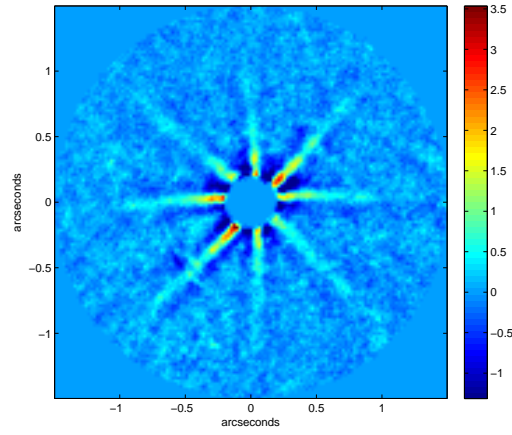


Figure 5.2 Final reduced  $L'$  image of the HD 32297 debris disk along with three artificial disks, all in units of detector counts/s, with North-up, East-left. A  $0''.2$  radius mask has been added in post-processing to cover the saturated portion of the star. The real disk is located at its nominal PA of  $\sim 47^\circ$ . All three model disks are easily recovered by the PCA pipeline, allowing correction factors for the real disk's surface brightness to be calculated.

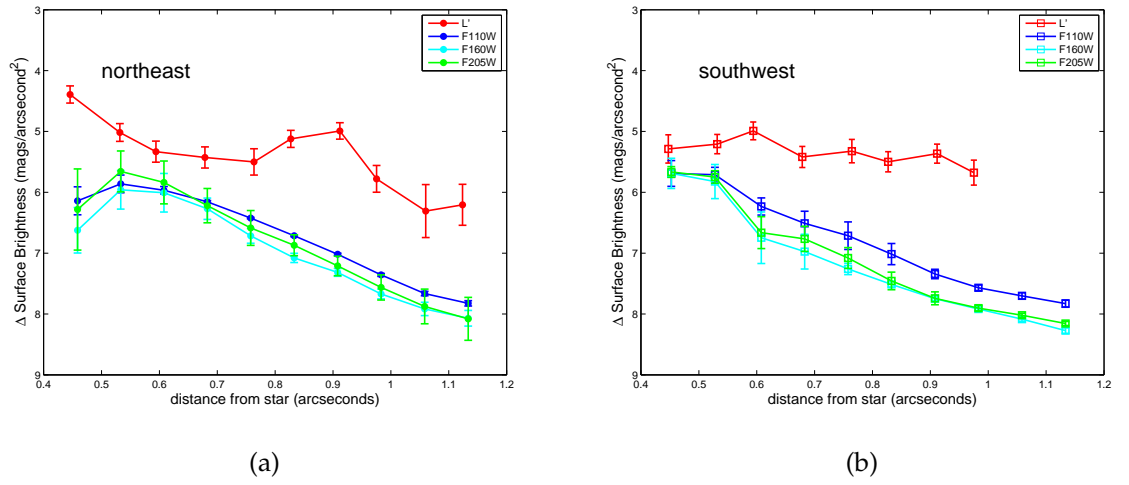


Figure 5.3 *Left*: SB profiles for the HD 32297 debris disk for the HST/NICMOS and LBT data for the northeastern lobe. *Right*: The same except for the southwestern lobe of the disk. From  $\sim 0''.4$ - $1''$ , the disk is brighter at  $L'$  than at shorter wavelengths by  $\sim$  a magnitude/arcsecond<sup>2</sup>. The profiles fall with distance from the star at similar slopes across wavelength. A  $\sim 3\sigma$  SB peak exists at  $\sim 0''.9$  on the northeastern lobe of the disk for the  $L'$  data.

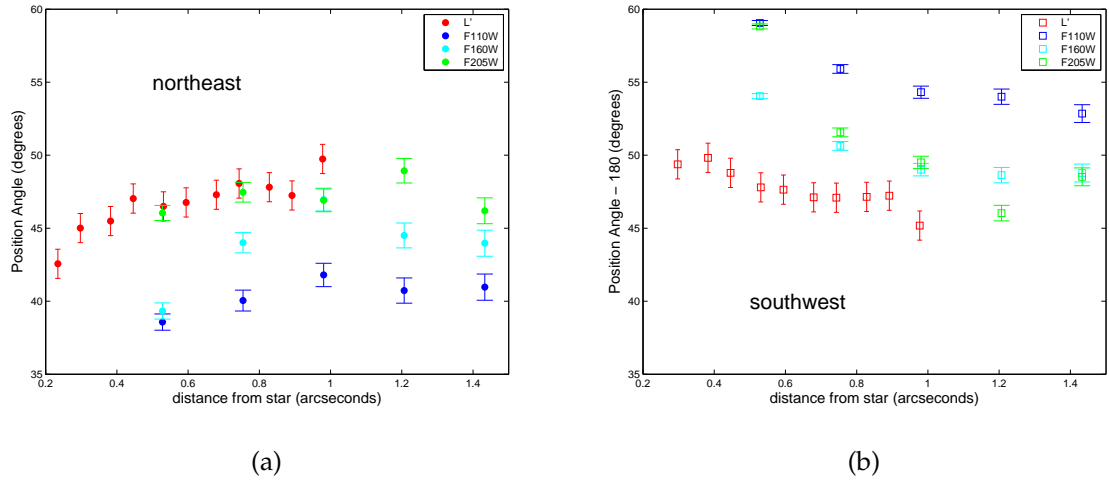


Figure 5.4 *Left*: PA as a function of distance from the star for the HST/NICMOS and LBT data for the northeastern lobe. *Right*: The same except for the southwestern lobe of the disk. The change in PA is less dramatic at  $L'$  compared to shorter wavelengths, and the PA generally decreases with increasing wavelength.

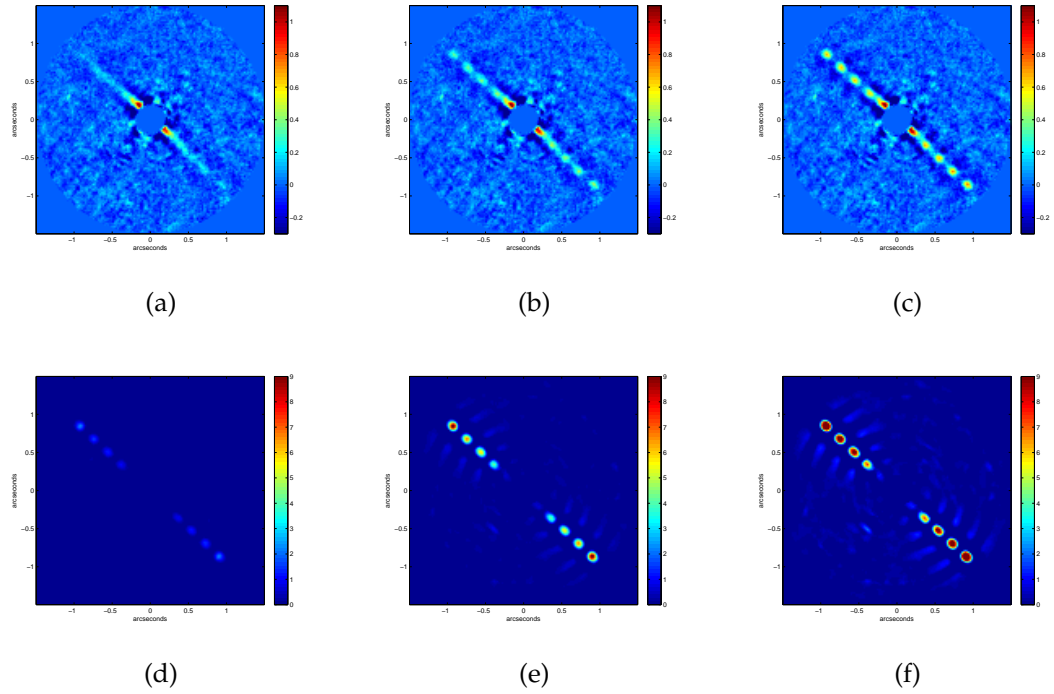


Figure 5.5 Artificial planets of varying brightnesses inserted into the HD 32297 debris disk and recovered. The top row consists of the re-reduced images with the planets inserted, and the bottom row is the corresponding S/N of the detections (after subtracting the S/N of the disk itself). From left to right, the brightnesses of the planets increases, with the leftmost panel showing no  $5\sigma$  detections and the rightmost showing successful detections for all planets at  $\geq 5\sigma$ .

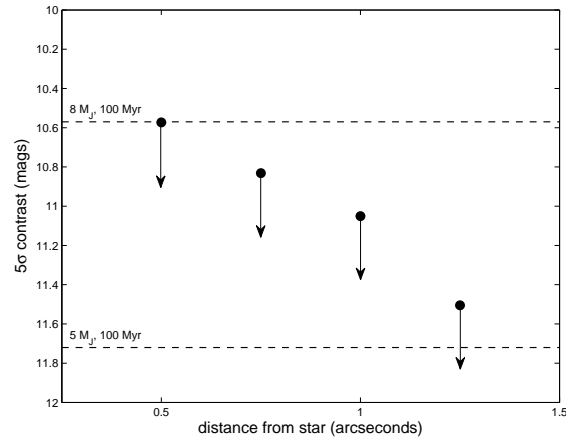


Figure 5.6 Limits on the masses of planets that could have been detected at  $5\sigma$  confidence in our  $L'$  dataset. The points with arrows represent the artificial planets that could have been detected in HD 32297's debris disk. The dashed lines correspond to the contrast (in mags) 100 Myr old planets would have in this system from Baraffe et al. (2003). We rule out planets more massive than  $8 M_J$  at projected separations  $\geq 0''.5$ , and planets more massive than  $\sim 6 M_J$  beyond  $1''.25$ .

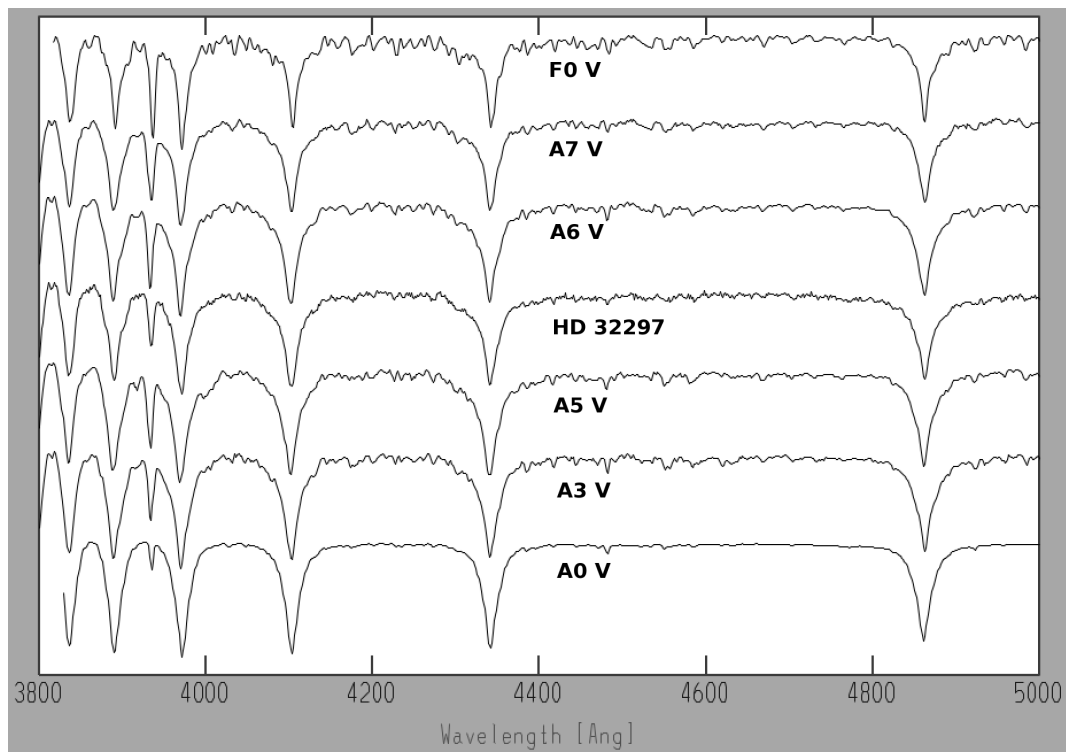


Figure 5.7 Visible spectrum of HD 32297, used for classifying its spectral type, which we classify as A6V.

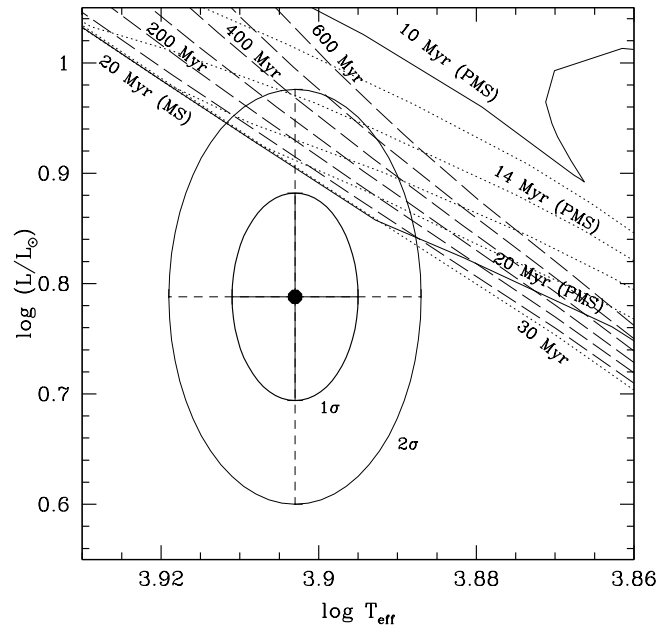


Figure 5.8 HD 32297's position on an HR diagram with pre-main sequence and main sequence isochrones from Bressan et al. (2012) for an assumed protosolar composition with  $Y = 0.27$ ,  $Z = 0.017$ . The star is likely older than  $\sim 15$  Myr and younger than  $\sim 500$  Myr.



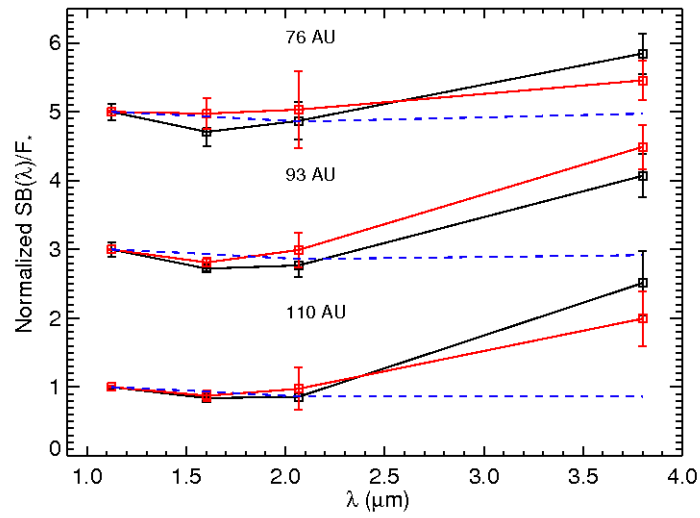


Figure 5.9 HD 32297 debris disk spectrum, along with the equivalent spectrum from the model of D13 (carbon, silicates, pourous water ice). Black corresponds to northeast, red corresponds to southwest, and dashed blue corresponds to the model. While the D13 model fits the 1-2  $\mu$ m data well, it fails to match the  $L'$  data.

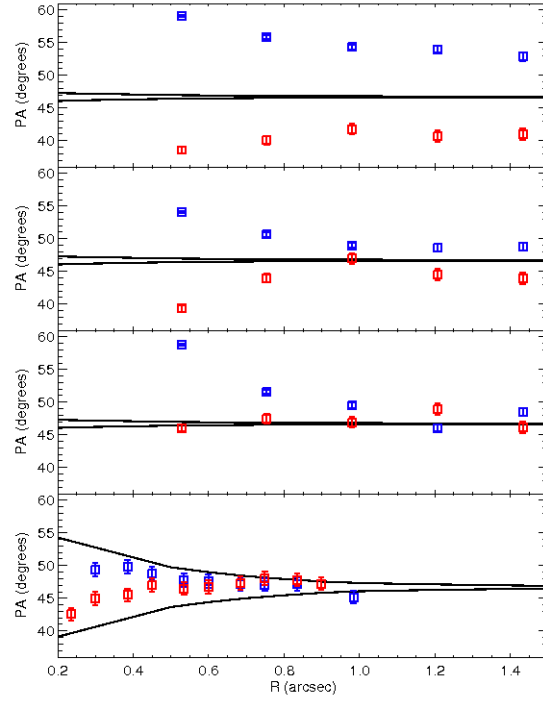


Figure 5.10 PA vs. distance from the star for the real disk data and the D13 model. The top panel corresponds to F110W, with each successive panel below increasing in wavelength. Red corresponds to northeast, blue corresponds to southwest, and the black lines correspond to the model. The PA changes by several degrees at each wavelength for the real disk, but these changes do not occur for the D13 model, implying poor agreement.

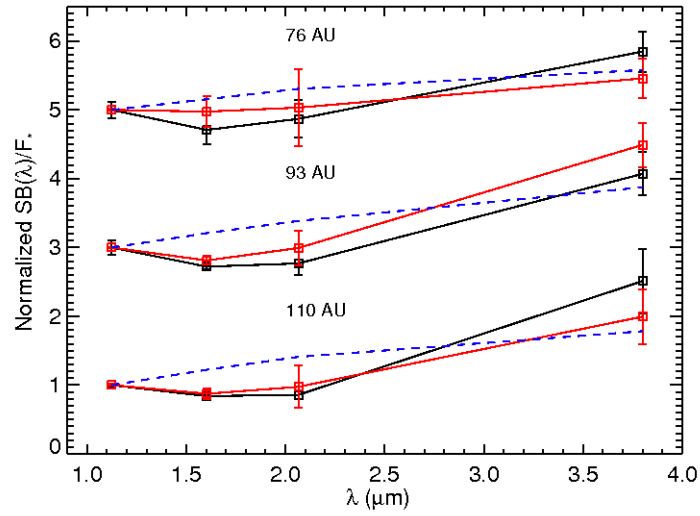


Figure 5.11 HD 32297 debris disk spectrum, along with the equivalent spectrum for 1  $\mu\text{m}$  tholins. Black corresponds to northeast, red corresponds to southwest, and dashed blue corresponds to the model. This model matches the red color of the disk at  $L'$  better, but is not a good fit at shorter wavelengths.

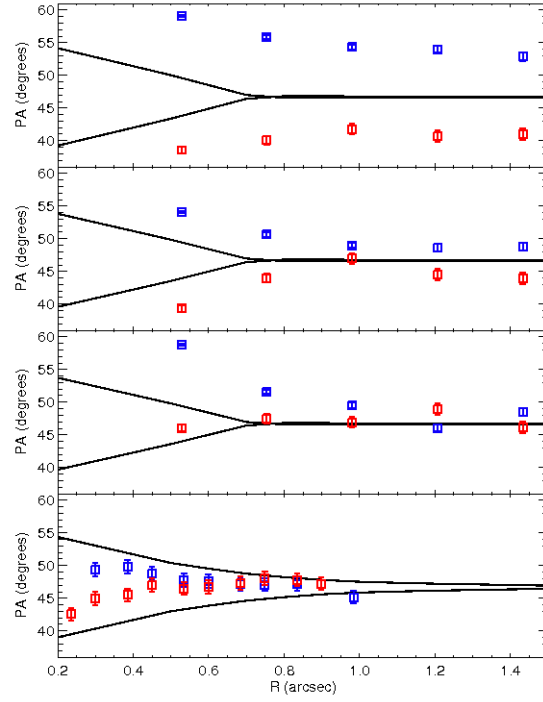


Figure 5.12 PA vs. distance from the star for the real disk data and the tholins model disk. The top panel corresponds to F110W, with each successive panel below increasing in wavelength. Red corresponds to northeast, blue corresponds to southwest, and the black lines correspond to the model. The tholins model disk changes in PA close to the star, as is seen for the real disk, but to a lesser extent.

## CHAPTER 6

EMPIRICAL CONSTRAINTS ON PLANETS SHEPHERDING DEBRIS DISKS FROM  
SCATTERED LIGHT OBSERVABLES

Planets can affect debris disk structure by creating gaps, sharp edges, warps, and other potentially observable signatures. Such features are now being discovered in scattered light images of debris disks. However, no general tool is yet available to observers to predict a disk-shepherding planet's properties from the observed features of the disk. Assuming these features are created solely by a single massive planet orbiting interior to the disk and in the same plane, we present a simple empirical procedure to help observers estimate the mass, semimajor axis, and eccentricity of such planets. These properties can be constrained with scattered light measurements of debris disks with ring-like structures (described by the disk's semimajor axis, eccentricity, and surface brightness full-width-half-maximum (FWHM)). We perform dynamical simulations of model systems consisting of a star, a single planet, and a disk of parent bodies and dust grains beyond the orbit of the planet to determine the resulting debris disk properties for a wide range of input parameters. We then derive an empirical equation that relates a debris disk's deprojected normalized FWHM to the maximum mass of its shepherding planet. We use this mass limit and the disk's eccentricity to estimate the planet's minimum semimajor axis and eccentricity. Assuming an initially infinitesimally-narrow ring of parent bodies, we find that more massive planets are required to produce broader debris rings, but there is no strong correlation with eccentricity. We apply our predictions to five well-known debris disks (Fomalhaut, HR 4796A, HD 207129, HD 202628, and HD 181327) to constrain the maximum allowable planet mass in each system. All work described below was

carried out by me, with helpful suggestions by Phil Hinz and Renu Malhotra.

## 6.1 Introduction

Circumstellar dust has been detected around several hundred main sequence stars, and more than 30 such systems have now been spatially resolved at visible, near-, and far-infrared wavelengths (<http://circumstellardisks.org>). In these so-called debris disk systems, the dust is inferred to be generated by collisions in planetesimal belts that are dynamically shepherded by planets, analogous to the solar system's asteroid and Kuiper belts. In a small number of systems, notably  $\beta$  Pictoris, Fomalhaut, and HR8799, spatially resolved debris disk structure as well as one or more planets have been detected (Lagrange et al., 2010; Kalas et al., 2008; Marois et al., 2010), allowing more detailed study of planet-planetesimal-disk interactions and of planetary system formation and evolution.

Currently there are many spatially-resolved debris disks known which do not have associated detections of planets, but many debris disks do show signs of shepherding planets, such as resolved gaps and sharp edges. Indeed the presence of a planet in the Fomalhaut system has been predicted based on the resolved disk's properties (Quillen, 2006), and Chiang et al. (2009) (hereafter C09) have carried out detailed dynamical modelling to constrain the planet's mass to  $< 3 M_J$  by consideration of the debris disk's observed properties. A faint object scattering star light has recently been imaged in the system (Kalas et al., 2008; Currie et al., 2012a; Galicher et al., 2012), but its true nature and origin remain ambiguous (Kalas et al., 2013).

The Fomalhaut dynamical predictions were very useful and exciting, but they were customized to a specific debris disk. What predictions can be made in the general case? Several studies have examined how planet mass affects debris disk

structure (Wyatt et al., 1999; Kuchner & Holman, 2003; Quillen, 2006; Chiang et al., 2009; Thebault et al., 2012), but these are not readily adapted for the inverse problem, namely computing the planet mass and orbit from a given set of debris disk observations.

The goal of the present paper is to provide observers with a “rough guide” for predicting the mass and orbit of a putative shepherding planet from scattered light observations of a debris disk. The procedure we present is obtained as follows: we carry out a suite of dynamical simulations of a single planet interacting with a ring of dust-producing planetesimals; the simulations cover a range of system parameters, and we obtain a suite of simulated debris disks. We calculate the optical depth profile (a proxy for surface brightness) of each simulated disk and measure the (normalized) full-width half-maximum (FWHM) of each ring. We then examine the relationships between the FWHM and the simulation input parameters. Specifically, we provide observers with a simple procedure to estimate the maximum mass of a putative shepherding planet, its orbital semimajor axis, and its eccentricity from surface brightness profiles of scattered light images of debris disks. In Section 6.2, we describe our methods. In Section 6.3, we describe our results. In Section 6.4, we apply our results to several observed debris disk systems and report our predictions for planets in these systems. In Section 6.5, we discuss our results on parent body disk widths. In Section 6.6, we summarize our results and outline the observer’s procedure for predicting a planet’s mass and orbit from scattered light images of debris disks.

## 6.2 Methods

In spatially resolved scattered light images of debris disks, if the disks are not too inclined relative to our line of sight, we can typically determine the following disk

parameters: the semimajor axis,  $a_{peak}$ , and the eccentricity,  $e_{disk}$ , and longitude of periastron,  $\varpi_{disk}$  of the deprojected disk by ellipse fitting; we can also determine the normalized FWHM of the surface brightness of the deprojected disk, defined here as

$$\text{FWHM} = \frac{a_{1/2}^{out} - a_{1/2}^{in}}{a_{peak}}, \quad (6.1)$$

where  $a_{1/2}^{out}$  and  $a_{1/2}^{in}$  are the semimajor axis where the deprojected disk surface brightness is half of the peak surface brightness ( $a_{peak}$ ).

We adopt the hypothesis that the scattered light of the debris disk arises from stellar light scattered by dust grains produced in an underlying ring of dust-producing planetesimals —“parent bodies”— shepherded by a nearby perturbing planet orbiting interior to its inner edge. We describe the parent body disk by the following parameters: its semimajor axis,  $a_{pb}$ , defined as the midpoint between the outer and inner edges of the parent body disk,  $a_{outer}$  and  $a_{inner}$ , respectively; the fractional width of the parent body disk,  $w = (a_{outer} - a_{inner})/a_{pb}$ ; the eccentricity of the parent body disk,  $e_{pb}$ ; and the longitude of periastron of the parent body disk,  $\varpi_{pb}$ . The perturbing planet’s parameters are its mass,  $m_p$ , its orbital semimajor axis,  $a_p$ , eccentricity,  $e_p$ , and longitude of periastron,  $\varpi_p$ . We assume that the midplane of the planetesimal disk coincides with the orbital plane of the planet.

We make several additional simplifying assumptions. Because our study concerns debris disks (where little or no gas is present), the forces acting on dust grains are primarily: gravity from the host star, gravity from the perturbing planet, radiation pressure from the host star, and Poynting-Robertson (PR) light drag. In addition, the lifetimes of dust grains are limited by grain-grain collisions, for these lead to catastrophic fragmentation. For a geometrically absorbing dust grain of bulk density  $\rho$  and radius  $s$ , the ratio,  $\beta$ , of the radial force of stellar



radiation pressure to the force of stellar gravity is,

$$\beta = \frac{3L_*}{16\pi GM_* c \rho s}, \quad (6.2)$$

where  $L_*$  and  $M_*$  are the stellar luminosity and mass,  $G$  is the universal constant of gravitation, and  $c$  is the speed of light. In response to radiation pressure, dust grains generated by parent bodies moving on circular orbits acquire larger, more eccentric orbits, with semimajor axis and eccentricity given by

$$a = a_{pb}(1 - \beta)/(1 - 2\beta), \quad e = \beta/(1 - \beta). \quad (6.3)$$

Only the particles with  $\beta < 0.5$  remain bound to the star; in other words, bound particles are larger than the “blow out” size (C09),

$$s_b = \frac{3L_*}{8\pi GM_* c \rho s} = 1.16 \left( \frac{\rho}{1 \text{ g cm}^{-3}} \right)^{-1} \left( \frac{L_*}{L_\odot} \right) \left( \frac{M_*}{M_\odot} \right)^{-1} \mu\text{m}. \quad (6.4)$$

Smaller particles,  $s < s_b$ , acquire hyperbolic orbits upon release from the parent bodies, and their residence time in the debris disk is

$$t_b \approx \frac{w}{\Omega(a_{pb})} = 16 \left( \frac{w}{0.1} \right) \left( \frac{a_{pb}}{100 \text{ AU}} \right)^{3/2} \left( \frac{M_*}{M_\odot} \right)^{-1/2} \text{yr}, \quad (6.5)$$

where  $\Omega(a) = \sqrt{GM_*/a^3}$  is the local Keplerian frequency and  $w$  is the orbital frequency of the dust particles. (For parent bodies on modestly eccentric orbits, the orbit of the dust grain depends on the longitude at which it is released, and so does the minimum blow out size, but the latter is still close to  $s_b$  given above.) For the bound dust grains, PR drag causes orbits to circularize on a timescale

$$\begin{aligned} t_{PR} &= \left| \frac{\dot{e}}{e} \right|^{-1} = \frac{32\pi \rho s c^2 a^2 \sqrt{1-e^2}}{15L_*} \\ &\approx 7 \times 10^6 \frac{(1-\beta)}{\beta(1-2\beta)^{3/2}} \left( \frac{M_*}{M_\odot} \right)^{-1} \left( \frac{a_{pb}}{100 \text{ AU}} \right)^2 \text{yr}; \end{aligned} \quad (6.6)$$

the orbit decay timescale is  $|\dot{a}/a|^{-1} \approx 2(1 - 2\beta)t_{PR}$  for  $\beta \lesssim 0.5$ .

The characteristic lifetime for destruction of grains by grain-grain collisions in the bound population is (C09),

$$\begin{aligned}
 t_{\text{collision}} &\sim \left( \frac{\tau_R \Omega(a)}{w} \right)^{-1} \\
 &\sim 5 \times 10^4 \left( \frac{10^{-3}}{\tau_R} \right) \left( \frac{w}{0.1} \right) \left( \frac{a_{pb}}{100 \text{ AU}} \right)^{3/2} \left( \frac{M_*}{M_\odot} \right)^{-1/2} \text{ yr}, \quad (6.7)
 \end{aligned}$$

where  $\tau_R$  is the radial optical depth, and  $\tau_R/\sqrt{w}$  accounts for the effective optical depth for the path length  $a_{pb}\sqrt{w}$  traversed by a dust grain on an elliptical orbit of eccentricity near unity. In Eqs. 6.6 and 6.7 we have also used the relation between the dust grain's orbital parameters and those of the parent bodies,  $a_{pb}$  (Eq. 6.4).

Comparing these three timescales for dust grains, we see that  $t_{PR} \gg t_{\text{collision}} \gg t_b$  (as in C09, Wyatt (2005)). This means that particles below the blowout size do not contribute to the brightness of a debris disk; and on timescales on the order of their lifetimes,  $\sim t_{\text{collision}}$ , the bound dust grains' orbits do not change significantly from their initial orbits upon “release”. This justifies our neglect of PR drag in the simulations described below.

Planetary perturbations have several effects: they shepherd the orbits of parent bodies, and they also truncate the distribution of dust grain orbits, as close encounters with the planet can eject grains from the system. We use numerical simulations to account for these effects.

For the numerical simulations, we use a fast n-body orbit integrator, based on the second order mixed-variable method of Wisdom & Holman (1991). The effects of radiation pressure on dust grains are included as a modification to stellar gravity by multiplying the stellar mass by  $1 - \beta$ . This code, written in FORTRAN, provides an order of magnitude increase in speed compared to conventional integrators, while minimizing numerical losses in the constants of integration (energy, angular momentum, Jacobi constant). To illustrate, a simulation of 10,000

particles interacting with a star and a perturbing planet for 1000 orbits of the planet, and using an integration step size of 5% of the planet's orbital period, takes only  $\sim 1$  minute of wall clock time on a 2010 computer<sup>1</sup>.

### 6.2.1 Initial conditions

The star, planet, and parent bodies all orbit in the same plane so that their relative inclinations are zero. This assumption is made for simplicity and should not seriously change the results since most debris disks are flat (aspect ratio, defined as disk height divided by disk radius, on the order of a few percent).

We adopt units whereby the stellar mass  $M_*$  and the universal constant of gravitation,  $G$ , are unity, and the inner edge of the initial parent body disk,  $a_{inner}$  is adopted as the unit of length. In these units, a particle orbiting at  $a_{inner}$  has a period of  $2\pi$ . We simulate systems with mass ratio  $\mu$  in the range (0.3, 1.0, 3.0, 10.0)  $\mu_J$ , where  $\mu_J$ , the mass ratio for Jupiter relative to our Sun,  $= 10^{-3}$ . Although smaller planet masses are likely present in debris disks, we do not simulate these cases because Thebault et al. (2012) showed that over a wide range of optical depths and for  $\mu < 0.3 \mu_J$ , dust grain collisions can wash out observable effects on debris disks.

The parent bodies' semimajor axes are all initialized at  $a_{inner}$ . We also tested disks with non-zero initial widths but found that these cases introduced a degeneracy with planet mass/semimajor axis combinations. For example, imagine a debris disk with an initial parent body disk width of 10% that has a planet of a given mass a given distance away from its inner edge. Over time, the disk broadens to 15% from interactions with the planet. Now imagine a second disk whose initial width was 15% with a very low-mass perturbing planet. This disk will remain at 15%, but an observer has no way of knowing which planet produced

---

<sup>1</sup>Macbook Pro, 4 GB memory, 2.66 GHz Intel Core 2 Duo

the disk without knowing the initial parent body disk width, which cannot be measured. If we instead consider initially infinitesimally-narrow rings, then for a given observed disk width, we can at least constrain the maximum mass of the putative planet.

The initial eccentricities of all parent body disks are (0, 0.05, 0.1, 0.15, 0.2). These values adequately span known debris disk eccentricities. The parent bodies all have the same initial longitude of periastron, which we initialize to zero.

We set the planet's eccentricity to be equal to its parent disk's eccentricity. While other studies have used the forced eccentricity relationship between the planet and the dust (e.g., Quillen (2006) and C09), this relationship is derived from linear secular theory, which is only valid for small mass ratios ( $\mu < 10^{-3}$ ). The larger mass ratios we are testing would require that the planets be much more eccentric than their parent disks. This would cause the planets to dynamically disturb the dust more. At small mass ratios, the difference between the forced eccentricity of the planet and the eccentricity of the disk is very small, so we do not anticipate any problems with our choice of planet eccentricity.

The initial semimajor axis of the planet is determined by means of a bootstrap procedure in which we numerically determine the inner edge of stable orbits exterior to the planet's orbit for the ranges of planet mass and eccentricity of interest. Although we could have made use of published formulas for the chaotic zone of a planet (e.g., Wisdom (1980); C09; Mustill & Wyatt (2012)), the results in the literature do not adequately cover the range of planet mass of interest in our study. Therefore, we determine the semimajor axis of the planet relative to the inner stable edge of the parent body disk as follows: we place a planet of a given mass at  $a_{inner}$  ( $= 1$ ) and parent bodies at discrete semimajor axis locations  $> a_{inner}$ , with random mean anomalies between  $0-2\pi$ , starting far from the planet. The parent

bodies have the same eccentricity as the planet (in the range 0-0.2). The system is then integrated for 1000 orbits of the planet. In this simulation and all others described below, we use an integration step size of 5% of the orbital period of a particle with semimajor axis =  $a_{inner}$ . Parent bodies that approach within the planet's Hill radius or cross within  $0.1 a_{inner}$  of the star or beyond  $100 a_{inner}$  are discarded. The width of the unstable zone is determined as the closest location at which at least 90% of the parent bodies remain at the end of the simulation. These locations are reported in Table 6.1. From Table 6.1, the initial eccentricity of the

Table 6.1 Numerically determined  $a_p/a_{inner}$

$e_{disk,i}$	$\mu/\mu_J = 0.3$	$\mu/\mu_J = 1$	$\mu/\mu_J = 3$	$\mu/\mu_J = 10$
0	0.86	0.80	0.71	0.59
0.05	0.86	0.80	0.70	0.55
0.10	0.86	0.80	0.69	0.52
0.15	0.86	0.79	0.69	0.49
0.20	0.84	0.79	0.67	0.47

disk widens the chaotic zone only for the largest mass ratios. However, the initial eccentricities of debris disks cannot be measured. Therefore we cannot compute a master chaotic zone equation from the numbers in Table 6.1. Instead, because we are attempting to constrain the *maximum* mass of a disk-shepherding planet in this study, we can only constrain the *minimum* semimajor axis of a putative planet. Therefore we construct a chaotic zone equation for the  $e_{disk,i} = 0.20$  case, since these correspond to the widest chaotic zones and the planets that are the farthest from the disk inner edges:

$$a_p = a_{inner} / (1 + 10.23\mu^{0.51}) . \quad (6.8)$$

To review, we have two free parameters that will be varied in the simulations:

$m_p$  and  $e_{disk,i}$ . Note that  $a_p$  depends on  $m_p$  through Eq. 6.8,  $e_p = e_{disk,i}$ , and  $\varpi_p = \varpi_{pb}$ . The simulations will produce two outputs: FWHM, calculated using Eq. 6.1, and  $e_{disk,f}$ , the final fitted eccentricity of the simulated disks.

With all parent body and planet input parameters determined, we integrate the system of the star, planet, and 5000 parent bodies for 1000 orbital periods of a particle at  $a_{inner}$ . After 1000 orbits, the parent bodies “release” dust grains that have the same positions and velocities as their parents, as in C09. The dust grain orbits are then computed, accounting for the effects of radiation pressure (parameterized by  $\beta$ ).

As in C09, we then numerically integrate the system for 8 different values of  $\beta$ ; including  $\beta = 0$ , these are: (0.0, 0.00625, 0.0125, 0.025, 0.05, 0.1, 0.2, 0.4). We integrate each system with a given  $\beta$  for 100 orbit periods of a particle at  $a_{inner}$ . The length of this integration is approximately the collisional lifetime of a dust particle in the debris disk (Eq. 6.7). We also carried out longer (1000 orbit) integrations (corresponding to collisional timescales in lower optical depth disks) but found that the choice of integration time made little difference on the overall results discussed below (predicted masses and orbits).

To obtain the optical depth profiles of the simulated debris disks, we take each surviving dust particle’s final  $x$  and  $y$  positions and velocities, construct a grid of concentric ellipses with eccentricity given by the final eccentricity of the parent body disk,  $e_{disk,f}$ , and ellipse center given by  $a_{disk}e_{disk,f}$ , and count the total number of surviving particles in a given ellipse. Here,  $e_{disk,f}$  is the maximum of the eccentricity distribution of the surviving parent bodies, and  $a_{disk}$  is the maximum of the semimajor axis distribution.

To increase the signal-to-noise, we “spread” each dust particle out along its orbit (“Gaussian wire method”) as in C09. In this method, a surviving particle

is cloned and placed at discrete locations along its orbit; the orbital elements are determined from the position and velocity of the particle at the end of the integration and account for the effects of radiation pressure. The number of particle clones generated per orbit is chosen so that the total number of particles equals  $10^6$ . For example, if 5000 particles survive, then each particle would be “spread” along its orbit at 200 locations equally spaced in true anomaly. For the  $\beta > 0$  particles, each particle has a weight that is inversely proportional to its velocity at the end of the integration, effectively causing slower moving particles to create greater dust density.

The number of ellipses used to construct the optical depth profile—which determines the “resolution” of the final profile—is 50, with the first ellipse at  $0.83 a_{inner}$  and the last at  $1.83 a_{inner}$ . This results in an optical depth resolution of  $0.02 a_{inner}/\text{ellipse}$ . This is lower than the resolution used in C09 (200 ellipses), but is well-matched to current observations. For example, if  $a_{inner} = 50\text{-}100$  AU (most debris disks reside at these separations), and 1 ellipse = 1 resolution element, then the resolution is 1-2 AU. This is comparable to the typical resolution achieved by HST for debris disks 50-100 pc from Earth.

For a given planet mass and disk eccentricity, we produce the final optical depth profile  $\tau_{\perp}$  in the same manner as C09, by linearly combining the 8 different optical depth profiles for each  $\beta$ :

$$\tau_{\perp} = \sum_{\beta \neq 0} N_{\beta} \frac{\max(N_{0.00625})}{\max(N_{\beta})} \left( \frac{\beta}{0.00625} \right)^{q-3} + N_0 \frac{\max(N_{0.00625})}{\max(N_0)} (1 + \sqrt{2}), \quad (6.9)$$

where  $N_{\beta}$  refers to the optical depth profile for a specific  $\beta$ ,  $q$  is the differential power-law index assuming a collisional cascade in the disk and here assumed to be 3.5 (Dohnanyi, 1969), and the  $1 + \sqrt{2}$  term comes from the choice of binning

(see C09, section 3.1.3 for a more in depth discussion of this constant term). See Table 6.2 for a full list of all chosen simulation parameters.

Table 6.2 Simulation Parameters

Parameter	Value
$\mu/\mu_J$	(0.3, 1.0, 3.0, 10.0)
$e_{disk,i}$ ( $= e_p$ )	(0.0, 0.05, 0.10, 0.15, 0.20)
$a_{inner}$	1
$\beta$	(0.0, 0.00625, 0.0125, 0.025, 0.05, 0.1, 0.2, 0.4)
Number of test particles	5000
total integration time	100-1000 orbits
time step	5%

### 6.2.2 Control simulation

Before running a full suite of n-body simulations, we verified that our simulations were producing results similar to those obtained by C09. While their input parameters (mass ratio, planet/disk eccentricity, initial parent body disk width) differ from ours, the general set up and methodology are very similar. Therefore we should expect to see similar results for similar inputs.

Fig. 6.1a shows our  $\beta$  profiles for the specific case of  $\mu/\mu_J = 0.3$  and initial disk eccentricity = 0.10. The profiles are very similar to Fig. 2 in C09. This gives us confidence that our simulations will yield accurate results, despite our differences relative to C09.

We also verified that the perturbing planet was having the expected effect on the dust particles, namely spreading them out, resulting in wider optical depth profiles with increasing mass (as was seen by C09). Fig. 6.1b shows such an ex-



ample simulation for an initial disk eccentricity of 0.1. The expected behavior is observed, again validating the methods and parameters chosen for the simulations.

### 6.3 Results

After running the full suite of simulations, we measured  $a_{1/2}^{out}$ ,  $a_{1/2}^{in}$ , and  $a_{peak}$  for each  $\beta$ -summed optical depth profile (as in Fig. 6.1b) and computed the normalized FWHM of each modeled disk using Eq. 6.1. We then examined the relationships between this output and the planet mass ratio and final disk eccentricity. We cannot use the initial disk eccentricity as an independent variable because, depending on the mass of the perturbing planet, it can increase or decrease from its original value (see Fig. 6.2). Therefore we first examine the relationship between each disk's normalized FWHM and its final disk eccentricity (see Fig. 6.3). From Fig. 6.3, there is no strong correlation between these two variables. This means that disk eccentricity may *not* be an indicator of a nearby massive planet (neglecting the possible dynamical interactions that could have excited the disk into an eccentric state in the first place).

Viewing final disk eccentricity as having little effect on the disk's width, we now examine the relationship between the normalized disk FWHM and the planet mass ratios (see Fig. 6.4). Evidently increasing the mass ratio of the perturbing planet causes an increase in the range of possible disk FWHM values.

Fitting a line to data yields an equation which can be used to estimate the maximum mass of a perturbing planet in a debris disk. To estimate the uncertainties in the slope and y-intercept, we fit all possible combinations of points and set the averages of the minimum and maximum slopes and y-intercepts as the uncertainties in each parameter, respectively. We then propagated these er-

rors to obtain a total error for each predicted mass. Eq. 6.10 shows our linear fit to the data, along with the uncertainties in the slope and y-intercept. Interestingly, our fitted slope is not too different from the slope ( $\sim 0.03$ ) obtained by fitting the normalized FWHM values from Fig. 3 in C09 for the specific case of Fomalhaut. Despite the differences between our specific simulations (mass ratios, eccentricities, parent body disk widths, chaotic zone widths, and integration times), it is encouraging to see similar results.

$$\text{FWHM} = (0.019 \pm 0.0064)\mu/\mu_J + (0.107 \pm 0.032). \quad (6.10)$$

Inverting Eq. 6.10, we now have an empirical estimate of the maximum mass of a disk-shepherding planet that depends solely on the disk's scattered light FWHM:

$$\mu/\mu_J = \frac{\text{FWHM} - (0.107 \pm 0.032)}{0.019 \pm 0.0064}. \quad (6.11)$$

### 6.3.1 Caveats

Before making predictions for potential planets shepherding known disks, we outline several caveats in this work that need to be considered. We made several assumptions that enabled us to take shortcuts so that we could perform many simulations relatively fast. We sought dynamical stability of all parent bodies for only  $10^3$  orbits. Integration times of  $> 10^6$  orbits would have been more realistic since debris disks are generally old, typically  $\sim 1$  Gyr. Nonetheless our shorter integrations provide a good approximation because test particle dynamical lifetimes near planets have approximately logarithmic distributions (Holman & Wisdom, 1993; Minton & Malhotra, 2010) so that longer integration times will not significantly change the stable population.

We also assumed that integrating the dust particles for 100 orbits was satisfactory for all debris disks. Since we assumed that all debris disks are collision-

dominated, we only needed to integrate for the length of time that a particle survives before being destroyed by collisions, which is directly related to a debris disk's optical depth. This amount of time should technically change for each system, so our results will not be accurate for all disks. Nonetheless most debris disks' optical depths are within  $\sim$  an order of magnitude of each other, and we also found that integrating for longer times (e.g., 1000 orbits) made little difference on the final results.

The assumption that all debris disks are collision-dominated may also not be true, so our results technically should apply only to collision-dominated disks. We assumed a differential power-law index for collisional cascades of 3.5, based on Dohnanyi (1969). This is a common assumption but will certainly not be valid for all debris disks. Gáspár et al. (2012) found evidence for the index being closer to 3.65, but this difference is small and should not seriously affect our results.

We assumed that the initial parent body disk width was zero to remove degeneracies in this parameter. It is probable that parent bodies in debris disks are not initially confined to infinitesimally-narrow rings; however, this assumption does not preclude us from estimating the maximum mass of a disk-shepherding planet. For a debris disk of a given width, from our study an observer can rule out planets above a certain mass that would have dynamically broadened the disk more than is observed.

Finally, we stress that our models cannot explain all sharp, eccentric debris rings. Rather, the goal of this study was to answer the following question: *if the observed disk features are being created by a single disk-shepherding planet*, how massive is that planet and what is its orbit like? It is certainly possible that other physical processes (e.g., dust grain collisions, radiation forces, dynamical interactions with a distant binary, dynamical interactions with the interstellar medium, dy-

namical interactions with multiple low-mass planets (e.g., Raymond et al. (2011, 2012)), or even gas (Lyra & Kuchner, 2013)) could produce disk features that we assume are created by a single planet.

## 6.4 Predictions for resolved debris rings

### 6.4.1 Fomalhaut

Fomalhaut is a very nearby A star with a debris disk detected in scattered light (Kalas et al., 2005) and a possible point source shepherding the ring (Kalas et al., 2008; Janson et al., 2012; Currie et al., 2012b; Galicher et al., 2012). Recent evidence suggests that the point source may not be dynamically sculpting the ring (its orbit may be very eccentric and could cause it to cross through the plane of the ring in the future (Kalas et al., 2013)). Nonetheless it is useful to estimate the maximum mass of a planet shepherding the disk in the system, since such a planet may still exist in the system and future observations will seek to detect it if it exists. Since the disk's eccentricity is not a good predictor of planet mass, we need only the disk's deprojected normalized FWHM. This is  $\sim 0.17$  (Kalas et al., 2005). Inputting this value into Eq. 6.11 and multiplying by the star's mass of  $2.3 M_{\odot}$ , we find a maximum planet mass of  $\sim 7.6 \pm 4.6 M_J$ . The planet's eccentricity would be equal to the disk's (0.11), and its semimajor axis would be  $\gtrsim 85$  AU from Eq. 6.8. Taking into account the inclination to the system, the minimum orbit-averaged projected separation would be  $\sim 4''4$ . Recent imaging studies have already ruled out planets more massive than  $\sim 3 M_J$  at these distances, so our dynamical constraint is not very powerful in this case.

### 6.4.2 HR 4796A

HR 4796A has a bright debris disk that has been resolved at many wavelengths (e.g., Schneider et al. (2009); Thalmann et al. (2011); Lagrange et al. (2012)). In

scattered light, the disk appears as a narrow ring, with a large central gap between the disk and the star. The gap, the sharp inner and outer edges, and a small offset from the star are cited as evidence for a perturbing planet (Schneider et al., 2009; Thalmann et al., 2011; Wyatt et al., 1999). To date no planet has been detected, though Lagrange et al. (2012) ruled out  $3.5 M_J$  planets beyond  $0''.5$  (36.5 AU projected separation).

According to Schneider et al. (2009), the disk's normalized FWHM is  $\sim 0.18$  from the deprojected radial surface brightness profile. With a stellar mass of  $2.18 M_\odot$ , we predict the maximum mass of a perturbing planet would be  $\sim 7.7 \pm 4.5 M_J$ . The planet's eccentricity would be equal to the disk's ( $\sim 0.05$  from Schneider et al. (2009) and Thalmann et al. (2011)), and its semimajor axis would be  $\gtrsim 44$  AU. Its orbit-averaged minimum projected separation would be  $0''.14$ . This is closer to the star than the detections limits reached by Thalmann et al. (2011) and Lagrange et al. (2012), so we advocate additional high-contrast imaging of this system.

#### 6.4.3 HD 207129

HD 207129 is a Sun-like star that has a large, faint debris disk, recently resolved in scattered light by Krist et al. (2010) with HST. The disk has a normalized FWHM of  $\sim 0.18$ . Taking a stellar mass of  $1.1 M_\odot$  (Krist et al., 2010), we obtain using Eq. 6.10 a maximum planet mass  $4.2 \pm 2.3 M_J$ . Since the eccentricity of the disk is only constrained to be  $< 0.08$ , the same constraint applies to the planet's eccentricity. Its semimajor axis would be  $\gtrsim 92$  AU. The minimum orbit-averaged projected separation on the sky of this putative planet would be  $\sim 2''.8$ . Despite this large separation, the star's old age ( $\sim 1$  Gyr from Krist et al. (2010)) and small maximum planet mass would likely make detecting the planet difficult.

#### 6.4.4 HD 202628

HD 202628 is a Sun-like star with a large debris disk recently resolved by HST and similar in structure to that of Fomalhaut (Krist et al., 2012). The disk has a normalized FWHM of  $\sim 0.4$  and an eccentricity of  $\sim 0.18$ . Assuming a solar mass for the star, the maximum mass of a single perturbing planet would be  $\sim 15.4 \pm 5.5 M_J$ . Its eccentricity would be 0.18, and its minimum semimajor axis would be  $\sim 71$  AU. Given the planet's large possible mass, along with a minimum orbit-averaged projected separation of  $\sim 1''2$ , we strongly encourage high-contrast imaging of this system.

Table 6.3 Predicted Masses and Orbits

Star	$m_p/M_J$	$a_p/\text{AU}$	proj. sep. ( $''$ )*	$e_p$
Fomalhaut	$< 7.6 \pm 4.6$	$> 85$	$> 4.4$	0.11
HR 4796A	$< 7.7 \pm 4.5$	$> 44$	$> 0.14$	0.05
HD 207129	$< 4.2 \pm 2.3$	$> 92$	$> 2.8$	$< 0.08$
HD 202628	$< 15.4 \pm 5.5$	$> 71$	$> 1.2$	0.18
HD 181327	$< 15.2 \pm 5.6$	$> 35$	$> 0.55$	0

\*Orbit-averaged

#### 6.4.5 HD 181327

HD 181327 is a Sun-like star with a large, bright debris disk resolved by HST (Schneider et al., 2006). The most current analysis of the resolved images reveals that the disk has a normalized FWHM of 0.32 (Lebreton et al., 2012) and an eccentricity consistent with zero (Stark et al. 2013, in prep.). For a stellar mass of  $1.36 M_\odot$  (Lebreton et al., 2012), the planet's maximum mass would be  $\sim 15.2 \pm 5.6 M_J$ . Its eccentricity would be  $\sim 0$  and its minimum semimajor axis would be  $\sim 35$  AU (minimum orbit-averaged projected separation  $\sim 0''55$ ). Schneider et al.

(2006) claim that planets more massive than  $\sim 10 M_J$  beyond 52 AU could have been detected in the HST images, not quite reaching the limits calculated here. Given the large maximum mass of the putative planet, we advocate additional high-contrast imaging of this system.

See Table 6.3 for a summary of the predicted masses and orbits for planets in each system.

### 6.5 Parent body disk widths

The predictions for planet mass and orbit in this study make use of the dynamical effects on dust grains. Are there any dynamical signatures on the parent bodies that produce the dust? Fig. 6.5 shows the normalized parent body disk width as a function of planet mass ratio. Clearly there is more scatter such that degeneracies in mass exist for widths  $\lesssim 10\%$ . However, for parent body disk widths  $\gtrsim 10\%$ , the planet mass ratio must be  $> 3 \mu/\mu_J$ . Since we can only estimate the maximum mass of a putative planet from this study, this means that for a parent body disk width of 10% or less, we know the putative planet cannot be more massive than  $\sim 3 \mu/\mu_J$ , otherwise the width would be larger.

In the ideal case, observers would have scattered light images of debris disks, since our predictions are more precise using scattered light measurements. However, this is not always possible, as many known debris disks have not yet been spatially resolved. Instead, their existence is inferred from spectral energy distribution (SED) modeling using long wavelength data (from, in particular, Spitzer). In some cases, models can estimate the location and width of the parent body disk. These particular systems could make use of our predictions for parent body disk widths described above.

In cases where both images of the dust disk and the parent bodies are ob-

tained (e.g., with ALMA (Boley et al., 2012)), the dynamical models used here and in other works can be refined. This will help better constrain the properties of putative shepherding planets.

## 6.6 Summary: Observer's Procedure

The mass limits reported in this work are maximum values because we assumed the parent bodies were originally confined to infinitesimally-narrow rings. This is almost certainly not the way nature works, but it is adequate for allowing observers to estimate the maximum masses of putative planets in debris disks. Our predictions can then serve as starting points for determining which systems are favorable for direct imaging follow-up.

Given our simple assumptions, we have provided a general equation to estimate the maximum mass of a planet perturbing a debris disk. Our results indicate that this mass increases proportionally with the measured FWHM of the disk in a deprojected scattered light image.

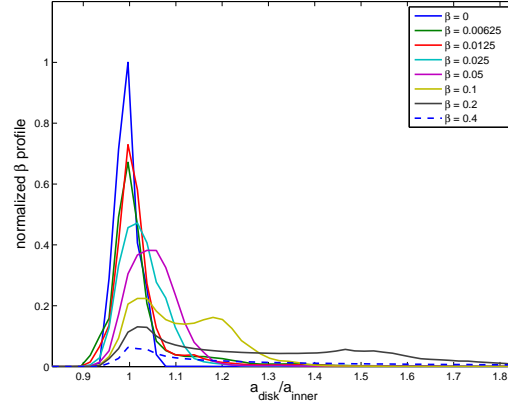
Below we summarize the exact procedure an observer should carry out to determine the maximum mass and orbit of a putative perturbing planet:

1. Construct the azimuthally-averaged radial profile of the disk's deprojected scattered light and normalize the profile by the maximum value.
2. Determine the semimajor axis of the peak, and the two locations equal to half the peak ( $a_{peak}, a_{1/2}^{in}, a_{1/2}^{out}$ ).  $a_{inner}$  can be set equal to  $a_{1/2}^{in}$ . Plug these into Eq. 6.1 to calculate the disk's normalized FWHM.
3. Calculate the eccentricity of the debris disk,  $e_{disk,f}$ , from the deprojected scattered light image. The planet's eccentricity = this value.

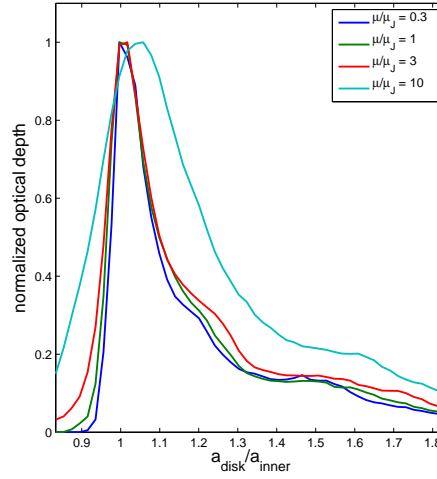


4. Plug the disk's normalized FWHM into Eq. 6.11 to solve for the maximum mass of the perturbing planet.
5. Plug the planet's mass and  $a_{inner}$  into Eq. 6.8 to solve for the planet's minimum semimajor axis.

Our predictions for the few resolved debris disks with gaps have interesting implications. For Fomalhaut and HR 4796A, deep imaging has already yielded mass limits well below the maximum masses we report here. For HD 207129, despite the favorable separation between the star and putative planet, the maximum planet mass of only  $4.4 M_J$ , combined with a likely age of  $\sim 1$  Gyr (Krist et al., 2010), make this system unfavorable for direct imaging. However for HD 202628 and HD 181327, the maximum planet masses of  $\sim 15 M_J$  in each system, along with the large projected separations of such planets, warrant additional high-contrast imaging.



(a)



(b)

Figure 6.1 *Top*:  $\beta$  profiles for  $\mu = 0.3\mu_J$  and initial  $e_{disk,i} = 0.10$ . The profiles are very similar to what C09 observe for  $\mu = 0.44\mu_J$ ,  $e_p = 0.12$ , and parent body disk width = 10%. *Bottom*:  $\beta$ -summed optical depth profiles for different  $\mu$  values, all with  $e_{disk,i} = 0.10$ . As the mass ratio increases, the profiles spread out, as is observed by C09 for their Fomalhaut simulations.

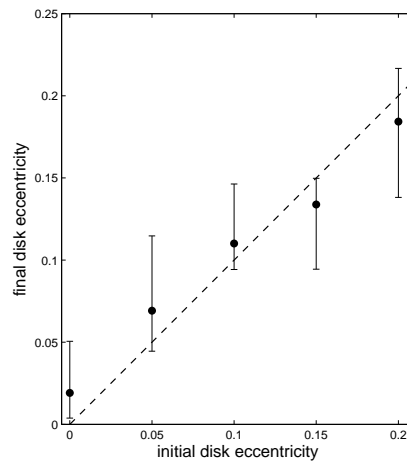


Figure 6.2 Final disk eccentricity as a function of initial disk eccentricity for the various input planet masses. The points represent the averages of the final disk eccentricity values across mass, and the error bars represent the full range in values. The dashed line denotes final and initial eccentricity values that are equal. The introduction of a massive perturbing planet into the system can result in both an increase and a decrease in the disk's eccentricity, depending on the mass and initial eccentricity.

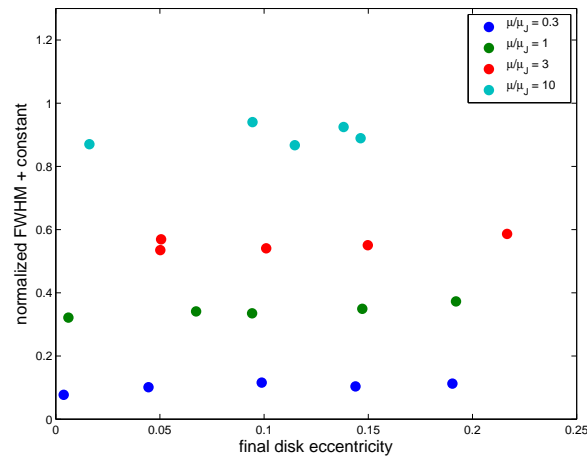


Figure 6.3 Normalized disk FWHM as a function of final disk eccentricity for the various input planet masses. The different colors are each associated with a different mass ratio planet, and constant terms have been added to the FWHM values for graphical clarity. There is no strong correlation between a debris disk's width and its eccentricity. This implies that disk eccentricity may not be a good indicator of a nearby perturbing planet.

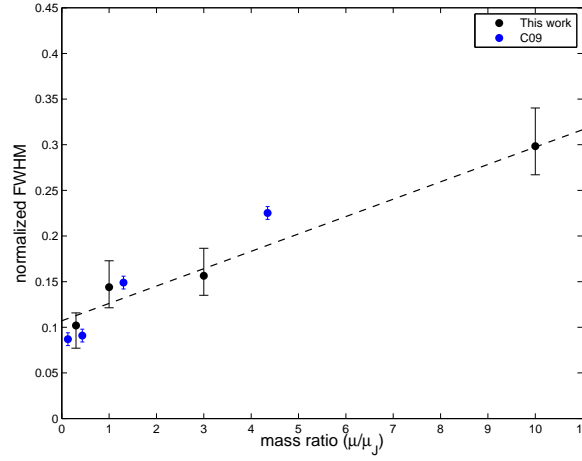


Figure 6.4 Normalized disk FWHM as a function of planet mass ratio. The black points represent the averages of FWHM values at each mass for the various final disk eccentricities, and the error bars represent the full range in FWHM values for each mass. The dashed line represents a linear fit to the points. The blue points and error bars represent equivalent values taken from Fig. 3 in C09. Evidently increasing the mass ratio of the perturbing planet causes an increase in the range of possible disk FWHM values. A similar effect was seen in C09 for the specific simulation parameters tested for Fomalhaut.

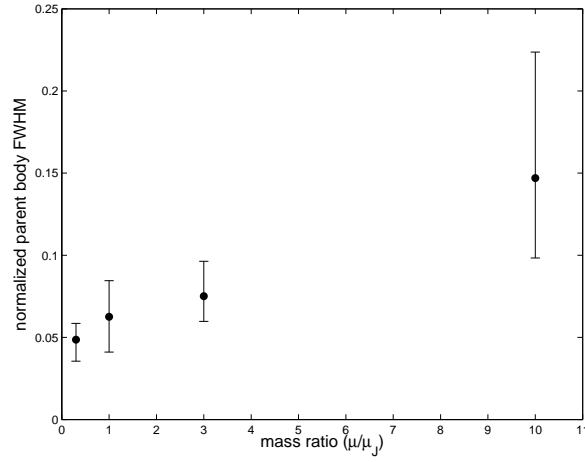


Figure 6.5 Normalized parent body disk FWHM as a function of planet mass ratio. The black points represent the averages of the values at each mass for the various disk eccentricities, and the error bars represent the full range in FWHM values for each mass. While a linear trend is evident, there is much more scatter than in the plot relating the dust disk FWHM to the planet mass ratio (Fig. 6.4), making the predictive power less precise. However, we can infer that parent body disk widths  $< 10\%$  cannot contain a planet with mass ratio  $\gtrsim 3 \mu/\mu_J$ .

## CHAPTER 7

## CONCLUSIONS

## 7.1 Summary

In this thesis, I have described work that aims to help answer two questions currently unanswered in the field of exoplanets: what are the typical masses and orbits of exoplanets?; and do the building blocks for life—water and organic materials—exist outside the solar system in other debris disks? While my work has nowhere fully answered these questions, it has laid the groundwork for future studies that surely will.

My work on examining the eccentricity distribution of known RV-detected exoplanets, discussed in Chapter 2 (Rodigas & Hinz, 2009), showed that there may be many more multi-planet, circular-orbit planetary systems than previously thought. This is useful because it paints the solar system as not so strange anymore. It will also help observers choose future targets for direct imaging. While current technology makes directly detecting RV planets too difficult due to their old ages and low luminosities, future extremely large telescopes (ELTs) will likely have more luck. Since there are nearly 1000 RV detected planets, observers can cull their target lists using my prediction that planets having eccentricities in the 0.1-0.2 range will be most likely to have wide companions.

The predictions discussed in this work have also already yielded promising results. Two known RV systems each with one previously-detected mildly-eccentric planet have both been recently revised as systems with multiple low-eccentricity planets (Wittenmyer et al., 2012). Recent studies also suggest that the planetary system around GJ 581 has five planets on nearly circular orbits rather than four planets on eccentric orbits (Vogt et al., 2012). Most recently Wittenmyer

et al. (2013) found nine additional RV systems whose data are better fit by multiple planets on low-eccentricity orbits, rather than isolated planets on eccentric orbits. As more data are collected and reanalyzed, it appears the trend of systems with more planets on circular orbits will continue to grow stronger.

The direct imaging study of 14 Her, discussed in Chapter 3 (Rodigas et al., 2011), built on this work by combining RV data with direct imaging in a particularly favorable case. Since the residuals of the one-planet fit to the RV data showed a long-term trend indicative of a massive outer companion, we were able to rule out significant portions of the putative planet's phase space in just a few hours of imaging at the MMT. More importantly, we demonstrated how to combine RV data, imaging data, and even dynamical estimates, to constrain an exoplanet's mass, semimajor axis, and eccentricity. This type of analysis will be crucial in the future as ELTs are used to directly image older systems that have known RV planets.

My work discussed in Chapters 4-6 dealt largely with understanding and characterizing debris disks. What are the typical dust grain sizes in the HD 15115 debris disk? What is the composition of the dust in the HD 32297 debris disk? How does dust behave in the presence of massive planets, and can the disk itself be used as a signpost of a nearby planet? These are the questions I have attempted to answer.

In Chapter 4, I presented my recent imaging 2-4  $\mu\text{m}$  results on the HD 15115 debris disk (Rodigas et al., 2012). Formerly only known to contain small dust grains  $< 1 \mu\text{m}$  in size, I showed that a stable population of dust grains 1-10  $\mu\text{m}$  in size exists close to the star. Detecting scattered light from faint debris disks at such long wavelengths was previously thought to be too difficult, but with the exceptional imaging ability of LBTI and the LBT AO system, along with new



advances in image processing (Lafrenière et al., 2007), I showed that obtaining accurate photometry at these wavelengths was possible.

Building on this work, in Chapter 5, I presented my recent  $L'$  imaging results on the HD 32297 debris disk. This disk is much brighter than HD 15115's at  $L'$  and was therefore detected at much higher S/N. This allowed us to obtain more accurate photometry, leading to better constraints on the composition of the dust. We found that the disk's spectrum does not match the cometary dust model proposed by Donaldson et al. (2013). Model disks consisting of small silicates or small tholins better reproduce the red color of the disk between 1-4  $\mu\text{m}$ , but fail to accurately match the 1-2  $\mu\text{m}$  HST data. Additional modeling and data is necessary to fully characterize the dust's composition in the disk.

Finally, in Chapter 6, I presented my recent theory work on the dynamics of dust grains in the presence of massive planets. I built on the previous work of Chiang et al. (2009), who used dynamical modeling to constrain the mass of Formalhaut b. I extrapolated their methods to more general cases and a wider range of planet and disk parameters in order to empirically estimate the relationships between a debris disk's observed features and an unseen planet's mass and orbit. I found that a debris disk's width is proportional to the mass of its perturbing planet. We could obtain only upper limits on the planet masses, owing to our simplified dynamical modelling. This is still a very powerful result, one that should help observers select the most favorable debris disks for direct imaging follow-up.

In this thesis, I have laid the groundwork for future studies of exoplanets and debris disks. A natural next step is to build on my imaging work of debris disks. In particular, technology is beginning to allow for precise detection of faint debris disks at wavelengths previously too difficult to image at from the ground. These

longer wavelengths allow for accurate compositional modeling of the dust. In the following section, I discuss my plans for imaging and modeling several additional debris disks from the ground.

## 7.2 Future Work: Searching for Water Ice and Organics in Resolved Debris Disks with MagAO/Clio

This upcoming fall, I will be starting three-year postdoctoral fellowship at the Carnegie Institute of Washington, Department of Terrestrial Magnetism (DTM), in Washington D.C. There I will work closely with Alycia Weinberger on NIR imaging of resolved debris disks with MagAO/Clio. Below I discuss our specific plans.

Many outer solar system bodies contain copious amounts of water ice (Drake (2005), and references therein). Additionally studies have shown that organics can form in space (Sandford, 2009) and could possibly have been delivered to Earth in the early solar system via gravitational scattering by Jupiter (Gr   J  rgensen et al., 2009). Do water ice and organics exist in the circumstellar environments of stars outside the solar system? If so, what is their spatial distribution? As a first step towards answering these questions, I will search for water ice and organic materials in extrasolar debris disks by obtaining resolved high-contrast images. I will use the newly commissioned Magellan adaptive optics (AO) system (MagAO; Close et al. (2010, 2013); Follette et al. (2013)) and Clio, a 1-5  $\mu\text{m}$  high-contrast imaging camera previously operating at the MMT. The MagAO system is a clone of the LBT's AO system, with an identical ASM (which in practice has fewer functioning actuators) and a PWFS. The ASM and PWFS combine to correct up to 300 modes of wavefront error, producing low thermal background, high Strehl ratio images, especially in the NIR. This facilitates de-

tecting debris disks from the ground with Clio. The discovery of water ice and/or organic materials in a debris disk would be a landmark achievement, one that would hint that our solar system may not be so unique.

Water ice and organic materials have unique spectral features in the 1-10  $\mu\text{m}$  range. In particular, water ice has a strong absorption feature near 3  $\mu\text{m}$ . This feature has so far been detected spectroscopically in young gas-rich disks like those around HK Tau B and HV Tau C (Terada et al., 2007). Recently Honda et al. (2009) detected the feature in the disk of the Herbig Ae star HD 142527 using ground-based images at 2.2  $\mu\text{m}$  (Ks band), 3.09  $\mu\text{m}$  (narrow H<sub>2</sub>O band), and 3.8  $\mu\text{m}$  (L' band), showing how photometry can also pick out water ice absorption (see Fig. 7.1 left panel). This feature can also be attributed to organic materials like tholins. The near-infrared spectrum of Saturn's moon Phoebe (Fig. 7.2 middle panel) has this characteristic feature, attributed by Buratti et al. (2008) to a combination of tholins and water ice. The debris disk around HR 4796A is also believed to contain tholins based on its red spectrum between 1-2  $\mu\text{m}$  (Fig. 7.1 right panel, from John Debes, private communication). Photometry between 1-4  $\mu\text{m}$  is required to distinguish between water ice, tholins, and other dust compositions in the disk.

I will observe at 1-4  $\mu\text{m}$  (J, H, Ks, H<sub>2</sub>O, and L') bright, spatially-resolved southern hemisphere debris disks (see Table 7.1). Each target disk is required to have a surface brightness value brighter than 14 mags/sq. asec; this ensures that  $3\sigma$  disk detections will not require more than 2 hours at a given wavelength. To date there are seven such stars, one of which (HR 4796A), we have already obtained resolved images of at Ks, H<sub>2</sub>O, 3.3  $\mu\text{m}$ , and L'; Rodigas et al., in prep.).

With resolved photometric images at J, H, Ks, H<sub>2</sub>O, and L', I will compare the brightness of each disk with model spectra for dust of different compositions. Taking advantage of the resources at Carnegie DTM, I will work with the institu-

Table 7.1 Debris Disk Target List

Name	Spectral type	Distance (pc)	SB (mags/sq. asec)	Integration/mins (J/H/Ks/H <sub>2</sub> O/L')
HD 32297	A0	113	13.75	25/25/25/75/75
HD 61005	G8	35.3	14	30/30/30/90/90
AU Mic	M1	9.9	9	<10/<10/<10/<60/<60
HD 15115	F2	45.2	14	30/30/-/90/-
Beta Pic	A6	19.3	10	<10/<10/<10/<60/<60
HD 181327	F6	51.8	13.85	30/30/30/80/80 (x2)
HR 4796A	A0	67	13	12/12/12/40/40

tion's world-leading researchers in fields such as geochemistry, geophysics, geology, and planetary science to accurately model the disk colors observed. Their ongoing NASA Astrobiology Institute (NAI) programs studying icy bodies in the outer solar system (e.g., Sheppard (2012)) and organics in meteorites (e.g., Cody et al. (2012)) will be particularly valuable for a better understanding of the potentially complex organic materials in the debris disks. With resolved images, I will also probe the spatial distributions of the dust, showing how composition changes as a function of separation from the star. Finally, because ADI/PCA naturally pick out point sources in addition to extended objects like disks, I will set strong limits on planetary-mass companions around each star. In the event a companion is detected, I will have multi-wavelength photometry to constrain its atmosphere (e.g., Skemer et al. (2012)).

Fig. 7.2 is a good representation of the aims of this program. Using high-contrast imaging, I will identify the systems that have the prebiotic soup ingredients that are key for life. This is crucial for future exploration and characterization of exoplanetary systems. JWST, in particular, will have both the resolving power and the sensitivity to study systems in greater detail than ever before. The debris

disks from this program that are found to have significant amounts of water ice and organics could be key first targets for JWST. As our understanding of the universe continues to grow, the answer to the key question—“Are there other systems out there like ours?”—is finally within our reach.

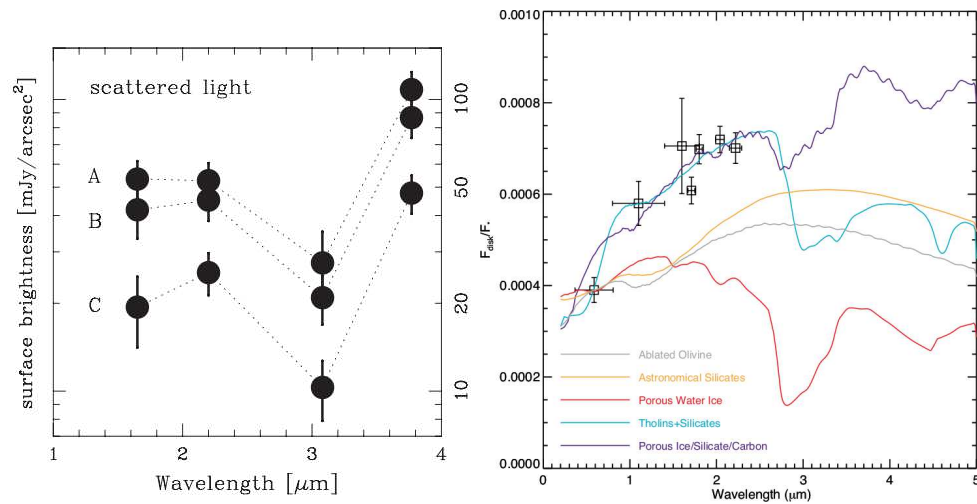


Figure 7.1 *Left*: from Honda et al. (2009), 2–4  $\mu\text{m}$  photometry of the circumstellar disk of the Herbig Ae star HD 142527. *Right*: NIR spectrum of the HR 4796A debris disk (squares, from HST), along with model spectra of various dust species (from John Debes, private communication).

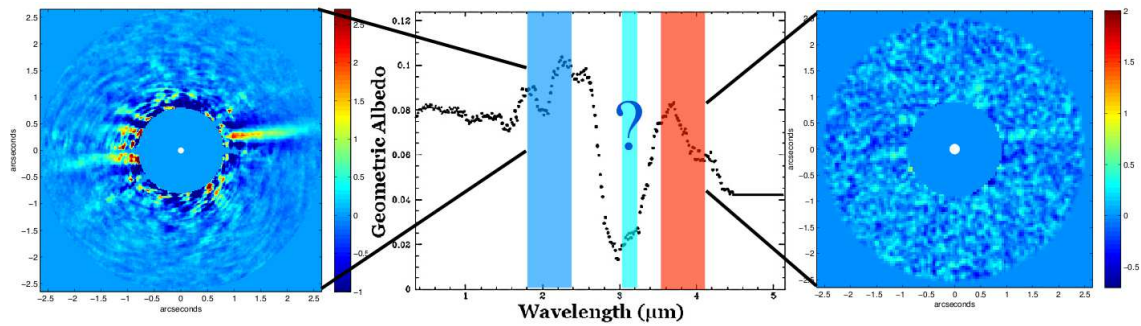


Figure 7.2 Spectrum of Saturn's moon Phoebe from Buratti et al. (2008), with Ks and L' images of the HD 15115 debris disk on either side (Rodigas et al., 2012). With an additional resolved image of the disk in the H<sub>2</sub>O band, we could constrain the amount of water ice/organics in the dust. This is the general idea for each target debris disk.

## APPENDIX A

## ACCOUNTING FOR DISK SELF-SUBTRACTION BY LOCI IN THE HD 15115 DATA

To account for disk self-subtraction by the LOCI algorithm, at each wavelength we inserted an artificial model disk into the raw data, at a PA nearly perpendicular to the known disk, ran the data through the pipeline, and recovered the model disks. The artificial disks were set to SB levels comparable to the real disks at each wavelength, and the widths of the artificial and real disks were comparable. Fig. A.1a and Fig. A.1b show the expected and recovered model disks at  $Ks$  band, respectively; Fig. A.1c and Fig. A.1d show the same at  $L'$ .

After recovering the model disks, we compared the observed PA, FWHM, and SB values as a function of distance from the star with the expected PA, FWHM, and SB values. The calculations were performed with identical methods to the real disk data analysis. At both wavelengths, the expected and observed PA values are consistent with each other, therefore no correction was needed (see Fig. A.2a and Fig. A.2b). At  $Ks$  band, an addition to the observed FWHM of  $\sim 0''.03$  was needed to correct the apparent constant offset (see Fig. A.2c). At  $L'$ , a correction was also needed, with a value of  $\sim 0''.11$  (see Fig. A.2d). Both FWHM correction offsets have been included in the FWHM analysis of the real disk images.

To correct for the reduction in disk SB at both wavelengths relative to the expected values, we mapped out the self-subtraction as a function of distance and multiplied this into each recovered disk. The corrected SB values, along with the expected and observed, are shown in Fig. A.2e ( $Ks$  band) and Fig. A.2f ( $L'$ ). The SB corrections have been included in the SB analysis of the real disk images.

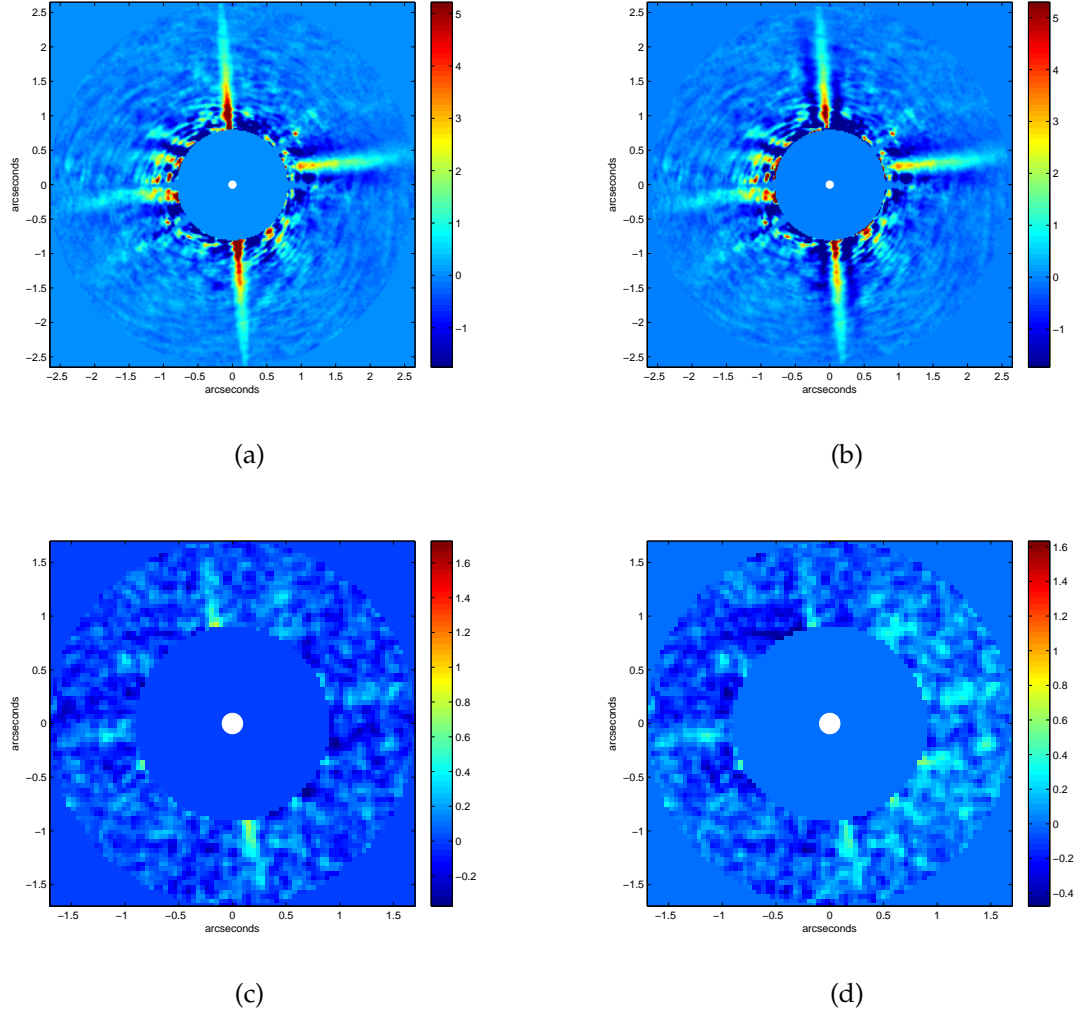


Figure A.1 Expected and observed artificial disks at  $Ks$  band and  $L'$ . Model disks are always vertical. *Top left*:  $Ks$  band image of the artificial disk, showing what the disk should look like if unaltered by the LOCI algorithm reduction. *Top right*:  $Ks$  band image of the recovered model disk. *Bottom left*: the same as (a) except at  $L'$ . *Bottom right*: the same as (b), except at  $L'$ . In all cases, the model disks are recovered, though some self-subtraction is evident.



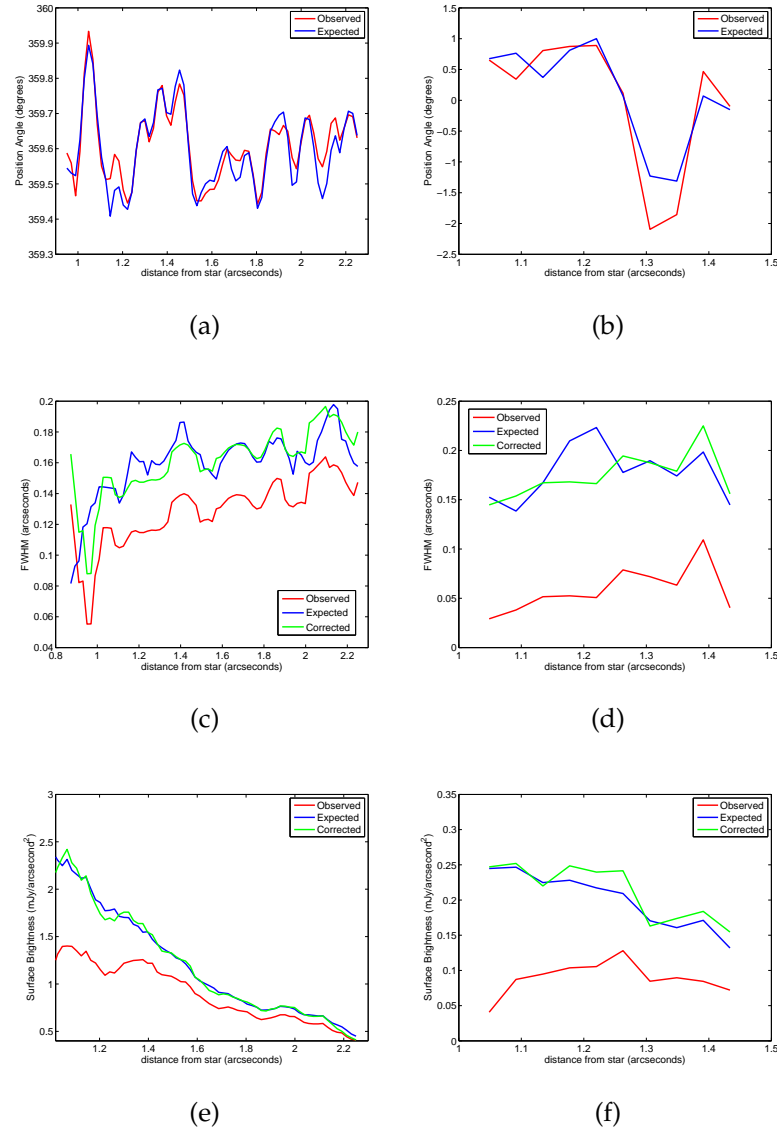


Figure A.2 *Top left:* Expected (blue) and observed (red) model disk PA vs. distance from the star at  $Ks$  band. No correction is needed. *Top right:* the same, except at  $L'$ . No correction is needed. *Middel left:* Expected (blue), observed (red), and corrected (green) model disk FWHM vs. distance from the star at  $Ks$  band. An offset correction of  $\sim 0''.03$  is needed. *Middle right:* the same, except at  $L'$ . An offset correction of  $\sim 0''.11$  is needed. *Bottom left:* Expected (blue), observed (red), and corrected (green) model disk SB vs. distance from the star. *Bottom right:* the same, except at  $L'$ .

## REFERENCES

- Adams, F. C., & Laughlin, G. 2003, *Icarus*, 163, 290
- Augereau, J.-C., & Beust, H. 2006, *A&A*, 455, 987
- Baraffe, I., Chabrier, G., Barman, T. S., Allard, F., & Hauschildt, P. H. 2003, *A&A*, 402, 701
- Boccaletti, A., et al. 2012, *A&A*, 544, A85
- Boccaletti, A., Lagrange, A.-M., Bonnefoy, M., Galicher, R., & Chauvin, G. 2013, *A&A*, 551, L14
- Boley, A. C., Payne, M. J., Corder, S., Dent, W. R. F., Ford, E. B., & Shabram, M. 2012, *ApJL*, 750, L21
- Bonnefoy, M., et al. 2013, *ArXiv e-prints*
- Boss, A. P. 1997, *Science*, 276, 1836
- Bressan, A., Marigo, P., Girardi, L., Salasnich, B., Dal Cero, C., Rubele, S., & Nanni, A. 2012, *MNRAS*, 427, 127
- Buenzli, E., et al. 2010, *A&A*, 524, L1
- Buratti, B. J., et al. 2008, *Icarus*, 193, 309
- Burrows, A., Sudarsky, D., & Lunine, J. I. 2003, *ApJ*, 596, 587
- Butler, R. P., et al. 2006, *ApJ*, 646, 505
- Carson, J. C., Hiner, K. D., Villar, G. G., Blaschak, M. G., Rudolph, A. L., & Stapelfeldt, K. R. 2009, *AJ*, 137, 218

- Chauvin, G., Lagrange, A.-M., Dumas, C., Zuckerman, B., Mouillet, D., Song, I., Beuzit, J.-L., & Lowrance, P. 2004, *A&A*, 425, L29
- Chiang, E., Kite, E., Kalas, P., Graham, J. R., & Clampin, M. 2009, *ApJ*, 693, 734
- Close, L. M., Gasho, V., Kopon, D., Males, J., Follette, K. B., Brutlag, K., Uomoto, A., & Hare, T. 2010, in *Society of Photo-Optical Instrumentation Engineers (SPIE) Conference Series*, Vol. 7736, Society of Photo-Optical Instrumentation Engineers (SPIE) Conference Series
- Close, L. M., et al. 2013, *ArXiv e-prints*
- Cody, G. D., Wang, Y., Kebukawa, Y., Fogel, M. L., & Alexander, C. M. O. 2012, *LPI Contributions*, 1667, 6176
- Crepp, J. R., et al. 2012a, *ApJ*, 751, 97
- . 2012b, *ApJ*, 761, 39
- Currie, T., Bailey, V., Fabrycky, D., Murray-Clay, R., Rodigas, T., & Hinz, P. 2010, *ApJL*, 721, L177
- Currie, T., et al. 2011, *ApJ*, 729, 128
- . 2012a, *ApJL*, 760, L32
- . 2012b, *ApJL*, 760, L32
- . 2012c, *ApJ*, 757, 28
- Debes, J. H., Weinberger, A. J., & Kuchner, M. J. 2009, *ApJ*, 702, 318
- Debes, J. H., Weinberger, A. J., & Schneider, G. 2008a, *ApJL*, 673, L191
- Debes, J. H., Weinberger, A. J., & Song, I. 2008b, *ApJL*, 684, L41

- Dohnanyi, J. S. 1969, *J. Geophys. Res.*, 74, 2531
- Donaldson, J. K., Lebreton, J., Roberge, A., Augereau, J.-C., & Krivov, A. V. 2013, ArXiv e-prints
- Drake, M. J. 2005, *Meteoritics and Planetary Science*, 40, 519
- Duchêne, G., McCabe, C., Ghez, A. M., & Macintosh, B. A. 2004, *ApJ*, 606, 969
- Ertel, S., Wolf, S., Metchev, S., Schneider, G., Carpenter, J. M., Meyer, M. R., Hillenbrand, L. A., & Silverstone, M. D. 2011, *A&A*, 533, A132
- Esposito, S., et al. 2011, in *Society of Photo-Optical Instrumentation Engineers (SPIE) Conference Series*, Vol. 8149, Society of Photo-Optical Instrumentation Engineers (SPIE) Conference Series
- Esposito, S., et al. 2010, *Appl. Opt.*, 49, G174
- Fischer, D. A., Marcy, G. W., Butler, R. P., Vogt, S. S., Frink, S., & Apps, K. 2001, *ApJ*, 551, 1107
- Fitzgerald, M. P., Kalas, P. G., Duchêne, G., Pinte, C., & Graham, J. R. 2007, *ApJ*, 670, 536
- Follette, K. B., et al. 2013, ArXiv e-prints
- Freed, M., Hinz, P. M., Meyer, M. R., Milton, N. M., & Lloyd-Hart, M. 2004, in *Presented at the Society of Photo-Optical Instrumentation Engineers (SPIE) Conference*, Vol. 5492, Society of Photo-Optical Instrumentation Engineers (SPIE) Conference Series, ed. A. F. M. Moorwood & M. Iye, 1561–1571
- Galicher, R., Marois, C., Zuckerman, B., & Macintosh, B. 2012, ArXiv e-prints

- Gáspár, A., Psaltis, D., Rieke, G. H., & Özel, F. 2012, *ApJ*, 754, 74
- Gould, A., et al. 2010, *ApJ*, 720, 1073
- Goździewski, K., Konacki, M., & Maciejewski, A. J. 2006, *ApJ*, 645, 688
- Goździewski, K., Migaszewski, C., & Konacki, M. 2008, *MNRAS*, 385, 957
- Gråe Jørgensen, U., Appel, P. W. U., Hatsukawa, Y., Frei, R., Oshima, M., Toh, Y., & Kimura, A. 2009, *Icarus*, 204, 368
- Guyon, O. 2005, *ApJ*, 629, 592
- Hahn, J. M. 2010, *ApJ*, 719, 1699
- Han, I., Black, D. C., & Gatewood, G. 2001, *ApJL*, 548, L57
- Heckmann, O. 1975, AGK 3. Star catalogue of positions and proper motions north of -2.5 deg. declination
- Heinze, A. N., Hinz, P. M., Kenworthy, M., Miller, D., & Sivanandam, S. 2008, *ApJ*, 688, 583
- Helled, R., & Schubert, G. 2008, *Icarus*, 198, 156
- Hines, D. C., et al. 2007, *ApJL*, 671, L165
- Hinz, P. M., et al. 2008, in Society of Photo-Optical Instrumentation Engineers (SPIE) Conference Series, Vol. 7013, Society of Photo-Optical Instrumentation Engineers (SPIE) Conference Series
- Hinz, P. M., Heinze, A. N., Sivanandam, S., Miller, D. L., Kenworthy, M. A., Brusa, G., Freed, M., & Angel, J. R. P. 2006, *ApJ*, 653, 1486

- Hinz, P. M., Rodigas, T. J., Kenworthy, M. A., Sivanandam, S., Heinze, A. N., Mamajek, E. E., & Meyer, M. R. 2010, *ApJ*, 716, 417
- Holman, M. J., & Wisdom, J. 1993, *AJ*, 105, 1987
- Honda, M., et al. 2009, *ApJL*, 690, L110
- Hong, S. S. 1985, *A&A*, 146, 67
- Ida, S., & Lin, D. N. C. 2004, *ApJ*, 616, 567
- Inoue, A. K., Honda, M., Nakamoto, T., & Oka, A. 2008, *PASJ*, 60, 557
- Janson, M., et al. 2009, *MNRAS*, 399, 377
- Janson, M., Bergfors, C., Goto, M., Brandner, W., & Lafrenière, D. 2010, *ApJL*, 710, L35
- Janson, M., Carson, J. C., Lafrenière, D., Spiegel, D. S., Bent, J. R., & Wong, P. 2012, *ApJ*, 747, 116
- Jurić, M., & Tremaine, S. 2008, *ApJ*, 686, 603
- Kalas, P., Fitzgerald, M. P., & Graham, J. R. 2007, *ApJL*, 661, L85
- Kalas, P., et al. 2008, *Science*, 322, 1345
- Kalas, P., Graham, J. R., & Clampin, M. 2005, *Nature*, 435, 1067
- Kalas, P., Graham, J. R., Fitzgerald, M. P., & Clampin, M. 2013, *ArXiv e-prints*
- Kennedy, G. M., & Kenyon, S. J. 2008, *ApJ*, 673, 502
- Kenworthy, M. A., Mamajek, E. E., Hinz, P. M., Meyer, M. R., Heinze, A. N., Miller, D. L., Sivanandam, S., & Freed, M. 2009, *ApJ*, 697, 1928

- Khare, B. N., Sagan, C., Arakawa, E. T., Suits, F., Callcott, T. A., & Williams, M. W. 1984, *Icarus*, 60, 127
- Krist, J. E., Stapelfeldt, K. R., Bryden, G., & Plavchan, P. 2012, *AJ*, 144, 45
- Krist, J. E., et al. 2010, *AJ*, 140, 1051
- Kuchner, M. J., & Holman, M. J. 2003, *ApJ*, 588, 1110
- Lafrenière, D., Marois, C., Doyon, R., Nadeau, D., & Artigau, É. 2007, *ApJ*, 660, 770
- Lagrange, A., et al. 2010, *Science*, 329, 57
- . 2009, *A&A*, 493, L21
- Lagrange, A.-M., et al. 2012, *A&A*, 546, A38
- Laor, A., & Draine, B. T. 1993, *ApJ*, 402, 441
- Lebreton, J., et al. 2012, *A&A*, 539, A17
- Leconte, J., et al. 2010, *ApJ*, 716, 1551
- Leggett, S. K., et al. 2003, *MNRAS*, 345, 144
- Levison, H. F., Lissauer, J. J., & Duncan, M. J. 1998, *AJ*, 116, 1998
- Liu, M. C. 2004, *Science*, 305, 1442
- Lloyd-Hart, M. 2000, *PASP*, 112, 264
- Luhman, K. L., & Jayawardhana, R. 2002, *ApJ*, 566, 1132
- Lyra, W., & Kuchner, M. 2013, *Nature*, 499, 184

- Malhotra, R. 1998, in *Astronomical Society of the Pacific Conference Series*, Vol. 149, *Solar System Formation and Evolution*, ed. D. Lazzaro, R. Vieira Martins, S. Ferraz-Mello, & J. Fernandez , 37
- Mamajek, E. E., & Hillenbrand, L. A. 2008, *ApJ*, 687, 1264
- Maness, H. L., Fitzgerald, M. P., Paladini, R., Kalas, P., Duchene, G., & Graham, J. R. 2008, *ApJL*, 686, L25
- Maness, H. L., et al. 2009, *ApJ*, 707, 1098
- Marley, M. S., Fortney, J. J., Hubickyj, O., Bodenheimer, P., & Lissauer, J. J. 2007, *ApJ*, 655, 541
- Marois, C., Lafrenière, D., Doyon, R., Macintosh, B., & Nadeau, D. 2006, *ApJ*, 641, 556
- Marois, C., Macintosh, B., Barman, T., Zuckerman, B., Song, I., Patience, J., Lafrenière, D., & Doyon, R. 2008, *Science*, 322, 1348
- Marois, C., Zuckerman, B., Konopacky, Q. M., Macintosh, B., & Barman, T. 2010, *Nature*, 468, 1080
- Mawet, D., Serabyn, E., Stapelfeldt, K., & Crepp, J. 2009, *ApJL*, 702, L47
- McCarthy, Jr., D. W., Ge, J., Hinz, J. L., Finn, R. A., & de Jong, R. S. 2001, *PASP*, 113, 353
- Minton, D. A., & Malhotra, R. 2010, *Icarus*, 207, 744
- Moór, A., Ábrahám, P., Derekas, A., Kiss, C., Kiss, L. L., Apai, D., Grady, C., & Henning, T. 2006, *ApJ*, 644, 525



- Moór, A., et al. 2011a, *ApJL*, 740, L7
- . 2011b, *ApJS*, 193, 4
- Moro-Martín, A., & Malhotra, R. 2005, *ApJ*, 633, 1150
- Mustill, A. J., & Wyatt, M. C. 2012, *MNRAS*, 419, 3074
- Naef, D., Mayor, M., Beuzit, J. L., Perrier, C., Queloz, D., Sivan, J. P., & Udry, S. 2004, *A&A*, 414, 351
- Nielsen, E. L., & Close, L. M. 2010, *ApJ*, 717, 878
- Patience, J., et al. 2002, *ApJ*, 581, 654
- Quillen, A. C. 2006, *MNRAS*, 372, L14
- Ragazzoni, R. 1996, *Journal of Modern Optics*, 43, 289
- Rasio, F. A., & Ford, E. B. 1996, *Science*, 274, 954
- Raymond, S. N., et al. 2011, *A&A*, 530, A62
- . 2012, *A&A*, 541, A11
- Reffert, S., & Quirrenbach, A. 2011, *A&A*, 527, A140
- Rhee, J. H., Song, I., Zuckerman, B., & McElwain, M. 2007, *ApJ*, 660, 1556
- Rocha-Pinto, H. J., Maciel, W. J., Scalo, J., & Flynn, C. 2000, *A&A*, 358, 850
- Rodigas, T. J., & Hinz, P. M. 2009, *ApJ*, 702, 716
- Rodigas, T. J., et al. 2012, *ApJ*, 752, 57
- Rodigas, T. J., Males, J. R., Hinz, P. M., Mamajek, E. E., & Knox, R. P. 2011, *ApJ*, 732, 10

- Sandford, S. A. 2009, in *Astronomical Society of the Pacific Conference Series*, Vol. 420, *Bioastronomy 2007: Molecules, Microbes and Extraterrestrial Life*, ed. K. J. Meech, J. V. Keane, M. J. Mumma, J. L. Siefert, & D. J. Werthimer, 113
- Schneider, G., et al. 2006, *ApJ*, 650, 414
- Schneider, G., Weinberger, A. J., Becklin, E. E., Debes, J. H., & Smith, B. A. 2009, *AJ*, 137, 53
- Shen, Y., & Turner, E. L. 2008, *ApJ*, 685, 553
- Sheppard, S. S. 2012, ArXiv e-prints
- Silverstone, M. D. 2000, PhD thesis, UNIVERSITY OF CALIFORNIA, LOS ANGELES
- Sivanandam, S., Hinz, P. M., Heinze, A. N., Freed, M., & Breuninger, A. H. 2006, in *Society of Photo-Optical Instrumentation Engineers (SPIE) Conference Series*, Vol. 6269, *Society of Photo-Optical Instrumentation Engineers (SPIE) Conference Series*
- Skemer, A. J., et al. 2012, *ApJ*, 753, 14
- Skrutskie, M. F., et al. 2010, in *Society of Photo-Optical Instrumentation Engineers (SPIE) Conference Series*, Vol. 7735, *Society of Photo-Optical Instrumentation Engineers (SPIE) Conference Series*
- Soummer, R., Pueyo, L., & Larkin, J. 2012, *ApJL*, 755, L28
- Spiegel, D. S., & Burrows, A. 2012, *ApJ*, 745, 174
- Szebehely, V., & McKenzie, R. 1981, *Celestial Mechanics*, 23, 3

- Takeda, G., Ford, E. B., Sills, A., Rasio, F. A., Fischer, D. A., & Valenti, J. A. 2007, *ApJS*, 168, 297
- Takeda, Y. 2007, *PASJ*, 59, 335
- Terada, H., Tokunaga, A. T., Kobayashi, N., Takato, N., Hayano, Y., & Takami, H. 2007, *ApJ*, 667, 303
- Thalmann, C., et al. 2009, *ApJL*, 707, L123
- . 2013, *ApJL*, 763, L29
- . 2011, *ApJL*, 743, L6
- Thebault, P., Kral, Q., & Ertel, S. 2012, *A&A*, 547, A92
- Torres, C. A. O., Quast, G. R., da Silva, L., de La Reza, R., Melo, C. H. F., & Sterzik, M. 2006, *A&A*, 460, 695
- Valenti, J. A., & Fischer, D. A. 2005, *ApJS*, 159, 141
- van Leeuwen, F., ed. 2007a, *Astrophysics and Space Science Library*, Vol. 350, *Hipparcos, the New Reduction of the Raw Data*
- van Leeuwen, F. 2007b, *A&A*, 474, 653
- Vogt, S. S., Butler, R. P., & Haghighipour, N. 2012, *Astronomische Nachrichten*, 333, 561
- Williams, J. P., & Andrews, S. M. 2006, *ApJ*, 653, 1480
- Wisdom, J. 1980, *AJ*, 85, 1122
- Wisdom, J., & Holman, M. 1991, *AJ*, 102, 1528

- Wittenmyer, R. A., Endl, M., & Cochran, W. D. 2007, *ApJ*, 654, 625
- Wittenmyer, R. A., et al. 2012, *ApJ*, 753, 169
- . 2013, ArXiv e-prints
- Wolf, S., & Voshchinnikov, N. V. 2004, *Computer Physics Communications*, 162, 113
- Wright, J. T., Marcy, G. W., Butler, R. P., & Vogt, S. S. 2004, *ApJS*, 152, 261
- Wright, J. T., Upadhyay, S., Marcy, G. W., Fischer, D. A., Ford, E. B., & Johnson, J. A. 2009, *ApJ*, 693, 1084
- Wyatt, M. C. 2005, *A&A*, 433, 1007
- . 2008, *ARA&A*, 46, 339
- Wyatt, M. C., Dermott, S. F., Telesco, C. M., Fisher, R. S., Grogan, K., Holmes, E. K., & Piña, R. K. 1999, *ApJ*, 527, 918
- Yelda, S., Lu, J. R., Ghez, A. M., Clarkson, W., Anderson, J., Do, T., & Matthews, K. 2010, *ApJ*, 725, 331
- Zuckerman, B., & Song, I. 2004, *ApJ*, 603, 738